Award Number:
W81XWH-09-1-0410

TITLE:
Harnessing the Úower of Šight to Ùee and Vreat Óreast Ôancer

PRINCIPAL INVESTIGATOR:
Nirmala Ramanujam Ph.D.

CONTRACTING ORGANIZATION: Duke University
Durham, NC 27708

REPORT DATE: December 2015

TYPE OF REPORT: Final

PREPARED FOR: U.S. Army Medical Research and Materiel Command
Fort Detrick, Maryland 21702-5012

DISTRIBUTION STATEMENT: Approved for Public Release;
Distribution Unlimited

REPORT DOCUMENTATION PAGE

Form Approved
OMB No. 0704-0188

Public reporting burden for this collection of information is estimated to average 1 hour per response, including the time for reviewing instructions, searching existing data sources, gathering and maintaining the data needed, and completing and reviewing this collection of information. Send comments regarding this burden estimate or any other aspect of this collection of information, including suggestions for reducing this burden to Department of Defense, Washington Headquarters Services, Directorate for Information Operations and Reports (0704-0188), 1215 Jefferson Davis Highway, Suite 1204, Arlington, VA 22202-4302. Respondents should be aware that notwithstanding any other provision of law, no person shall be subject to any penalty for failing to comply with a collection of information if it does not display a currently valid OMB control number. **PLEASE DO NOT RETURN YOUR FORM TO THE ABOVE ADDRESS.**

1. REPORT DATE *(DD-MM-YYYY)*	2. REPORT TYPE	3. DATES COVERED *(From - To)*
December 2015	Final	18 Sep 2009 - 17 Sep 2015

4. TITLE AND SUBTITLE

Harnessing the Power of Light to See and Treat Breast Cancer

5a. CONTRACT NUMBER

5b. GRANT NUMBER
W81XWH-09-1-0410

5c. PROGRAM ELEMENT NUMBER

6. AUTHOR(S)

Nirmala Ramanujam Ph.D.

go ckx"pko o kB f wng@f w

5d. PROJECT NUMBER

5e. TASK NUMBER

5f. WORK UNIT NUMBER

7. PERFORMING ORGANIZATION NAME(S) AND ADDRESS(ES)

Duke University
ÁÁÁÁÁÁÁÁÁÁÁ
ÁÁÁÁÁÁÁÁÁÁÁÁÁÁÁÁÁ
Durham, NC 27708

8. PERFORMING ORGANIZATION REPORT NUMBER

9. SPONSORING / MONITORING AGENCY NAME(S) AND ADDRESS(ES)
U.S. Army Medical Research And Materiel Command

Fort Detrick, Maryland 21702-5012

10. SPONSOR/MONITOR'S ACRONYM(S)

11. SPONSOR/MONITOR'S REPORT NUMBER(S)

12. DISTRIBUTION / AVAILABILITY STATEMENT

Approved for public release; distribution unlimited.

13. SUPPLEMENTARY NOTES

14. ABSTRACT

Our objective is to exploit the wealth of physiological, metabolic, morphological and molecular sources of optical contrast to develop novel strategies that focus on two breast cancer applications: tumor margin assessment and prediction of response to neo-adjuvant therapy. The proposed aims of this grant are expected to result in three major contributions. The first has the most immediate impact. An optically based strategy that can quickly and non-destructively detect positive tumor margins will decrease the need for re-excision surgery and thereby decrease the local recurrence rate and rate of distant metastases in women electing BCS. Gaining insight into the physiological, metabolic, morphological and molecular sources of heterogeneity within and among tumors and how they are modulated by therapy, drug resistance and metastatic potential will directly benefit prognostication, prediction of outcome and planning of cancer therapies. With these tools, clinicians and clinical researchers can get a better understanding of this disease and how it might react to a drug. Basic science researchers could use it as an informed approach to study tumor biology and assay the effect of novel therapeutic agents *in vivo*.

15. SUBJECT TERMS
optical spectroscopy, imaging, fiber-optic, molecular, screening, breast cancer

16. SECURITY CLASSIFICATION OF:			17. LIMITATION OF ABSTRACT	18. NUMBER OF PAGES	19a. NAME OF RESPONSIBLE PERSON USAMRMC
a. REPORT U	b. ABSTRACT U	c. THIS PAGE U	UU	73	19b. TELEPHONE NUMBER *(include area code)*

Standard Form 298 (Rev. 8-98)
Prescribed by ANSI Std. Z39.18

Table of Contents

1. INTRODUCTION

Our objective is to exploit the wealth of physiological, metabolic, morphological and molecular sources of optical contrast to develop novel strategies that focus on two breast cancer applications: tumor margin assessment and prediction of response to neo-adjuvant therapy. The proposed aims of this grant are expected to result in three major contributions. The first has the most immediate impact. An optically-based strategy that can quickly and non-destructively detect positive tumor margins will decrease the need for re-excision surgery and thereby decrease the local recurrence rate and rate of distant metastases in women electing BCS. Gaining insight into the physiological, metabolic, morphological and molecular sources of heterogeneity within and among tumors and how they are modulated by therapy, drug resistance and metastatic potential will directly benefit prognostication, prediction of outcome and planning of cancer therapies. With these tools, clinicians and clinical researchers can get a better understanding of this disease and how it might react to a drug. Basic science researchers could use it as an informed approach to study tumor biology and assay the effect of novel therapeutic agents *in vivo*.

a. Original Statement of Work for 5 Years

Aim 1: Optical imaging of margin morphology on breast lumpectomy specimens: To evaluate the role of wide-field imaging (coverage) and high-resolution interrogation (localization) of breast margin morphology to guide surgical resection intra-operatively and pathologic assessment of the tumor margin post-operatively (Timeframe: year 1-5).

  1a. Development of one optical spectral imaging system that integrates sensing capabilities for aims 1 and 2 and a high-resolution probe that can image absorption, scattering and fluorescence contrast (timeframe, year 1).
  1b. Conduct clinical studies on lumpectomy margins on 200 patients (time frame, years 2-4)
  1c. Data analysis and interpretation (timeframe, years 3-5)
    Test the sensitivity and specificity of wide-field imaging to detect positive tumor margins
    Test sensitivity and specificity of high-resolution probe to detect IDC and DCIS.

Aim 2: Optical quantitative biology of different sub-types of breast cancer: To investigate biomarkers of oxygenation, carotenoids (β-carotene) and ECM proteins (collagen) in human breast cancer stratified by tumor sub-type and receptor status and their association with neo-adjuvant chemotherapy response.

  2a. Development of rotating needle compatible spectroscopy probe (timeframe, year 1).
  2b. Conduct clinical studies to measure optical biomarkers *in vivo* in 150 patients undergoing surgery (timeframe, years 2-4).
  2c. Conduct clinical studies to measure optical biomarkers from 75 patients before neo-adjuvant therapy
  2d. Data analysis and interpretation (years 3-5):
    Determine association of biomarkers with tumor subtype
    Determine association of biomarkers with receptor status

Determine association of biomarkers with genomic signatures

Determine association of biomarkers with pathologic sub-total and complete response

Aim 3: Optical quantitative biology to assess therapy response in different sub-types of breast cancer: To investigate biomarkers of oxygenation and ECM proteins (collagen and $\alpha_v\beta_3$ expression) in rodent breast cancer stratified by tumor sub-type, receptor status and metastatic potential in response to targeted and chemotherapies.

3a. To determine if multi-parametric intra-vital optical microscopy, measuring hemoglobin saturation, total hemoglobin, redox ratio, collagen, and integrin expression can monitor tumor response to tamoxifen in parental and tamoxifen-resistant MCF-7 tumors in the mouse dorsal skin fold window chamber (timeframe, years 1-2).

- A total of 40 athymic nude mice will be required for this study (10 mice/group).

3b. Monitor optical parameters in the dorsal skin fold window chamber in response to doxorubicin chemotherapy in MCF-7 parental and doxorubicin-resistant tumors (timeframe, years 2-3).

- A total of 40 athymic nude mice will be required for this study.

3c. Monitor optical parameters in the dorsal skin fold window chamber in response to doxorubicin chemotherapy in tumors that express high (MDA-435) and low (MCF-7) levels of $\alpha_v\beta_3$ integrin (timeframe, years 3-4).

- A total of 40 athymic nude mice will be required for this study.

3d. Data and statistical analysis (timeframe, year 5).

2. BODY

Aim 1: *Optical imaging of margin morphology on breast lumpectomy specimens:*

Aim 1 seeks to leverage diffuse optical spectroscopy as a tool for rapidly surveying breast tumor margins. Specifically, we use a wide-field high-resolution diffuse optical spectroscopy device to quantify the likelihood of residual disease at the tumor excision site. The analysis must be performed rapidly to afford the surgeon enough time to act on the information. Initial studies for aim 1 informed the sources of optical contrast and established timing considerations, resulting in development of a 49-channel (49ch) device with a large field of view. The 49ch device was developed to survey a typical lumpectomy surface in a single spectral snapshot. In year 4, the 49ch device was further augmented with the development of computer-numeric-controlled (CNC) imaging platform to further improve the resolution and reduce random error introduced by the user. A custom multi-spectral LED light source was developed to improve system SNR and reduce the overall acquisition time (year 5). The high-power LEDs used afford a tenfold reduction in total acquisition time. In the final year, the acquisition and control software was revised to provide hi-resolution real-time optical property maps to aid in the designation of specific sites for pathological review and device validation. In this final year, we report our patient data analysis utilizing the optimized device.

Introduction

We have previously demonstrated that wide-field optical imaging of tumor morphology detects positive margins (margins with IDC and DCIS) with accuracies that well exceed that of the breast surgeon. Here we further refine our understanding of the micro-architectural differences between different types of tumor margin sub-types, in particular, DCIS, towards improving sensitivity and specificity. Our approach is to image the boundaries of the excised tumor mass, which is consistent with the existing paradigm for post-operative pathologic margin assessment, using the 49-channel device to acquire wide-field images of the tumor margins. We have previously shown that both radiographic breast density, as well as neoadjuvant status, impact the spectroscopic data of the surgical margins and should be considered when assessing the margin status. In this work, we investigate the influence of additional system parameters afforded by the latest generation wide-field imaging technology, such as sampling resolution and optical changes related to the pressure at the tissue-probe interface. Furthermore, we present a follow- up study based on empirical cumulative distribution functions (eCDFs) to corroborate previous findings now in the context of improved resolution. Data acquired from the first 57 patients using the hi-resolution wide-field system are analyzed and discussed.

Results

Part A. Advancing optical imaging for breast margin assessment:

Introduction

Breast conserving surgery (BCS) is a recommended treatment for early-stage breast cancer and for breast cancers that have been reduced in size by neoadjuvant therapy. The goal of

BCS is to excise the tumor along with a margin of normal tissue, while preserving as much of the normal breast tissue as possible. Unfortunately, as many as 18-72% of patients undergoing BCS require repeat surgeries due to a close or positive surgical margin diagnosed post-operatively and thus, require a re-excision surgery to achieve cancer free margins [1-9]. The large variation in re-excisions is thought to be due to differences in surgeon's training and in the perceived risk of focally positive margins versus extensive involvement [10].

Surgery to remove the cancer and obtain clear margins is a collaborative effort between the surgeon and the pathologist (and in some institutions, the radiologist). In spite of this, there can be substantial variability in the prediction of positive margins in the intra-operative and post-operative settings. Surgeons do not have adequate intra-operative assessment tools to ensure that the cancer has been completely removed at the time of first surgery. Pathologists do not have adequate tools for sampling from areas on large tumor margins. The lack of these capabilities represents a significant unmet clinical need for margin assessment for both the surgeon and pathologist.

Optical imaging of tissue is an attractive solution to this problem because it is relatively fast and non-destructive. Optical techniques can also measure features related to the histological landscape without the need for labels. Before this technology can be used in an intra-operative setting or in a post-operative setting, systematic studies have to be performed to determine which surgical and post-surgical factors affect the precision and accuracy with which this technology maps optical contrast. This is true not only for our technology but other technologies, both optical and non-optical that are intended for this application.

In the following section, we review technological optimizations to the clinical instrumentation. In previous reports, we detailed the transition to the 49-channel wide-field imaging probe and custom raster-scanning imaging platform. We used this technology to examine the impact of the pressure at the probe-tissue interface in the context of false-positive/ false negative rates. The optimal scanning resolution was determined to maximize the likelihood of detecting small regions of focal disease with intra-operative time scales in mind. The optimal raster-scanning upsample factor was determined to be 8: a full scan of a single margin can be acquired in less than 15 minutes (12.8mins) at a resolution better than 1mm (.75mm). Considering breast tumor margin assessment, resolution greater than 1mm is warranted to increase the probability of detection of focal disease. Small regions of focal disease are particularly important to discover as standard of care stipulates that partial mastectomy specimens be sliced at 5mm increments for histological preparation. The optical property extraction accuracy of the wide-field 49-channel probe was shown consistent with previous generation devices (less than 10% for mus' and mua). The reproducibility of the scanning mechanism was evaluated clinically and shown to be within 1%.

One identified clinical limitation with the integrated spectral scanning system is the manner in which the sites marked for histopathological review are performed. After a scan has taken place, the user replaces the probe with a plastic component with the exact geometry of the probe used but with holes in place of the optical channels. The downside to this is twofold: 1) ink dots can only be placed where an optical channel exists, meaning that each dot must be offset by at least

the pixel pitch of the probe. In the case of breast tumor margins, there is typically a dense region of tumor/morphological activity or a very sparse, subtle region of localized disease. To accurately corroborate our technology across all tissue subtypes, there must be mechanism to remove this geometric constraint such that any suspicious region can be indicated for review by pathology. The second limitation stems from the contact made by the inking hardware; because the inking plate is pressed against the hardware, the ink tends to run along the hardware and tissue surface, resulting in smeared dots that make the exact location of the ink centroid ambiguous.

Detailed in this section is the final phase of the imaging platform development. We implement optimizations to facilitate sample co-registration, guided site-level inking (explained in detail below), improve sanitation, and enhance the device footprint.

Methods

The final platform embodiment is achieved with the addition of a board-level camera, an integrated low-power laser, and a copper specimen base plate. The imaging platform was redesigned to improve modularity and utilize low-cost ABS plastic instead of machined aluminum, reducing the overall cost and weight. Optically aligned dovetail attachments were developed to house a low-power laser, similar to a laser pointer that is programmatically powered and positioned. Software updates detailed in Part B allow the user to choose any pixel within the upsampled image to position the laser, at which point the site can be inked without any hardware interference or limitation on the next inked location. The position was tracked in software using the number of steps output to each motor relative to a stop switch-based home position, providing precise (±3μm) co-registration information for the optical parameter maps.

Informed by routine clinical use; sanitization was addressed as the polycarbonate plate (where the specimen rests) began to scuff and retain residual tissue. The polycarbonate plate also did not provide enough resistance to keep the specimen in place while the probe established contact. The specimen plate was replaced with 2mm thick copper plate machined in-house to provide a small, grooved cavity to prevent the specimen from moving.

Results

The spatial translation approach was modified such that the specimen is translated in the x,y directions while the probe is translated in the z direction, as opposed to translating the probe in each dimension (previous method). Fig. 1.1 illustrates the reduction in size resulting from this modification. Two separate dovetail attachment points were designed to accompany the probe hardware, the inking hardware, and the digital camera. These attachment points share an optical axis and allow the user to interchange the components as needed for the clinical circumstance. The importance of this design is obvious in the case of specimens containing radio-active seeds; the specimen cannot be removed from a specialized container to ensure that the seed is not lost and mistakenly assumed to be still inside the patient. This container

prevents the imaging probe from making contact with the specimen without specialized hardware that is easily interchanged with the dovetail design.
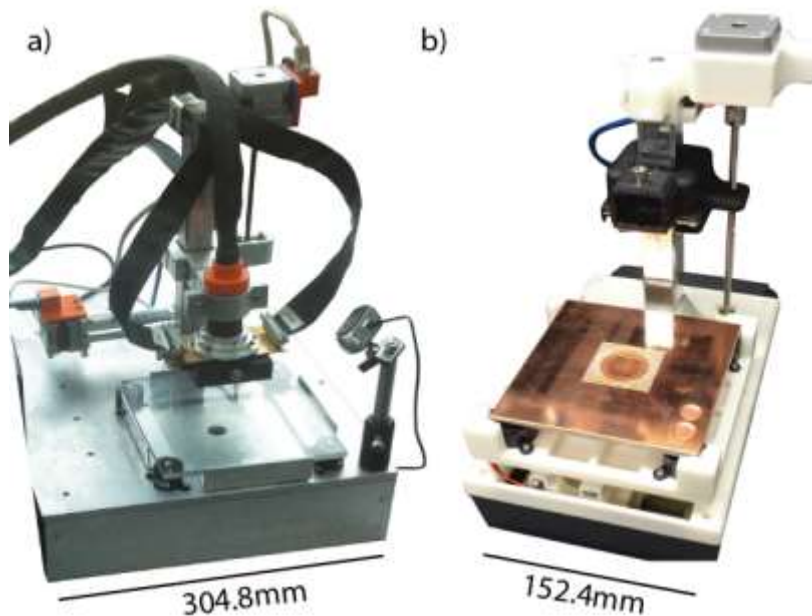

Figure 1.1 Imaging platform generations. a) The second generation platform and b) the optimized third generation device incorporating a copper specimen plate, a modular webcam, and a smaller footprint (152 x 228 x 304 mm compared to 304 x 304 x 406 mm). The feed rate and pressure mechanism is equivalent for the two devices.

Part B. Algorithm Development

Within this section we report extensive enhancements to the data acquisition and processing algorithms leveraged by the spectral imaging system. Comprehensive software development was prompted through limitations experienced during routine clinical use; hardware driver conflicts, undetected cable detachments, improper data labeling, and the lack of a robust acquisition decision tree rendered ~20% of clinical case data unusable in year 5. Detailed below are strategic enhancements for improved case efficacy, ease-of-use, and reduced failure rates.

Methods

A spectral imaging software package was developed based on the software requirements analysis shown below in Table 1.1 The goal of the design was chosen to be semi-automated/user-centered, thus, default parameters and processes were implemented to work

for the majority of users in most circumstances. Furthermore, the views for the graphical user interface were storyboarded based on the high level objectives of the software: 1) automatically find the hardware, 2) initialize the hardware, 3) take measurements to calibrate the hardware, 4) acquire the sample data, 5) process the sample data, 6) determine high-probability regions of disease.

Table 1.1 Software Requirements.

Category	Requirement	Rationale
Functional	• Must be able to read, store, and display spectral data • Must be able to obtain optical properties from spectral data • Must be able to indicate regions of interest on acquired data • Must have device specific default values	• A system that is ready to go with negligible setup will improve the quantity of high quality data.
Behavioral	• Hardware is automatically found and settings loaded • Calibration procedure is required to take measurements • Type of measurement is chosen • If defaults are used, user enters sample information (3 digit number) and measurement starts • Screen automatically changes view as data is acquired • Optical parameters are computed as soon as a "Reflectance Frame" is available • Once complete, user is able to select region of interest. Region of interest is also suggested. Region of interest is translated to central optical axis for marking. • Data anomalies and user errors should be accounted for and handled automatically in software. Each class should have its own error handling modules.	• If the device can be operated by a lay-person, data yield would improve. • An intuitive user-interface helps to ensure data quality • Reducing user decisions avoids unnecessary withdrawals
Structural	• Raw spectral data is represented as a "measurement object" • A series of raw measurements comprise a "Spectral Frame" which can be a calibration, intensity, or reflectance frame. Elements of a frame iterate over all spectral, detector, and illumination channels. Repeated measures are included • A series of frames comprise a "Multivariate Scan" which can be a calibration scan, generic scan over any measurement variable, or a clinical scan including case information. Ex: A raster-scan is a clinical scan over position and pressure • Display panels are structured according to this hierarchy	• A generic method of formatting the spectral data enables device abstraction; any spectral imaging device can be utilized • Separating clinical/calibration/other enables dynamic dispatch of processing/saving functions • Display is simplified by grouping panel elements according to datatype
Performance	• Optical parameter computations cannot be	• Data must be acquired on intra-

- slowed by saving and displaying data, therefore, these operations must be queue-based background threads
- Physical data capture must be less than 15s per single measure frame
- Physical data capture must have execution priority
- Imaging rate (excluding optical parameters) should be less than 1.2cm^2/s
- Optical parameters must be obtained with at a rate of 0.5s/spectrum or less
- operative time scales (25-30 minutes/case)
- Slower imaging rates force poorer resolution, reducing data quality
- Optical parameters need to be visualized soon after the measurement is complete (less than 5 minutes)

To generically handle different modes of acquisition and maintain scalability, an object-oriented design was implemented. The object-oriented G programming language developed by National Instruments© was used to reduce overall development time as the hardware interface protocol libraries are provided in G. Furthermore, the use of an object oriented design aids in meeting the generality design requirement; a hardware abstraction layer (HAL) can was implemented to abstract away hardware functions from hardware specific drivers, reducing hardware specific conflicts. The HAL is diagrammed in Fig. 1.2.
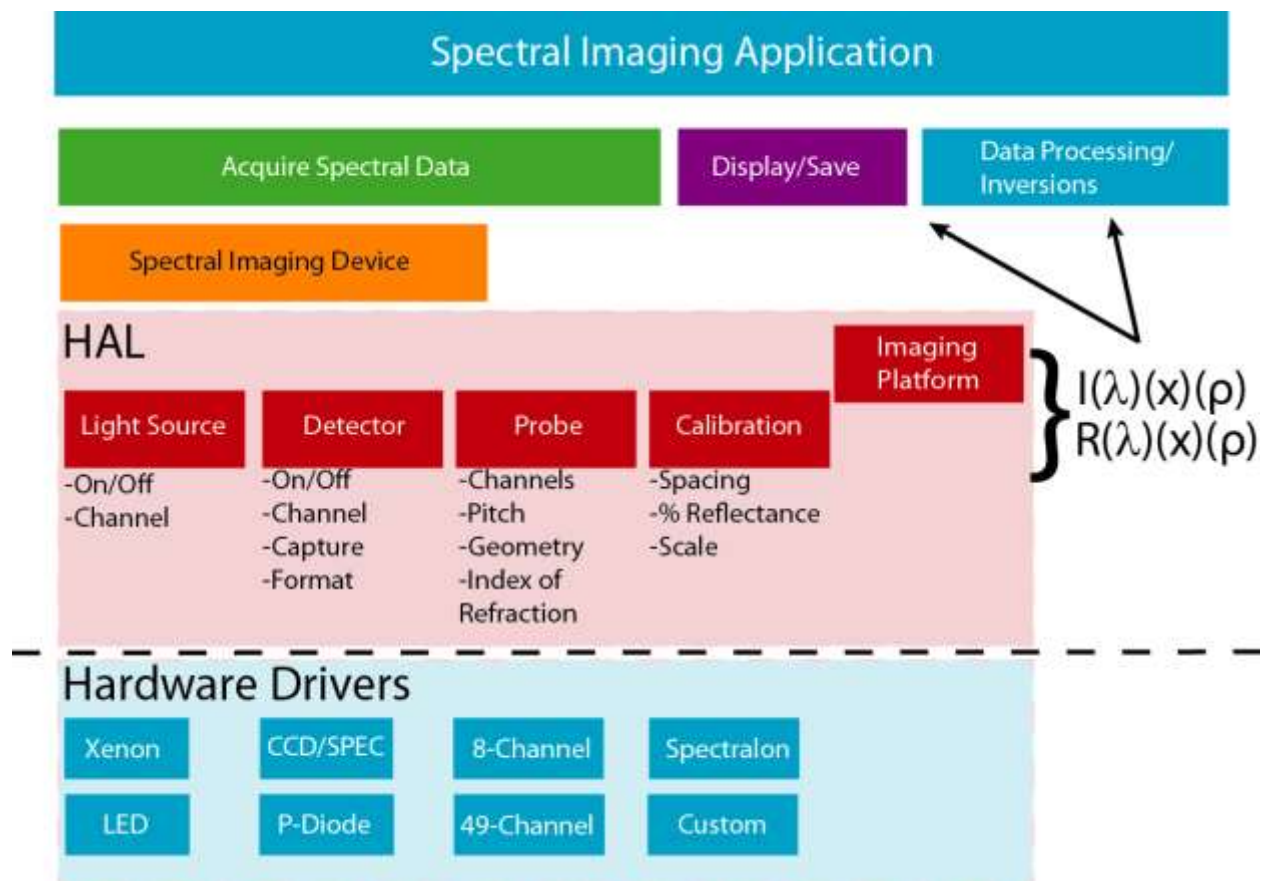

Figure 1.2 Software Abstraction. The software architecture is designed such that fundamental hardware functions are implemented generically to control a spectral imaging device. Typically a spectral imaging device will be comprised of a calibration standard, a light source, a detector, and a probe. Each associated function in the hardware abstraction layer (red) is then over-ridden by the hardware specific drivers(bottom, blue) at run-time. This provides a mechanism to generate spectral data in a generic

format (shown here as a function of position, wavelength, and pressure) that can then be used by the rest of software package regardless of the specific hardware used.

Results

The class hierarchy and grouping is shown in Fig. 1.3. The bulk of the software can be described as a component of 1 of 3 groups; 1) A core group relating to primary application and hardware components, 2) a display group that handles rendering data to the user, and 3), a data group pertaining to formatting, saving, and processing the collected data. The primary classes (Fig.1.3a) consist of: an application class that coordinates general startup, execution, and shutdown of necessary applications, a command class to harmonize requests and data between applications, hardware, and the user, a hardware class to manage each hardware component, and variable class that is used to specify parameters that need to be modified between acquisitions e.g. the next position. When the primary user interface (labeled QDRI) is launched (executable), an initialization routine starts all other needed applications (platform application, data management). Additionally, a "spectral imaging device" object is created consisting of the core components for any spectroscopy system: a light source, an acquisition source, a calibration object, and a probe. The specific drivers are determined by identifying connected hardware, which is done automatically for previous used devices. The user works through a series of panels needed to determine the remaining modules that should be loaded into memory and the type of data that will be collected. To minimize user error, the default parameters are set to known working values for any recognized hardware. The user can change these, but otherwise navigates through each screen in a touch –panel fashion, requiring minimal user decision. When the measurement is started, a series of commands are inserted into a queue that is read by the main application and dynamically dispatched the system and platform child command classes. When generated, the command is typically setup to generate a signal, relay reference information, or collect data based on an independent measurement variable. The utilization of measurement variable classes affords the ability to manipulate the measurement using any modifiable parameter, such as the integration time, light intensity, pressure, or position. The respective command classes call the abstract hardware classes, issuing generic commands that are overloaded by the hardware-specific child classes. The acquired data is pushed onto a queue read by a background thread responsible for managing the data. The data manager interprets all data generically for the current measurement context, allowing the specific data class to override and implement the specifics of the saving, displaying, and processing functions. The software was designed in this manner to achieve maximum scalability; the software package is hardware and acquisition sequence independent.

The data is simultaneously saved and pulled from a second queue to the front panel display: each of these processes are non-deterministic and require parallel execution independent from other time-critical processes. The display classes are determined by the data class and measurement context. The user has the option of allowing the software to dynamically toggle the display panel type, ensuring each measurement action is visible to the user. The spectral data classes are efficiently organized by data complexity: the raw data, the most basic form of data, represents the raw numeric readout obtained from the acquisition hardware. The raw data contains the context in which was acquired (intensity vs background, repeated

measure, etc.) a snapshot of the devices, and is simultaneously inserted into a "spectral frame" according to the context. If a calibration scan has already been completed, the spectral frame is dispatched to a reflectance frame, otherwise it can become an intensity frame or a calibration frame. A frame consists of an array of raw measurements corresponding to a complete, multi-channel spectral snapshot including the repeated measures. A completed frame automatically averages the repeated measures and is displayed on a separate pane. A complete spectral snapshot is captured for every unique measurement variable, collectively representing a "multivariate scan." A scan object contains all variables that are modified during a scan. For example, a raster-scan with an upsample of 8 would generate 64 separate measurement variables each containing one position used in the upsampled parameter maps. Clinical and calibrations scans additionally have properties specific to those scan types; this is later used to generated the correct save path. The final data module is dedicated to intraoperative spectral data inversions (conversion of raw reflectance to optical parameter maps) and is yet another queue-based module. The inverse model utilizes a scalable Monte-Carlo package developed by Palmer *et al* (US 7,570,988) [11-14]. The inversion routine is primarily MATLAB®-based and is called from within LabVIEW™. The routine requires 50-300ms per spectrum and is also non-deterministic due to the fitting algorithm; margin-wide optical parameter maps can be obtained within seconds of raw data acquisition and can therefore be used for intra-operative settings.

When the imaging platform is utilized, a separate imaging platform application is launched with execution priority equal to the main user interface; the movement cannot be interrupted as it will slow the physical data acquisition. Commands are received by the platform application through the platform command class. The imaging platform hardware is managed by a generic imaging platform class composed of a digital camera, a pressure sensor, and an array of movement axes. Similar to the spectral imaging device, the specific hardware functions are dynamically dispatched according to the recognized/specified hardware. A background thread constantly polls the pressure to ensure fine adjustments do not destabilize as a result of data communication lag. The platform application interprets the desired laser location placement based on the mouse cursor position when selecting a region of interest from an optical parameter map and the known scan positions. These ROIs can be chosen automatically, though further diagnostic algorithm development is necessary prior to this being a useful feature.
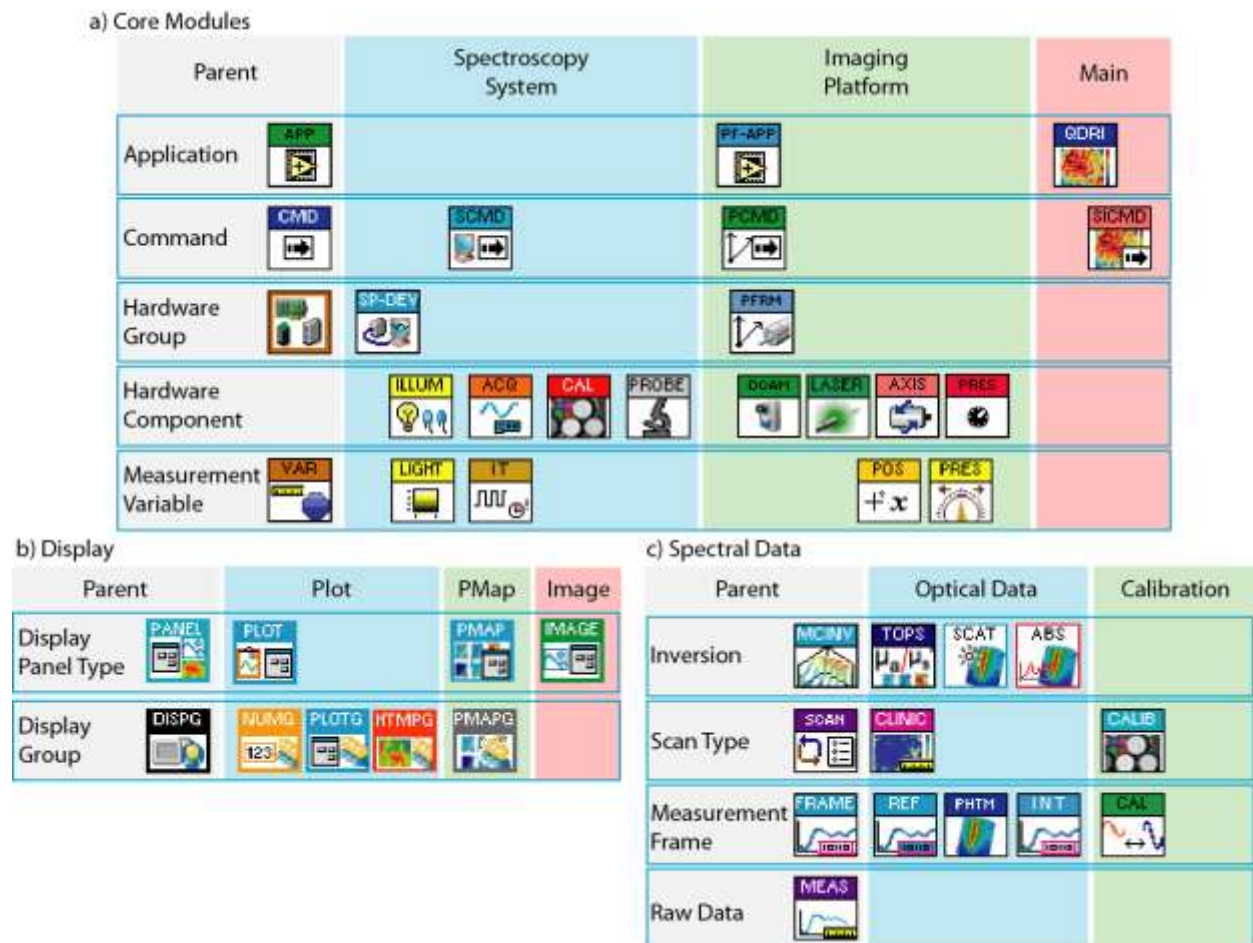
Figure 1.3 Class Hierarchy. The primary core classes are the application, command, hardware, and measurement variable classes, grouped in a) by the spectral imaging system, the imaging platform, and the main user interface. The display classes in b) are grouped by software panel type and indicate the data display groups contained with each. The spectral data in c) is grouped by the data context and respective allowable data types.

Part C. Clinical Study on Margin Assessment:

In previous reports, we saw a substantial proportion of margins (1.5 on average) that presented as positive under pathological review. At Duke University Medical Center (DUMC) the treatment paradigm has significantly changed in the last two years and that number has substantially decreased. The complications associated with small, focal regions of cancerous cells at the margin edge however, remain. Moreover, these regions of positivity are unlikely to be discovered within the current clinical framework; pathologists typically sample lumpectomy specimens at 3-5mm intervals for histopathological review, leaving a substantial risk for these small regions to go undetected. The challenge for any intra-operative technique for breast tumor margin assessment is the ability to detect the signal (i.e., the histologic changes due to varying amounts of malignancy at the margin) over the noise (i.e., the normal inter-patient and intra-patient variation in breast composition). If we view the range of normal tissues in the breast as a "landscape," then the challenge in margin assessment is to detect the presence of malignant

tissue at the boundary of an otherwise ''normal'' margin, as a perturbation in that landscape. The clinical challenges thus warrant a device capable of both a wide coverage area as well (to survey the entire margin) and small feature recognition (to avoid missing focal regions of cancer).

We previously reported on our first generation 49channel+scanning platform device to address the under-sampling/coverage obstacles, wherein optical parameter maps where shown for an oversampled positive and negative margin. As described in the previous section, the technology has extensively matured with strategic software enhancements, automatic digital images, precise automatic positioning, and improved form factor. The goal of these enhancements was to further reduce systematic and user error, improve the acquisition speed and thereby sampling resolution, and to elucidate the effects of resolution on the ability to detect small regions of disease. In this section, we extend the preliminary quantitative analysis presented in year 5 on a cohort of 57 patients.

Methods

Patient Data Collection

Diffuse reflectance spectra were collected from excised breast tissue specimens from 57 patients. For the purposes of this work, patients undergoing breast conserving therapy (BCT) as well as breast reduction surgery were recruited. Specimens (partial mastectomies and reduction mammoplasties) from the respective patient populations were used to compare the optical property values corresponding to dysplastic tissue (partial mastectomy specimens with a positive or close margin), normal tissue (reduction mammoplasty specimens without dysplasia), and additionally normal tissue in the presence of dysplasia (partial mastectomy specimens with negative margins). Partial mastectomy specimen orientation was determined according to surgically placed reference features including: a surgical wire inserted into the center of the tumor, colored sutures, and surgical clips. Specimen faces were defined as the faces of a cube and labeled relative to the specimen orientation in situ; the six measureable faces are hereafter referred to as the superior, inferior, posterior, anterior, medial, or lateral margin. Reduction mammoplasty specimens do not have such a reference system as they are typically not sent to post-operative pathology for assessment.

Immediately following the tissue resection, partial mastectomy specimens are sent to radiology for an intra-operative x-ray examination to verify successful removal of the intended tissue. Upon return, the specimen is then placed onto the pressure sensing base of the imaging platform and oriented accordingly. The raster-scanning procedure is initiated and diffuse reflectance spectra are collected across the visible spectrum (400-700nm). The pressure applied to the face of the specimen is dynamically controlled by a feedback loop that executes in parallel to the main acquisition software, such that subtle adjustments to the applied pressure can be made without interrupting spectrum collection. The specimen is then flipped to its opposing margin and the scan is initiated a second time. Once scanning is complete, a "site-level" inking procedure is performed wherein 6- 10 sites are marked using tattoo ink (typically orange in color) with the aid of a co-registration structure that physically relays the central location of each channel to specimen. The co-registration plate is then removed and the four

corners of the margin are then marked with a different color ink (typically green). A certified pathologist uses these inked dots to provide site-level (orange dots) and gross margin level (green dots) histopathological correlation to the collected spectral channel data. Margin inking was followed by the acquisition of a digital image using an on-board digital camera mounted to the imaging platform.

Clinical Data Processing

Partial mastectomy specimens were measured on the posterior or anterior margins: the pancake-like shape of the excised tissue limited measurements to only two margins. The measurement order is determined *ad hoc* as it is not possible to measure a margin multiple times due to time restrictions, nor is it possible to know with certainty the margin that has the highest likelihood of positivity. A single margin was inked for post-operative pathological assessment in a uniformly spaced diamond pattern. Over the next year, sites will be inked according to the likelihood of being cancerous as designated by our discriminatory algorithm. For this patient data set, tissue optical property maps were reconstructed post-operatively using the inverse Monte-Carlo model discussed previously.

      A dual arm cumulative distribution function (CDF) analysis was performed at the margin level, including all measured samples, and at the site-level, where parameter values corresponded only to regions marked for histological validation. The ability of our spectral mapping technique to survey shifts in of the morphological features of the normal breast was determined by analyzing the spectral information arising from inter-patient variations in mammographic breast density (MBD), which further established the morphological features to which the hyperspectral maps are sensitive. A two-sided Kolmogorov-Smirnov statistic p-value was used to determine if tissue-specific optical parameter distributions were from a common parent distribution, effectively summarizing our ability to categorically discern tissue subtypes. A conditional inference tree model (CIT) previously reported by our group [15] was used to further stratify tissue margins high and low breast density subgroups (HBD and LBD, respectively).

Patient Population

The following characteristics were recorded for each patient (if available): radiographic breast density, menopausal status, neoadjuvant treatment status (chemotherapy or endocrine therapy), age, body mass index (BMI), and surgical re-excision status. For the analyses presented herein, data was only included from patients who had not undergone prior radiation, adjuvant treatment, or surgery 1) due to limited sample sizes and 2) in order to assess differences in surgical margin status without these additional confounding factors. For mammographic breast density (MBD), each patient was assigned a value based on their pre-surgery mammogram: 1 (fatty), 2 (scattered fibrous), 3 (heterogeneously dense), or 4 (extremely dense). MBD score of 1 or 2 was considered to be low density, while a score of 3 or 4 was considered to be high density; the data was binned this way since the majority of the patients had 2's or 3's.

Table 1.2 Patient Demographics

# of patients included in analysis	57
Surgical Margin Status (margins, patients)	**(71, 57)**
Positive	3 (4%), 3 (6%)
Negative	38 (53%), 31(56%)
Close (Negative)	30 (42%), 21 (38%)
Avg. age (range)	63.8 (41-92)
Avg. BMI (range)	29.8 (18.3 - 47.1)
Specimen Volume (Ellipsoid)	23.0 (1.2 – 79.5) cm^3
Tumor receptor status (invasive only)	
ER +, -	40 (70%), 8 (14%)
PR +, -	35 (61%),13 (22%)
HER-2/neu +/-	0 (0%), 37 (65%)
Triple negative	5 (9%)
Menopausal Status	
Pre	8 (14%)
Peri	0 (0%)
Post	49 (86%)
Breast density*	
1	9 (16%)
2	31 (54%)
3	15 (26%)
4	2 (4%)

Clinical Imaging

Clinical raster-scanned images were acquired for 57 patients at an upsample rate of 8, resulting in 64 full frame spectral images (3136 full spectrum pixels) for each margin measured. Of the 6 possible margins, 2 were measured (anterior/posterior) in most cases due to the pancake-like shape of most specimens. The ratio of [β-carotene]/μ_s' has previously been established by our group as a valuable diagnostic parameter [15, 16].

Results

Data Analysis

The relationship between optical parameters and benign breast tissue composition has been well established by our group in prior publications [15-17]. Briefly, it has been determined that the ratio of [β-carotene] to $<\mu_s'>$ decreases as the tissue changes from predominantly adipose tissue to predominantly fibroglandular tissue components. This manifests as a left shift of the empirical CDF corresponding to all pixels with a given [β-carotene] /$<\mu_s'>$ parameter map. Furthermore, the ability to quantify and distinguish these changes is greatly enhanced the patient population is stratified by breast density. In this study, we sought to corroborate

previous results using the 57 patient cohort of tissue margins. Fig. 1.4 shows representative margin images for a positive, HBD margin (Fig. 1.4a), a positive, LBD margin (Fig. 1.4b), a negative, LBD margin (Fig. 1.4c), and a negative, HBD margin (Fig. 1.4d). Shown in Fig. 1.4(e-f) are corresponding CDFs for the entire cohort. Note that only 3 margins were found to be truly positive. This is due to continually evolving standard of practice.
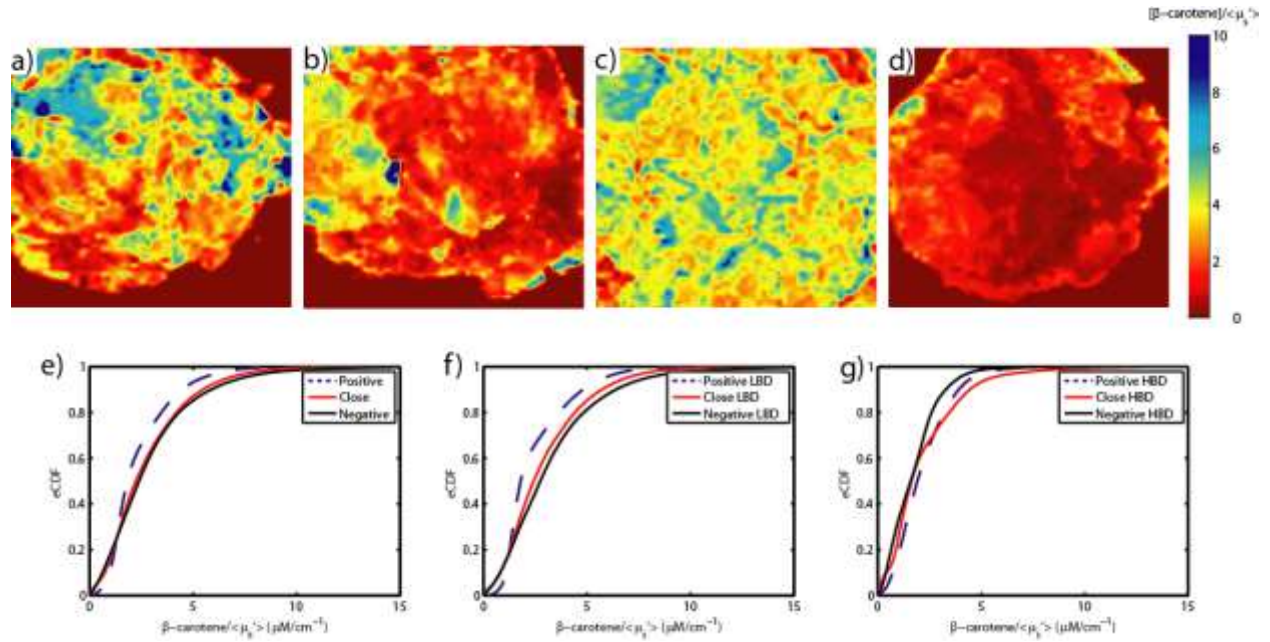

Figure 1.4 Optical differences in breast tissue associated with density. ,Maps of [β-carotene]/μ_s' shown for a), a positive, LBD margin, b), a positive, HBD margin, c), a negative, LBD margin, and d), a negative, HBD margin. Cumulative distribution functions are shown for e), all positive margins (n=3), all close margins (n=30), and all negative margins (n = 38), f), the corresponding low density margins (n = 2, 24, 30, respectively), and g), the corresponding high density margins (n = 1, 6, 8, respectively). Note that not all patients in the cohort had an associated breast density.

Typically, lower [β-carotene]/μ_s' values can be explained by the proportions of tissue typical to these breast density grades. Low density breasts are likely to have higher proportions of fatty tissue and therefore present with a naturally higher β-carotene concentration (thereby increasing the ratio). Likewise, high density breasts have higher proportions of collagen and glandular tissue, which manifests as an increase in the scattering signal. These effects are well summarized by the directional shift of the eCDFs: fatty tissue associated with the LBD margin has shifted the curve to right, fibrous tissue has shifted curve corresponding to the HBD margin to the left. Fig. 1.5 shows the eCDF trends for the entire patient cohort. Interestingly, in the case of the positive margins shown in Fig. 1.4, it appears that for dense breasts, the [β-carotene]/μ_s' ratio may not be appropriate for distinguishing benign from malignant tissue regions. This is paralleled in clinical practice; most positive margins are observed in abnormally dense breasts as the tumor boundary is not macroscopically apparent[18].
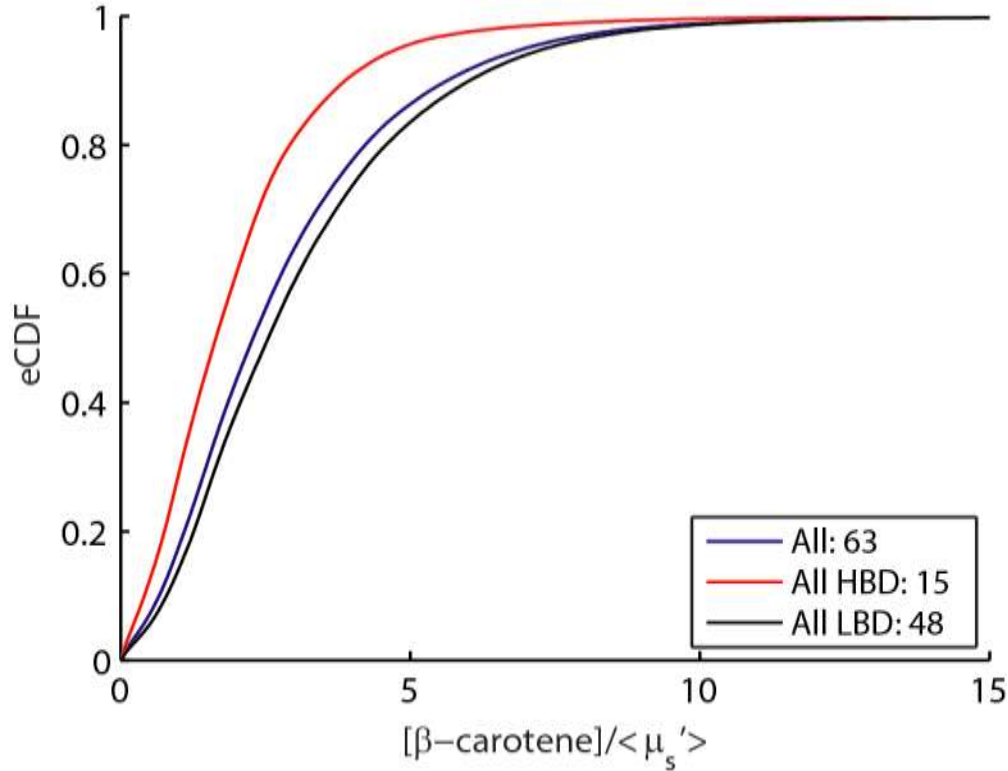
Figure 1.5 Combined CDFs for all low and high breast density samples. Empirical cumulative distribution functions (eCDFs) of all margin level data for all high and low breast density samples.

The Kolmogorov-Smirnov (KS) test was used to determine if these distributions are statistically likely to originate from a common underlying distribution. The KS test considers both the shape and size differences when comparing distributions, and is often used in the context of CDFs to quantify the distance between an empirical and a cumulative distribution function and can be considered a goodness of fit. HBD and LBD margins were found to be statistically different (p<.02) at the margin level for the cohort used in this analysis.

We performed a similar analysis at the site level using all available pathology-confirmed sites from the same patient data set. Site designations with n<8 were excluded from this analysis due to insufficient statistical power. Of the 234 selected sites, 105 were primarily composed of fat (labeled adipose), 23 were a mixture of fibrous tissue and fat tissue (fibroadipose), 10 were a mixture fibrous and glandular tissue (fibroglandular), 71 were a mixture of fat and fibroglandular tissue, 8 sites included regions of DCIS 0.1-2mm from the margin surface, similarly 6 sites included some invasive carcinoma 0.1-2mm from the surface. We chose to augment our analysis of site-specific distribution dependencies by also investigating how these change when lower/higher resolutions are used. Figure 1.6 shows the site level CDFs for each of these tissue compositions at the highest and lowest resolution used in this study (0.75mm/6mm).
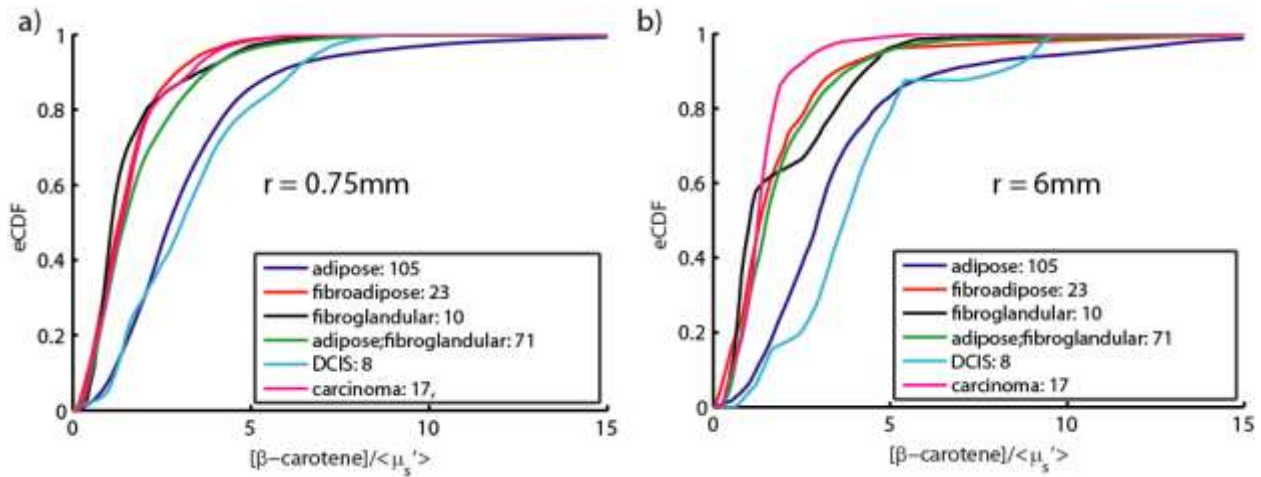
Figure 1.6 eCDFs for all site-level data. Empirical cumulative distributions for eligible pathology confirmed tissue sites. a) corresponds to distributions taken with the highest upsample (n=8) and correspond to the best resolution (0.75mm) and, b) represents the corresponding distributions measured using the native probe resolution (6mm).

Not surprisingly we discovered that as the adipose content is increased, the CDF tends to shift to the right. At the highest resolution used, each of these tissue subtypes are statistically distinct from one another, with the exception of fibroglandular and "carcinoma" tissues (p>.0001). Interestingly, adipose tissues are statistically different from fibroadipose tissues at the highest upsample (p<.0001) but not at the lowest, suggesting that the signal from fibrous components are washed out at low resolution. Similarly, fibroglandular tissue is no longer distinguishable from the fibroglandular/adipose mix as you decrease in resolution. Interestingly, the ability to distinguish "close" DCIS sites degraded with improved resolution. It is suspected that this may be due to the manner in which the region is selected; it may very well be the case that only a few pixels correspond to the truly dysplastic region while the remaining correspond to neighboring fat cells. This suggests that a region extraction algorithm could be used to pinpoint smaller regions of focal disease by locating distinct boundaries within a suspect area. The inability to distinguish pure fat from other tissue types suggests that sub-pixel sampling is imperative to accurately diagnose the margin landscape.

Aim 2: Optical quantitative biology of different breast cancer subtypes.
Part A – Duke University
The objective of the work in Aim 2 is to use optical techniques to measure markers of the tumor microenvironment in women with cancers representing a wide variety of subtypes, and to determine whether these optical measures can be used for real time diagnosis or to predict eventual chemotherapy response in a subset of the patients who are measured prior to commencement of chemotherapy. One such approach that we have discussed in previous years is to use a high resolution microendoscope (HRME) combined with a morphological stain

called acriflavine to visualize the tissue morphology in real time. In previous years we demonstrated the feasibility of using the HRME for detection of residual carcinoma in the normal tissue milieu and validated our unique image analysis approach on preclinical murine tumor margin specimens and small cohort of clinical mastectomy samples. Additionally, we completed a large study using the HRME to capture morphologically based information from biopsy specimens. Last year, we continued to image biopsy specimens, identified several quantitative endpoints to distinguish malignant from benign tissues, and laid the groundwork to build a diagnostic classification model. In year 5, we optimized our diagnostic model to yield the optimal separation between positive and negative biopsies. This included identifying endpoints/parameters that have diagnostic potential, optimizing how we summarize the data from each biopsy, and building predictive models that quantitatively diagnose high resolution images. Together, this work yielded an optimized set of tools that are capable of imaging thick tissue at high resolution with no tissue processing and that can automatically segment and quantify those specimens.

Introduction

Histopathology is the clinical standard for tissue diagnosis. Pathologists examine high resolution images of small volumes of fixed, sectioned, and stained tissue [19]. When diagnosing cancer in particular, pathologists look for changes in tissue morphology including changes in nuclei and surrounding tissue. Nuclear changes that may indicate the presence of cancer include pleomorphism, increased nuclear-to-cytoplasmic ratio, increased nuclear density (hyperchromasia), decreased chromatin organization, and increased mitotic rate [20, 21]. Changes in the surrounding tissue include the presence of reactive stroma, which is composed of connective tissue, blood vessels, macrophages, lymphocytes, other inflammatory cells, and the presence of progressive infiltration, which involves the invasion and destruction of surrounding tissue [20, 21]. While histopathology is the gold standard, limitations include tissue processing, sectioning and staining the tissue, which can take 30 minutes or more for frozen section diagnosis and more than 24 hours for paraffin section diagnosis, and a highly trained pathologist to render a diagnostic evaluation.

Several clinical situations could benefit from more rapid and automated histological processing, which could reduce the time and resources required between obtaining tissue and providing a diagnosis. For example, there is need for rapid detection of residual cancer on the surface of tumor resection specimens acquired during excisional surgeries, such as breast conserving surgery (BCS) [22]. Post-operative histopathologic assessment of the resected specimen is the current gold standard by which microscopic residual tumor in the margin is detected. Re-excision surgery is performed if residual cancer is found at or within 2 mm of the surface of the excised lumpectomy specimen, in order to reduce the risk of recurrence [23]. No tools for intra-operative margin assessment have been widely accepted. Intra-operative frozen section analysis and touch prep cytology are used to assess surgical margins at the time of first surgery at a few select high-volume centers with dedicated resources and personnel. However, these techniques have not been widely adopted because they require laboratory personnel to be present during surgery including specially trained pathologists and sometimes radiologists. An additional clinical scenario that could benefit from more rapid histological processing is the

assessment of biopsy specimens at the point of care to confirm that a suspicious lesion is successfully sampled, preventing an unnecessary repeat biopsy procedure. Rapid and low cost histological processing could also be potentially useful in settings lacking the resources necessary to perform standard histologic assessment [24]. For example, intermediate diagnostic biopsy is typically not performed between cancer screening and treatment in low and middle income countries (LMICs) due to the need for multiple visits (there is patient attrition with every clinic visit that is needed) and lack of resources [25]. The number of pathologists in LMICs is small, even as a percentage of the total medical workforce. For example, there are only 15 pathologists in the entire country of Tanzania, which translates to 1 pathologist per 2.5 million people [25]. Technologies that enable rapid, automated, low cost histological processing could be placed in the hands of other health care workers, such as nurses or community health care workers, in order to address this unmet clinical need in LMICs.

In order to enable visualization of tissue at the point-of-care, many groups have developed microscopy techniques including reflectance and fluorescence microscopy [26-30], confocal microscopy [31-35], and optical coherence tomography (OCT) [36-41] and demonstrated that morphological features can be detected with these approaches. While these techniques are well suited to enable real-time visualization of tissue morphology, quantitative image analysis is essential to enable objective interpretation and automated diagnosis. Towards this end, a few groups have combined automated nuclear morphometry and microscopy techniques to enable quantitative diagnosis during a procedure. For example, Nyirenda et al. applied nuclear morphometry to wide-field fluorescence microscopy images of a breast cancer rat model and found that area fraction, which is the nuclear area divided by the total area, achieved 97% sensitivity and 97% specificity for tumor detection [42]. Previously, our group used a high-resolution fluorescence microendoscope in combination with a topical contrast agent called acriflavine to enable visualization of the microanatomical features in resected preclinical tumor sarcoma margins [43]. We developed a strategy for isolating acriflavine positive features (APFs) from the heterogeneous sarcoma margins using a technique called sparse component analysis (SCA) [43], which has been used in the image processing community for image compression. While APFs roughly correspond to nuclei, in some cases nucleic acids are concentrated within the nucleoli of neoplastic cells; therefore, we refer to these acriflavine positive features as APFs throughout this work. SCA accurately isolated APFs from images that contain tumor, muscle, and adipose tissue types and differences in nuclear density were used to identify pathologically confirmed positive tumor margins [43].

The goal of our current study was to test the robustness of our quantitative microscopy tool box to detect the presence of malignancy in clinical core needle breast biopsies, and to assess if this approach can be extended from a preclinical sarcoma model to clinical specimens for point-of-care procedures associated with breast cancer diagnosis and/or margin resection. A model was optimized on individual images for which we had a corresponding pathologic diagnosis. Then the model was prospectively applied to the entire biopsy panel to assess if our approach could be used to diagnose whole biopsy specimens.

Methods

Patient Population: This study was performed under a protocol approved by the Duke University Institutional Review Board (Protocol Number: Pro00008003). Eighty patients age 18 and over undergoing core needle breast biopsy procedures at Duke University Medical Center gave written consent before enrolling into the study. In addition to imaging tissue, characteristics were tabulated for each patient including age, body mass index (BMI), receptor status, menopausal status, and mammographic breast density (MBD). For MBD each patient was assigned a value based on their pre-surgery mammogram: 1 (fatty), 2 (scattered fibroglandular), 3 (heterogeneously dense), or 4 (extremely dense). This demographic information is included in Table 2.1.

Imaging system and contrast agent: A high resolution fluorescence microendoscope that has been described previously [44] was used to capture images of breast tissue. Briefly, the microendoscope contained a 455 nm light emitting diode, excitation filter, dichroic mirror, 10x objective, emission filter, and CCD camera. The light was directed to the sample through a flexible fiber bundle composed of 30,000 fibers that yielded a circular field of view of approximately 750 µm in diameter. The resolution of the system was approximately 4.4 µm. Acriflavine was selected as a topical contrast agent because it highlights tissue morphology seconds after being applied. Specifically, acriflavine reversibly associates with RNA and DNA, and has also been shown to stain collagen and muscle fibers [45, 46]. Acriflavine was dissolved in phosphate buffered saline solution (0.01% w/v, Sigma-Aldrich) and was topically applied to excised breast tissue immediately prior to imaging with the microendoscope.

Imaging protocol: During core needle breast biopsy procedures several biopsies were taken from the suspicious area. Our research team was usually handed the first biopsy acquired, which typically came from the center of the suspicious lesion. This was not a research biopsy collected for our particular study; rather our research team intercepted the first biopsy collected before it was sent to the pathology laboratory. After the biopsy was acquired (typically within 10 minutes of the procedure being performed), acriflavine was applied to the surface of the specimen. After 30 seconds, the distal end of the fiber bundle was placed into contact with the tissue and images were acquired. The biopsy was scanned length-wise by systematically moving the probe in 1 mm increments over the tissue surface. Once one side was scanned, the biopsy was rotated 180 degrees and the length-wise scanning process was repeated. In order to improve the accuracy and reproducibility of these movements the fiber bundle was secured in a custom probe holder which was mounted on an x-y translation stage. Biopsies ranged from 10-20 mm in length and imaging took approximately 10-15 minutes to complete.

After imaging was completed the surface of the specimen was inked for pathological co-registration. In order to maintain the proper orientation for pathological evaluation, each half of the biopsy specimen was inked with a different color (see Figure 2.1). After imaging and inking were complete, the tissue was returned for standard pathologic processing, and the resulting H&E stained slides were reviewed by a breast pathologist (J.G.) who was blinded to the results of fluorescence microscopic imaging. A diagnosis was acquired for the ends of each biopsy (the last 1 mm, which we refer to as the site level diagnosis) as well as for the middle portion of each biopsy   (the central 8-18 mm, which we refer to as the biopsy level diagnosis). Since each end

of the biopsy was imaged twice, 4 images were acquired of the ends for each biopsy specimen. The middle portion of the biopsy ranged from 8-18 mm. Since images were acquired every 1 mm and the middle portion was also imaged twice, between 16 and 36 images were acquired of the middle portion of each biopsy specimen.
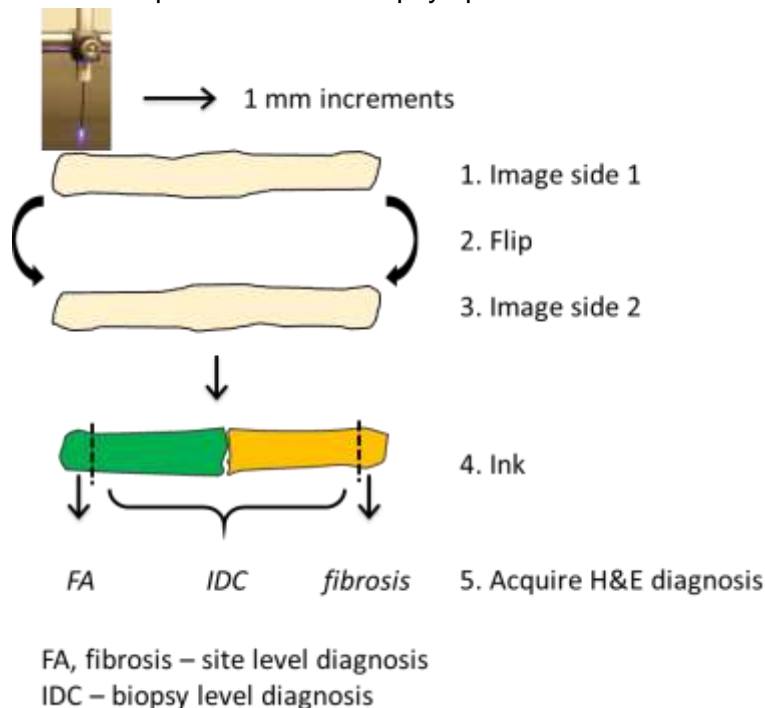

Figure 2.1. Illustration of imaging and inking protocol. First acriflavine was topically applied to the biopsy, and side 1 was imaged by moving the probe in 1 mm increments along the length of the biopsy. Then the biopsy was flipped 180 degrees, and side 2 was imaged in 1 mm increments. Next the biopsy was inked with two colors – for example, green ink was applied on the left side, and orange ink was applied on the right side. Then the biopsy was submitted for H&E processing and a three-part diagnosis was given – one diagnosis for each end (the last 1 mm, which we refer to as the site level diagnosis), and another aggregate diagnosis for the middle component (the center 8-18 mm, which we refer to as the biopsy level diagnosis).

Site level analysis: In order to develop a model to distinguish between positive and negative biopsies, a site level analysis was performed where each inked site had co-registered pathologic diagnosis. Specifically, the images that are located at the ends of each biopsy for which we have specific pathology diagnoses were examined in order to establish expected trends in diameter and density. A total of 80 patients were recruited for this study. However, 5 patients were used for a feasibility study prior to 2011. 8 patients were counted as screen fails because they became ineligible after consenting to the study. 8 patients were excluded from the study due to various logistical issues. In total our study team was able to successfully image 59 biopsy specimens with a corresponding pathologic diagnosis, 5 of which were stereotactic core biopsies and 54 of which were ultrasound guided core needle biopsies. For our analysis, the 5 stereotactic biopsies were removed from the data set because the samples were extremely fatty. This information is summarized in Figure 2.2.

In total, our group imaged 54 ultrasound guided biopsies for which a pathological diagnosis was obtained (see Figure 2.2), and since each of the 108 ends were imaged twice (as illustrated in Figure 2.1), this yielded 216 total images. However, a diagnosis for several specimens could not be acquired due to fragmentation of the biopsy or lack of ink. Due to a lack of diagnosis, 19 biopsy ends which corresponded to 38 images were lost. Additionally, only ends of the biopsies that were consistent with the biopsy (middle) level diagnosis were retained for further analysis. For example, many biopsies that contained invasive ductal carcinoma (IDC) had ends that contained adipose or fibrous tissue. The relevant pathology (such as IDC) always resided in the middle of the biopsy; there were no cases in which the ends were positive and the middle was negative Because the biopsy tissue was elastic and easy to expand and contract during imaging, we could not ensure that these images were truly negative; therefore these sites were removed. In total 26 biopsy ends, which corresponded to 52 images were removed because the ends of the biopsies were inconsistent with the biopsy level diagnosis. The remaining images were reviewed for quality control. Images were removed from the data set if there was little to no acriflavine staining present or the image was out of focus. Based on these criteria, 60 images were removed because they had little to no staining and 14 images were removed because they were out of focus. This yielded 52 quality images with a corresponding site level pathology diagnosis. Details of the exclusion criteria listed above are summarized in Figure 2.2.
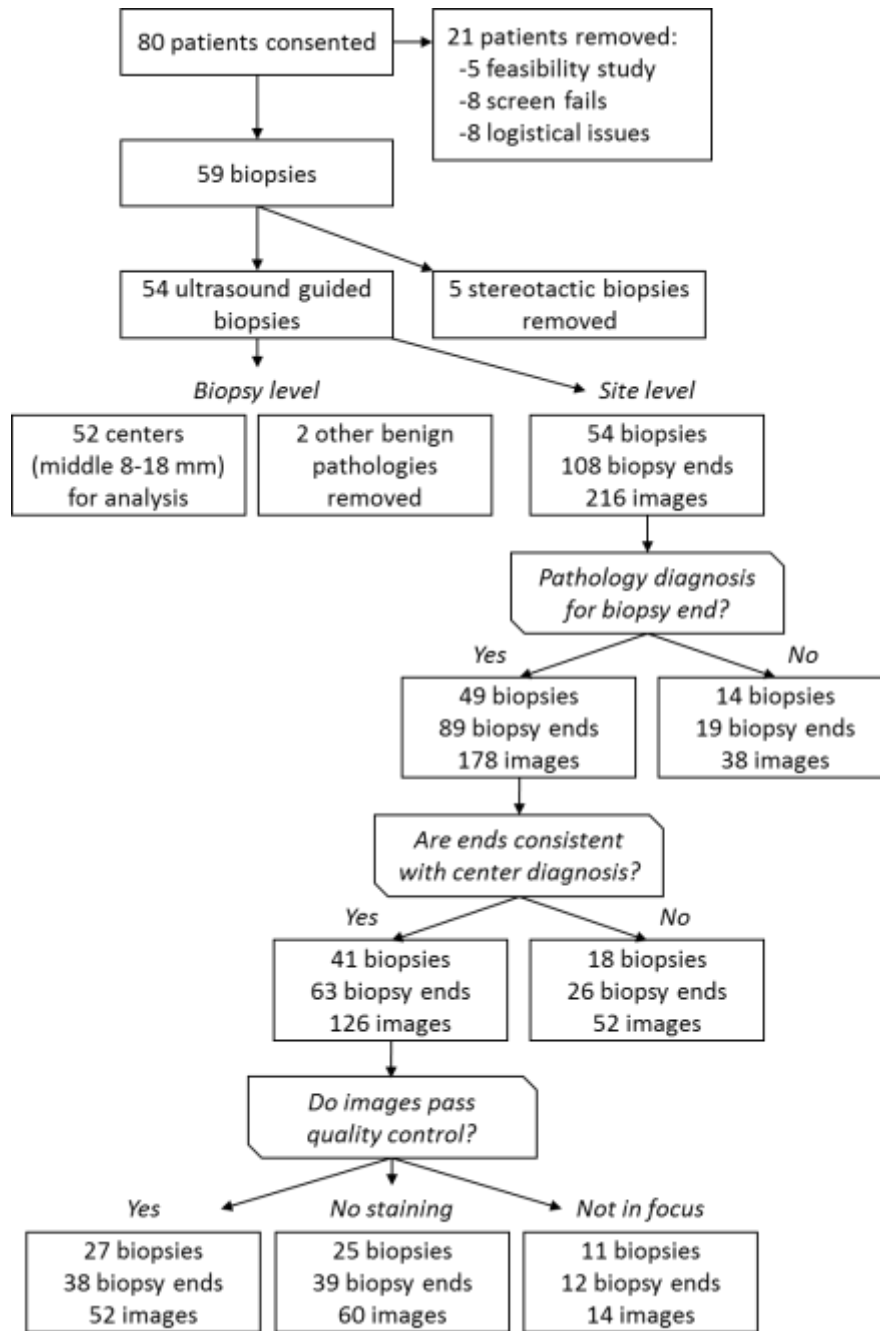
Figure 2.2. Inclusion criteria for site level training data set and biopsy level validation data set.

Acriflavine positive features (APFs) were segmented through applying a technique called sparse component analysis (SCA), which has been described previously [43]. All image processing and analysis was completed in MATLAB (2013b, Mathworks Inc., Natick, MA). First, images were cropped in order to discard the rim of the fiber bundle. Additionally, a low pass Gaussian filter was applied to remove the fiber core pattern that was superimposed onto the images. Next, SCA was used to separate APFs from muscle and adipose structures in heterogeneous images. After SCA was applied to isolate APFs, the circle transform (CT) was applied to compute the size and density of APFs. CT was chosen to quantify variables because it detects approximately

circular objects (i.e. APFs), can distinguish overlapping circular APFs, and is easy to tune [47].

Next, variables were calculated from segmented images. Variables were designed to capture disease features typically seen in H&E stained slides, such as increased nuclear density or nuclear pleomorphism (the variation in size and shape of nuclei) [20, 21]. Specifically, variables include density of APFs (the number of APFs in a unit area), area fraction (the total APF area divided by the total area), minimum inter-nuclear distance (the distance between the center of an APF and the center of the next closest or nearest neighboring APF), and diameter (the output given by CT). Density and area fraction (AF) represent scalar variables – only one value is returned for each image, while the minimum internuclear distance (IND) and diameter represent vector variables – a value is calculated for each APF in the image. In order to consolidate the vector variables into a scalar value, the mean IND and mean diameter were calculated for each image.

Different combinations of the variables described above were investigated through using the site level data set to evaluate performance of the different multivariate models. Multivariate models were based on logistic regression in the SAS programming environment. For each model, receiver operator characteristic (ROC) curves were constructed for the site level data set using a web-based tool [48]. The area under the curve (AUC) associated with each ROC curve was tabulated. Additionally, the cross-validated probabilities for each image were determined in SAS using leave one out cross-validation and then used to construct a cross-validated ROC curve.

Biopsy level analysis: The models developed using the site level data set were applied to the biopsy panels listed in Figure 2.2 and Table 2.3. Biopsy panels consisted of the images in the central 8-18 mm (as illustrated in Figure 2.1), and did not include the ends (the last 1 mm), which were used exclusively in the site level analysis described above. The probability that each image was malignant was determined by applying the models. The number of images that had a probability of greater than or equal to chance (50%) was tabulated and used to create ROC curves. The model that yielded the highest AUC for the biopsy data set was selected and used to examine which biopsies were correctly and incorrectly classified. A cut point on the ROC curve was selected based on the quantity $F = (1\text{-sensitivity})^2 + (1\text{-specificity})^2$, which is minimized at the optimal sensitivity and specificity.

Results

Demographic information: The breakdown of the 54 ultrasound guided biopsies specimens imaged in this study is shown in Table 2.1. Of the 54 biopsies, 23 were malignant and 31 were benign specimens. The 23 malignant cases were comprised of 20 invasive ductal carcinomas (IDC), 2 invasive lobular carcinomas (ILC), and 1 ductal carcinoma *in situ* (DCIS). Of the 31 benign biopsies, 2 contained primarily adipose or fibroadipose tissue, 21 contained primarily fibroglandular, fibrous, or glandular tissue, 6 were either fibroadenomas or papillomas and 2 contained other benign pathologies including a lymph node and a hematoma.

Table 2.1. Patient Demographics.

Characteristic	Biopsies

# of patients included in analysis	54
Primary histology	54
Malignant and premalignant	23 (42.6%)
Invasive ductal carcinoma (IDC)	20 (37.0%)
Invasive lobular carcinoma (ILC)	2 (3.7%)
Ductal carcinoma in situ (DCIS)	1 (1.9%)
Benign	31 (57.4%)
Adipose, fibroadipose	2 (3.7%)
Fibroglandular, fibrous, glandular	21 (38.9%)
Fibroadenoma, papilloma	6 (11.1%)
Other (lymph node, hematoma)	2 (3.7%)
Avg. age (range)	53.1 (19 - 85)
Avg. BMI (range)	31.5 (17.6 – 61.7)
Tumor receptor status (invasive only)	
ER +, -	16 (72.7%), 6 (27.3%)
PR +, -	15 (68.2%), 7 (31.8%)
HER-2/neu +/-	2 (9.1%), 20 (90.9%)
Triple negative	5 (22.7%)
Menopausal Status	
Pre	19 (35.2%)
Peri	1 (1.9%)
Post	34 (63.0%)
Breast density*	
1	1 (2.1%)
2	18 (37.5%)
3	24 (50.0%)
4	5 (10.4%)

*Breast density was acquired for 48 out of 54 patients since 6 mammograms were taken at other institutions.

Site level analysis: Table 2.2 shows how many images fell into each pathological category for the site level images. A total of 52 sites were imaged which included 14 malignant and premalignant sites and 38 benign sites. The 14 malignant sites included 12 IDC and 2 DCIS images. The benign sites were comprised of 15 adipose and fibroadipose images, 20 fibroglandular, fibrous, and glandular images, and 3 fibroadenoma or papilloma images.

Table 2.2. Site level data set

Primary histology	Sites
# of sites	52
Malignant and premalignant	14 (26.9%)
Invasive ductal carcinoma (IDC)	12 (23.1%)
Ductal carcinoma in situ (DCIS)	2 (3.8%)
Benign	38 (73.1%)
Adipose, fibroadipose	15 (28.8%)

Fibroglandular, fibrous, glandular	20 (38.5%)
Fibroadenoma, papilloma	3 (5.8%)

Representative images taken from the site level data set are shown in Figure 2.3A. Images of the corresponding H&E sites are shown in column 1. While H&E images and fluorescence images were acquired from approximately the same region of the biopsy, exact co-registration was not possible due to pathologic processing. Images acquired with the high resolution microendoscope are shown in column 2. For visualization purposes, APFs that were larger than 7 μm in diameter were false colored red and APFs that were less than or equal to 7 μm in diameter were false colored green and overlaid onto the original image (column 3). The threshold of '7 μm' was chosen because APFs smaller than the threshold are likely to correspond to nucleoli, while APFs larger than the threshold are likely to correspond to nuclei [49]. Specifically, others have found that nuclear volume of human breast cancer cell lines ranged from approximately 200 to 1500 μm^3 while nucleolar volume ranges from 5-170 μm^3 [49]. If the assumption is made that nuclei and nucleoli are approximately spherical, this corresponds 7-14 μm in diameter for nuclei and 2-7 μm in diameter for nucleoli, suggesting that threshold of '7 μm' may lead to some separation between nuclei and nucleoli. The resolution of our system is 4.4 μm; thus, our system can resolve nuclei and larger nucleoli in the range of 5-7 μm.
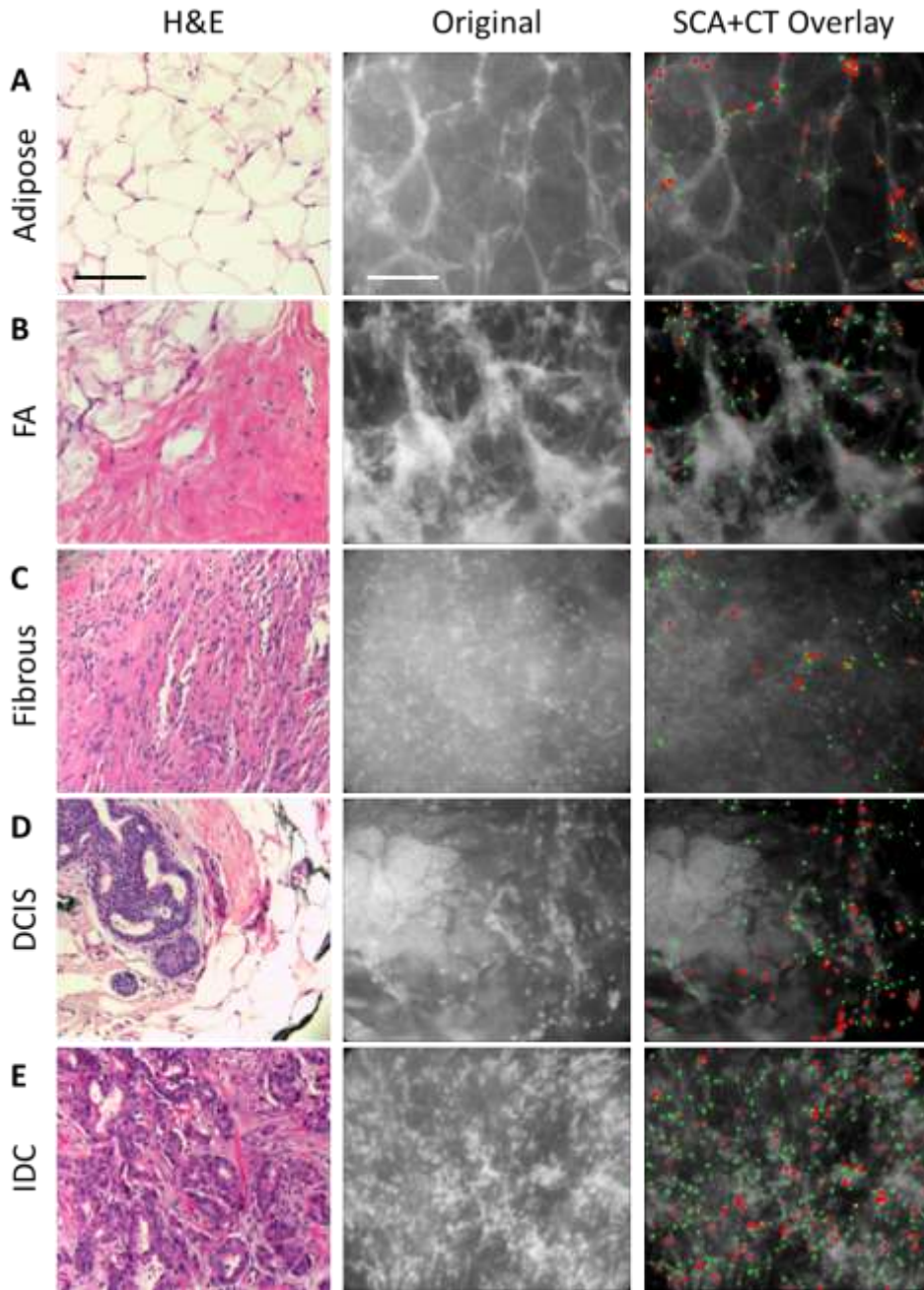
Figure 2.3. Application of sparse component analysis (SCA) and circle transform (CT) to representative images of adipose, fibroadipose (FA), fibrous, ductal carcinoma in situ (DCIS), and invasive ductal carcinoma (IDC) are shown in A-E respectively. Images of the corresponding H&E site are shown in column 1. The original images are shown in column 2. An overlay is shown in column 3 in which the smaller acriflavine positive features (APFs) (<7 μm diameter) are false colored green and the larger APFs (≥7 μm diameter) are false colored red. The background was dimmed to enhance visualization in the overlay. Both scale bars are 200 μm.

Figure 2.4A-C shows boxplots of density, area fraction (AF), and average inter-nuclear distance (IND), calculated from malignant (n=14), adipose and fibroadipose (n=18), fibroglandular, fibrous, and glandular (n=20), and fibroadenoma and papilloma (n=3) images. Density, AF, and average IND were calculated for all APFs, smaller APFs (green), and larger APFs (red). As expected, each density and AF boxplot reflected higher concentrations of APFs for the malignant compared to the benign tissue types. The density of the smaller APFs (green) yielded the most significant difference between malignant and benign images (p = 1.8 x 10^{-6}). Similarly, AF and average IND of the smaller APFs (green) led to the most significant differences between malignant and benign images. No significant differences in average diameter were seen between malignant and benign images (p = 0.54); therefore, diameter was not included in subsequent analysis.
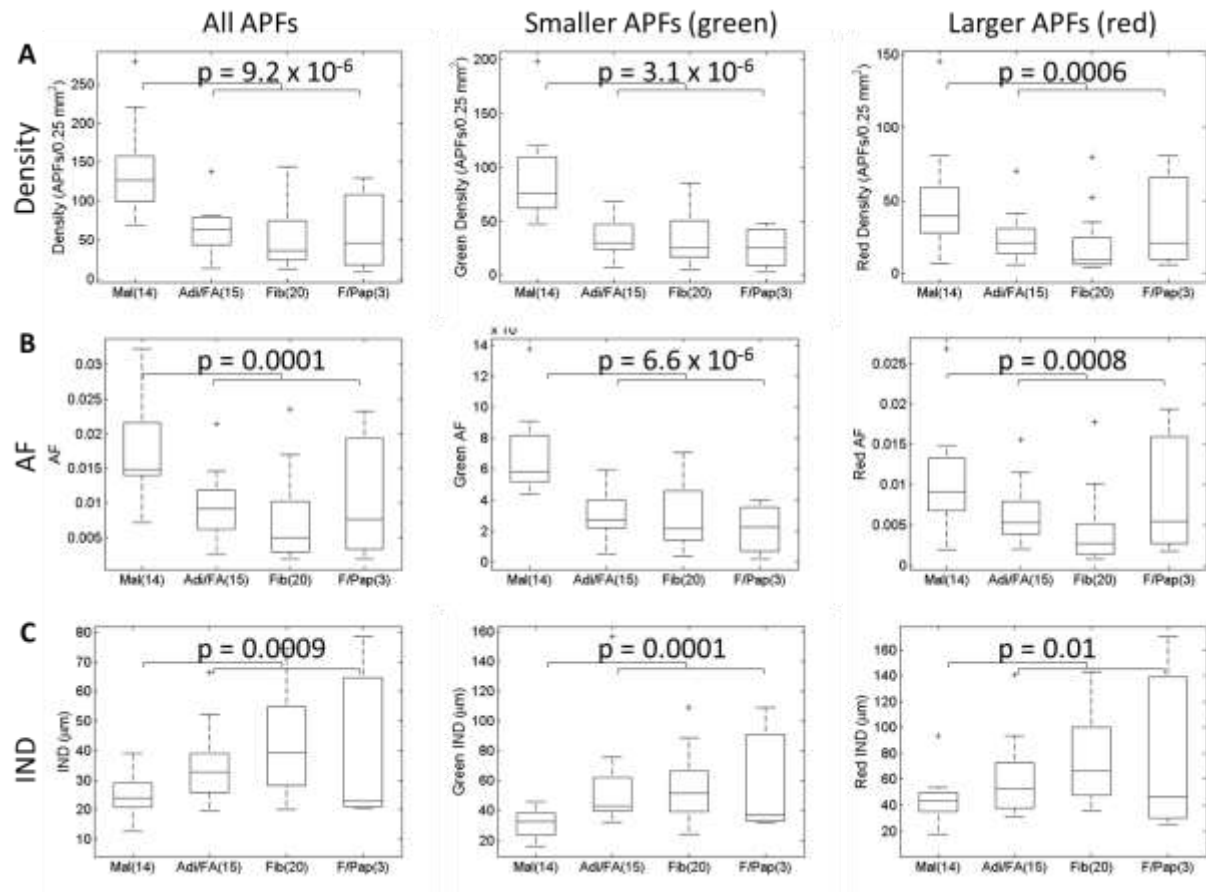

Figure 2.4. Variables calculated for the site level data set. Variables were calculated from 14 malignant (Mal), 18 adipose and fibroadipose (Adi/FA), 20 fibrous (Fib) images, and 3 fibroadipose and papilloma (F/Pap) images. Boxplots were created for the density, area fraction (AF), and average internuclear distance (IND), and are shown in A-C respectively. Calculations were completed for all APFs, smaller APFs (green), and larger APFs (red) and are shown in columns 1-3 respectively. P values calculated from Wilcoxon rank sums are shown in each boxplot. All p values less than 0.05 are considered significant.

ROC curves for the top two performing models are shown for both the original model and for cross-validation in Figure 2.5A and B. The model density (green) + AF (green) achieved the

highest AUC for both the original model (AUC = 0.95) and for the cross-validated model (Crossval AUC = 0.93). No additional improvement in performance was gained by using all three variables – density (green) + AF (green) + IND (green). The optimal cutpoint on the cross-validation density (green) + AF (green) curve in Figure 2.5A yielded a sensitivity of 86%, specificity of 89%, and overall accuracy of 88%. In total, there were 12 true positive (TP), 2 false negative (FN), 34 true negative (TN), and 4 false positive (FP) images. FP images included 1 adipose and 3 fibrous sites, while both FN images were IDC.
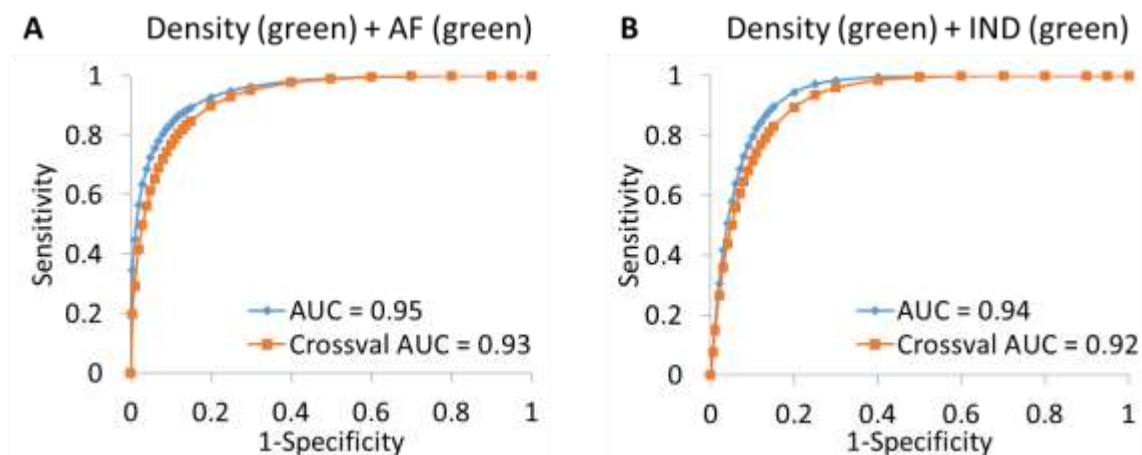

Figure 2.5. Multivariate models developed based on the site level data set. The top three performing variables from Figure 2.4 were used to create different multivariate models. ROC curves of the top two performing models are shown in A and B. Each ROC plot contains the ROC curve associated with the original model as well as with cross-validation. The area under the curve for the original model (AUC) and the AUC associated with cross-validation (Crossval AUC) are shown on each plot. The density, AF, and average IND of the smaller APFs (green) are referred to as Density (green), AF (green), and IND (green) respectively.

Biopsy level analysis: Table 2.3 shows how many images fell into each pathological category for the biopsy level analysis. For this analysis, the 2 biopsies from the other benign category were removed (which included a lymph node and hematoma) since only one sample was acquired of each of these rarer pathologies and no conclusions could be drawn. This decreased the total number of biopsies panels from 54 to 52.

Table 2.3. Biopsy level data set

Primary histology	Biopsies
# of biopsies	52
Malignant and premalignant	23 (44.2%)
Invasive ductal carcinoma (IDC)	20 (38.5%)
Invasive lobular carcinoma (ILC)	2 (3.8%)
Ductal carcinoma in situ (DCIS)	1 (1.9%)
Benign	29 (55.8%)
Adipose, fibroadipose	2 (3.8%)
Fibroglandular, fibrous, glandular	21 (40.4%)

Fibroadenoma, papilloma	6 (11.5%)

Figure 2.6 shows a representative example of a malignant and benign biopsy from our study. Each side of the biopsy was scanned length-wise—side 1 corresponds to the left column and side 2 corresponds to the right column. A summary diagnosis was given for the middle portion each biopsy (the central 8-18 mm), which we refer to as the biopsy level diagnosis. The malignant example in Figure 2.6A contains IDC and fibrous tissue and the benign example in Figure 2.6B contains fibroglandular and adipose tissue. The probability that each image is positive according to the density (green) + AF (green) model is listed in the upper left hand corner on each individual image. Probability values range from 0 to 1.
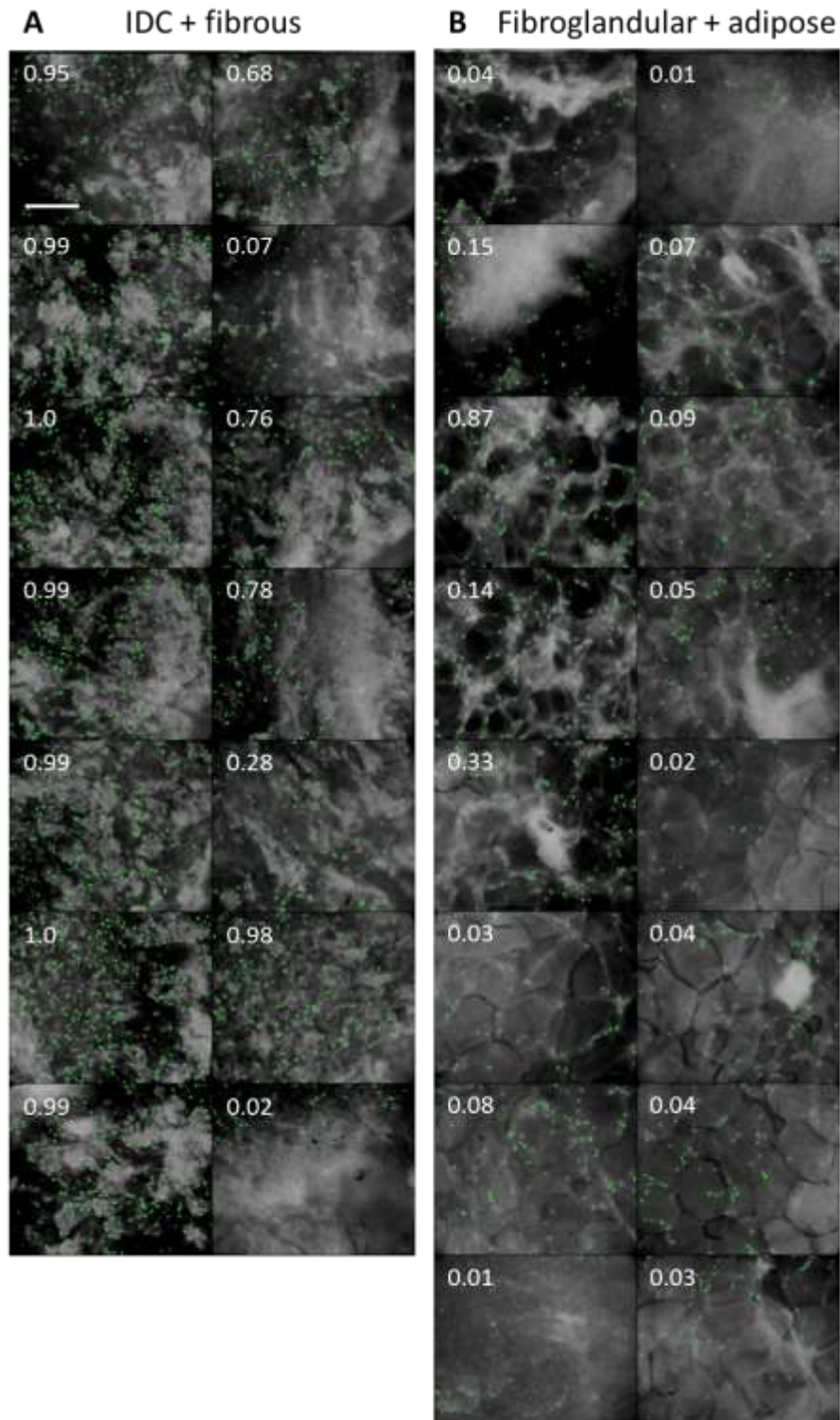
Figure 2.6. The application of an algorithm based on SCA+CT applied to representative biopsy panels. A representative positive and negative breast biopsy panel are shown in A and B respectively. Each side of the biopsy was scanned length-wise—side 1 corresponds to the left column and side 2 corresponds to the right column. Images are shown as an overlay in which the smaller acriflavine positive features (APFs) (<7 μm diameter) are false colored green. The

larger APFs were not included in the overlays because they are not part of the optimized model. The background was dimmed to enhance visualization in the overlay. The probability that each image is positive (according to the density (green) + AF (green) model) is listed in the upper left hand corner on each individual image. Scale bar is 200 µm.

As seen, each image in the representative biopsy panels in Figure 2.6 has a probability value of being malignant. In order to consolidate all of the probability values into a single variable, the number of images in each biopsy panel that had a probability of greater than or equal to chance (50%) was tabulated. For example, the biopsy in Figure 2.6A contains 14 probability values, 11 of which are greater than 0.50 (or 50%). The number of images for each biopsy panel (11 in previous example) was used to create ROC curves, which are shown in Figure 2.7. Specifically, the number of images was varied from 0 to 11 images (which was the highest value achieved for the 52 biopsies) to generate the ROC curves. As seen, the AUC associated with density (green) + AF (green) achieved the highest performance (AUC = 0.81). The optimal cut point on the ROC curve in Figure 2.7A yielded 17 TP, 6 FN, 24 TN, and 5 FP resulting in a sensitivity of 74%, a specificity of 83%, and overall accuracy of 79%. Of the 6 FN biopsies, 1 contained a small amount of DCIS, 4 contained IDC, and 1 contained ILC. Of the 5 FP biopsies, 3 fell into the fibrous category, 1 into the adipose/fibroadipose category, and 1 was a fibroadenoma. Two of the FP biopsies contained notable amounts of fibrosis or fibrous tissue, 1 contained inflammation dense inflammatory infiltrate, and 1 contained notable amounts of fat necrosis.
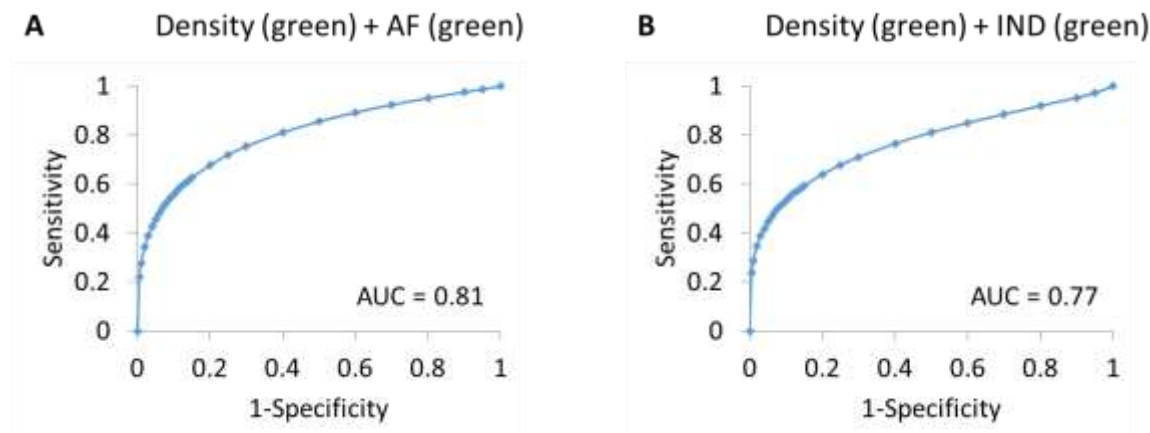

Figure 2.7. Models applied to biopsy level data set. The receiver operator curves (ROCs) for the top two performing models are shown in A and B. The area under the curve (AUC) is shown on each plot.

Discussion:
In this study, we demonstrate that fluorescent microscopic imaging of acriflavine stained tissue combined with an algorithm that leverages SCA+CT provides a rapid, non-destructive and automated strategy for quantitative pathology of heterogeneous, fresh, core needle biopsies. The primary source of contrast in this study was the density of the smaller APFs, AF of the smaller APFs, and average IND of the smaller APFs. Specifically, the density of smaller APFs

(green) + AF of the smaller APFs (green) achieved the highest AUCs on the site level testing set (AUC = 0.93). As expected there were higher density values and AF values for positive images and lower average IND values for positive images (Figure 2.3). This trend was also seen in our previous work in which the density of the smaller features led to more significant differences between positive and negative images of excised preclinical sarcomas [43]. The density of the smaller APFs likely provides more contrast between malignant and benign images because nucleic acids are highly concentrated within the nucleoli of malignant cells while they are more diffuse within benign cells. For example, the presence of prominent or multiple nucleoli is associated with a high nuclear grade, which has been shown to correlate with the aggressive potential of breast carcinomas. Thus, malignant regions or images are likely to contain a larger amount of the smaller APFs.

A significant strength of this approach is no additional tuning or optimization of SCA+CT is required when transitioning the application from preclinical sarcoma margin images to clinical core needle breast biopsies. Thus, this work demonstrates that this methodology can be easily applied to a variety of different organ sites where point of care quantitative pathology would be useful. For example, this rapid low-cost approach may be useful to provide rapid histologic assessment in regions where traditional pathology techniques are unavailable. Specifically, this approach could be used to evaluate the adequacy of core needle biopsies immediately after the tissue is acquired and provide a preliminary diagnosis at the point-of-care. Another strength of this study is that we were able to image the first core biopsy, which typically came from the center of the suspicious mass in the patient. Ultimately this allowed us to acquire a high yield of malignant images in our data set. Additionally, our study did not require removing additional tissue from the patient (as would be the case if our study required taking a separate research biopsy).

However, since we merely intercepted the tissue between the biopsy procedure and the pathology laboratory, the tissue that we imaged and inked had to be placed in formalin with the other biopsies (in order to follow standard biopsy pathology protocols). Often this resulted in fragmentation of the tissue, which prevented our research team from acquiring a three prong pathology diagnosis. For example, if the ends of a biopsy broke off in the vial with the other biopsies, then we did not acquire a diagnosis for the ends of the biopsy (rather we only acquired a diagnosis for the middle portion of the biopsy). Additionally, we found that it was difficult to acquire high quality images of the ends of the biopsies with our device because the tissue was extremely thin and difficult to get in focus. Consequently, we could not use many of the images at the end of the biopsies in our site level data set. To increase the yield of high quality site level images, future studies could employ alternative inking strategies. For example, the middle portion of the biopsy, which is most likely to contain malignant tissue, could be inked with a different color. This approach could increase the yield and quality of malignant images in the site level data set.

A similar distribution of FPs and FNs was seen in the site level and biopsy level data set. Specifically, the site level FPs contained 1 adipose image and 3 fibrous images. Similarly, the biopsy level FPs contained 1 adipose/fibroadipose biopsy, 3 fibrous biopsies, and 1

fibroadenoma biopsy. As seen, fibrous tissues are the largest source of FPs for both the site level and biopsy level data sets, likely because fibrous tissues can be highly cellular and difficult to distinguish from malignant tissue types. The addition of the fibroadenoma as a FP in the biopsy level data set is not surprising – fibroadenomas are characterized by cellular stroma, whose density is also difficult to distinguish from malignant tissue types. The site level FNs included 2 IDC images, and the biopsy level FNs contained 4 IDC, 1 DCIS, and 1 ILC biopsy. As seen, IDC was the largest source of FNs for both the site level and biopsy level data sets. Interestingly, the 4 IDC and 1 ILC biopsies that were misclassified were embedded in fibrous tissue, which resulted in hazy images and likely prevented detection of APFs. The DCIS biopsy only contained focal DCIS in 2 ducts while the remainder of the biopsy contained fibroadipose tissue; thus, small changes in density were likely missed by our model. Performance slightly decreased from the site level data set (sensitivity = 86%, specificity = 89%) to biopsy level data set (sensitivity = 74%, specificity = 83%). This decrease in performance is likely due to the heterogeneity that is present in the biopsy level data set. Specifically, the site level data set contains individual images that each have a circular field of view of approximately 750 μm in diameter. Therefore, individual images are likely to only contain a single tissue type. Conversely, biopsy panels (which are comprised of the central 8-18 mm of the biopsy) are more likely to contain different tissue types. While each biopsy panel was categorized as IDC, ILC etc based on their primary diagnosis, other tissue types are often present. Additionally, there may be differing amounts of IDC or ILC, which was not quantified in the pathological diagnosis. Thus, there is more heterogeneity present in the biopsy level data set, which led to a slight decrease in the performance of the model.

In previous work we found that SCA+CT performance varies with contrast between the APFs and background fluorescence [43]. One shortcoming from the work shown here is that the fluorescence microendoscope collects light from several cell layers, which contributes to significant background fluorescence [44]. This can lead to hazy images, which directly affects our ability to segment APFs in our images. The ability to segment APFs with SCA+CT could be improved through leveraging optical sectioning techniques, such as confocal microscopy or structured illumination microscopy (SIM). While confocal microscopy can achieve high spatial resolution (<1 μm), the need for beam scanning limits the volume of tissue that can be surveyed in a given amount of time and ultimately limits it translatability to the clinical practice. SIM has been shown to perform equivalently to confocal microscopy with respect to optical sectioning and SNR, particularly in superficial tissues [50-52]. However, SIM has the added advantage of full-field illumination and non-descanned detection, thus lowering the complexity compared to confocal scanning systems, and increasing the speed with which microscopy of large tissue areas can be performed. Thus, SIM in combination with appropriate segmentation algorithms could be leveraged to image large areas of tissue at high resolution and provide quantitative information in a clinically relevant time window.

Conclusions:
In conclusion, acriflavine staining and fluorescence microscopy combined with SCA+CT can be used to quantitatively diagnose breast disease. Together, this work yields an optimized set of tools that are capable of imaging tissue at high resolution with no tissue processing and that can

automatically segment and quantify those specimens. Ultimately, this platform provides a potentially useful adjunct to histopathological techniques by providing quality control at the point of care setting.

Plans for year 6:
During year 6, we plan to publish the diagnostic model described above, which yielded the optimal separation between positive and negative biopsies. Together, this work will yield an optimized set of tools that are capable of imaging thick tissue at high resolution with no tissue processing and that can automatically segment and quantify those specimens.

Part B – Rice University
While the analysis shown in Part A above shows an optimized approach to quantify positive and negative biopsies imaged with the HRME, we also wanted to explore how higher resolution microscopes, such as a fluorescent confocal microscope, could be used to visualize ductal morphology in addition to nuclear morphology. Towards this end, we partnered with Rice University to acquire confocal images of resected breast tissue and developed computerized algorithms to segment and quantify nuclear and ductal parameters to further enhance our ability to characterize breast architectural features.

Introduction:
In order to characterize quantitative criteria to classify breast architecture, several studies have described segmentation algorithms based on nuclear [53-57] and ductal [58-60] morphometry in images of fixed tissue stained with hematoxylin and eosin (H&E) staining. Additionally, some recent studies evaluated nuclear morphometric parameters using wide-field fluorescence microscopy [42] and micro-optical computed tomography [49] to acquire images of breast tissue. Specifically, wide field fluorescence microscopy combined with watershed segmentation to quantify nuclei found that area fraction could distinguish between tumor and normal regions in excised rat mammary tissue with 97% accuracy [42]. Micro-optical computed tomography and nuclear morphometry was used to compare variations between human breast cell lines and found that nuclear volumes increased from normal to metastatic breast cells and that nuclei of abnormal cells contained more nucleoli [49].

The idea of establishing quantitative criteria on fixed tissue can be taken one step further to be applied directly to intact specimens using other imaging modalities, which can obviate the need for extensive tissue processing. Several studies have already described the feasibility of imaging breast tissue with confocal microscopy in a clinical setting, [61-66]. Schiffhauer and colleagues showed that confocal reflectance microscopy could be used to image benign and malignant breast features and provide visual similarity to H&E micrographs [63]. Abeytunge and colleagues demonstrated that confocal fluorescence microscopy can be used to rapidly acquire images of fresh tissue specimens between 1-2.5 cm^2 in size [63]. Kortum and colleagues recently showed that confocal fluorescence microscopy yields images with sufficient detail to identify benign and malignant breast architecture in freshly-excised tissue [61]. In another recent study, Kortum et al. demonstrated that confocal fluorescence images can be used to estimate

percent tumor cellularity in core needle biopsy specimens and can indicate the adequacy of procured tissue for diagnosis and ancillary molecular and immunophnenotypic studies [62].

The goal of this work is to combine both quantitative image processing techniques with optical microscopy of intact breast tissue specimens for interpretation of breast tissue at the point of care. The benefits of this approach are minimal tissue processing, rapid diagnosis, and quantitative criteria that could potentially reduce the subjectivity with intra- and inter-observer variation in the evaluation of breast histology. In this study, we combine clinical confocal microscopy with a computerized image processing algorithm to quantify both nuclear and ductal morphology of breast tissue; we develop an algorithm using these parameters to classify breast tissue as benign or malignant. Although previous studies have described evaluation of breast architecture in histologic images [53-60], these studies only considered either nuclear or ductal parameters. We show that combining both yields improved diagnostic performance, particularly in the diagnosis of invasive ductal cancer (IDC) and ductal carcinoma *in situ* (DCIS). The APF and ductal parameters described in this study could potentially be used for objective categorization of breast lesions.

Methods

Breast Tissue Acquisition and Preparation: Fresh human breast tissue specimens were acquired through a protocol approved by The University of Texas MD Anderson Cancer Center and Rice University Institutional Review Boards. Fresh breast tissue was acquired from patients undergoing surgery to excise a clinically abnormal lesion. The procedure for tissue preparation has been described previously [61]. In brief, two tissue specimens - one grossly abnormal and one grossly normal in appearance were acquired from each patient for image acquisition and evaluation; each specimen measured approximately 15 x 15 mm^2 in size, with thickness varying from 2-7 mm. Within 30 minutes of surgical excision, breast tissue specimens were stained for one minute in a solution of 0.01% acriflavine in 1X phosphate buffed saline (PBS). Acriflavine is a nuclear contrast agent [67, 68], which has been used to stain breast tissue, oral mucosa, Barrett's esophagus, cervical tissue, and sarcoma in previous studies [43, 61, 62, 69-73]. Following topical application of acriflavine, specimens were washed with 1X PBS and then immediately imaged.

Image Acquisition and Evaluation: Confocal fluorescence images were acquired from multiple sites within each specimen using a multi-wavelength scanning confocal microscope (Vivascope 2500®, Caliber Imaging and Diagnostics) as described previously [61, 62, 74]. Following topical application of acriflavine and the PBS wash, each tissue specimen was positioned on the microscope stage and imaged using 2.1 ± 0.4 mW power at 488 nm laser excitation, and the fluorescence was detected in a band pass of 550 ± 44 nm with a 30x water immersion lens. At these settings, the lateral and axial resolution was 1.0 μm and 5.0 μm, respectively, in the center of the 750 x 750 μm^2 field of view. A 12 x 12 mm^2 composite image was created for both sides of each tissue specimen. To create the composite image, images were acquired from contiguous sites in a grid pattern (maximum area 12.2 x 12.2 mm^2) over the surface of the specimen at an approximate depth of 20 μm.. Following image acquisition, specimens were kept

moist in 1X PBS and were submitted for routine histologic preparation and fixation. Samples were stained with H&E and fixed on microscope slides for histologic assessment.

A board-certified, breast pathologist (author S. Krishnamurthy) viewed composite confocal images and fixed tissue specimens stained with H&E using a conventional light microscope to identify sites that corresponded to the same approximate location in the specimen based on similar image morphology. Specifically we selected in-focus confocal microscope fields of view that contain representative examples of characteristic benign and malignant breast features. Thus, at each site, a corresponding pair of confocal and H&E images were available from a 750 µm x 750 µm field of view. At each site, the H&E images of fixed tissue specimens were used as a reference standard to identify breast architectural features that should be present in corresponding confocal images [61, 75]. Benign breast features identified in reference H&E images included adipose and fibrous tissue, lobules, non-hyperplastic ducts, and ductal hyperplasia. Malignant breast features identified in reference H&E images included: ductal carcinoma *in situ* (DCIS), invasive ductal carcinoma (IDC), and invasive lobular carcinoma (ILC).

Segmentation and Connected Components Algorithms for Identifying APFs: Initial results from applying SCA+CT to confocal images (data not shown) indicate that SCA+CT may not be the optimal approach for segmenting APFs from confocal images. Therefore, an additional approach for image segmentation was investigated. Many approaches for nuclei or cell segmentation exist; however, nuclei segmentation remains a challenge due to the complexity of images that have varying levels of contrast and non-uniform background heterogeneity.

In 2004 Matas described a technique for detecting regions (i.e. APFs) in an image that remain stable over a range of threshold values called maximally stable extremal regions (MSER) [76]. The MSER method has important characteristics that are useful for the segmentation of objects (i.e. APFs) from complex (i.e. heterogeneous) images. In particular, MSER is not sensitive to pixel intensity changes and non-uniformities in background intensities because it is only dependent on pixel intensities within maximally stable extremal regions [77]. The feasibility for MSER for detecting cultured cells was recently demonstrated by Arteta et al [78]. Additionally, MSER has been used to detect cells in phase-contrast images [77].

In order to apply MSER to the confocal images of breast tissue, five tuning parameters associated with MSER were selected. The first two parameters, which included the minimum area (MinArea) and maximum area (MaxArea) of the connected components, are related to the expected size of APFs. These parameters were selected based on the biologically expected range of nuclear diameters. Specifically, other groups have found nuclear volume to range from approximately 200 to 1500 μm^3, which corresponds to 7 to 14 µm in diameter [49]. Therefore, MaxArea was set to 500 pixels, which corresponds to 19 µm in diameter, which is larger than the expected nuclear size for our images. MinArea was set to 35 pixels, which corresponds to 5 µm in diameter, which is smaller than the expected nuclear size for our images. The next set of parameters is related to the intensity thresholds and includes maximum variation (MaxVariation), minimum diversity (MinDiversity), and Delta. These intensity parameters were

systematically tuned through applying a range of values to representative images in order to select the best value for each parameter. Specifically, one input parameter was varied over a wide range while other input parameters were held constant. For each iteration, the area fraction (AF) from representative images of tumor and normal tissue was calculated and overlays of the features isolated with that particular setting were displayed. The values that led to the largest differences in AF between tumor and normal tissues, while isolating features that approximately corresponded to nuclei or nucleoli, which we refer to as acriflavine positive features (APFs), were selected. Specifically, MaxVariation was set equal to 2.5, MinDiversity to 0.5, and Delta to 6. These parameter values are in terms of relative intensity, which for our 8 bit images ranges from 0 to 255.

After APFs were isolated with MSER, a connected components algorithm was applied in order to calculate parameters such as the density and diameter of APFs. In the connected components algorithm, all touching or connected pixels are assumed to belong to the same APF. Parameters include APF density (the number of APFs in a unit area), area fraction (the total APF area divided by the total area), minimum inter-APF distance (the distance from an APF center to the next closest APF center), and APF diameter (the length of the major axis of each APF). APF density and area fraction (AF) represent scalar variables – only one value is returned for each image, while the minimum inter-APF distance (IND) and APF diameter represent vector variables – a value is calculated for each APF in the image. In order to consolidate the vector variables into a scalar value, several summary statistics were evaluated, including mean, median, mode, interquartile range, and standard deviation.

Ductal segmentation algorithm and quantification of ductal parameters: An algorithm was developed to measure ductal parameters, which segments non-hyperplastic ducts, ductal hyperplasia, and DCIS lesions based on the intensity of acriflavine staining. An illustration of both the APF and ductal segmentation is shown in Figure 2.8. To reduce noise and increase image contrast, a Wiener lowpass filter was first applied followed by contrast-limited adaptive histogram equalization (CLAHE). Images were converted from grayscale to binary using a user-defined threshold based on relative intensity. The mean threshold used to segment ducts was 107 ± 27 (range: 52-168) on a scale of 0 to 255 for 8 bit images. It was not possible to select a universal threshold, because in order to accurately segment ducts from surrounding tissue, it is necessary to isolate both nuclei in the duct walls and inter-nuclear space between them. The relative intensity of these features differed between images due to the variation in illumination power used for image acquisition and the variation in acriflavine staining. Areas smaller than the upper threshold for APFs (approximately equivalent to 280 μm^2 or 500 pixels, with a diameter of 19 μm [79]) were removed to avoid segmenting individual APFs outside of the duct walls. Individual ducts were manually segmented using a user-defined polygon selection tool to define architectural features corresponding to breast ducts. After application of the ductal segmentation algorithm, the binary confocal image showed the segmented duct walls and the outer and inner boundaries of the duct used to measure ductal parameters.
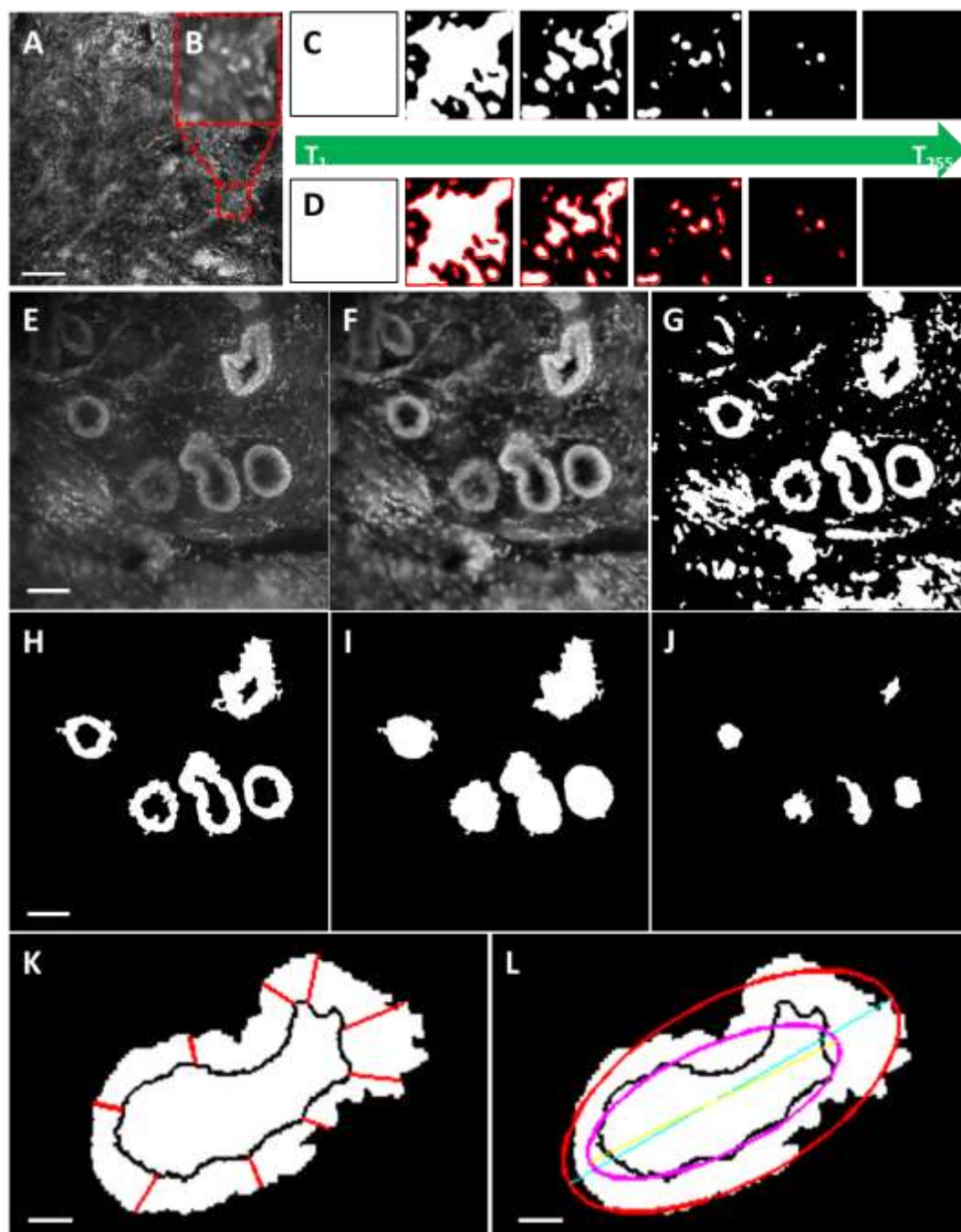
Figure 2.8. Algorithms for APF (A-D) and ductal (E-L) segmentation. APF segmentation: A: Raw image acquired from confocal fluorescence microscope with 750 x 750 μm² field of view. B: Region of interest selected in confocal fluorescence image with 75 x 75 μm² field of view. C: The maximally stable extremal regions (MSER) algorithm applies thresholds from 0 to 255 to B. D: At each threshold, the MSER algorithm identifies APFs as connected components and selects "maximally stable" components with the lowest size variation. Ductal segmentation: E: Raw image acquired from confocal fluorescence microscope with 750 x 750 μm² field of view. F: Wiener low pass filter and adaptive histogram equalization applied to E. G: The algorithm converts E to a binary image using an interactive threshold tool. H: Objects below range of APF

area are removed and then user selects a region of interest (ROI) around ducts with an interactive polygon selection tool. I: The algorithm fills boundaries of ducts identified in H to segment the outer boundaries of the duct. J: The algorithm selects the complement of H to segment the inner boundaries of the duct (lumen). K: Duct wall width is measured by selecting the shortest distance from the outer to the inner duct boundaries (red lines). L: Ellipses are fitted to outer and inner duct boundaries. E-J: scale bar is 100 µm. K,L: scale bar is 25 µm.

Following segmentation of ducts, a number of ductal parameters were measured based on the properties of the inner and outer duct boundaries. The outer boundary defines the outer edge of the duct wall and the inner boundary defines the inner edge of the duct wall; the lumen. The width of the duct wall was measured at every pixel on the outer edge of the duct wall. This was done by finding the shortest distance between every point on the outer boundary and the nearest point on the inner boundary. Duct wall width was measured for each non-hyperplastic duct, ductal hyperplasia, and DCIS lesion and the vector of values were summarized by calculating the mean, median, mode, interquartile range, and standard deviation. Other scalar parameters measured include the area of the duct wall, area of the lumen, area of an ellipse approximating the duct wall, area of an ellipse approximating the lumen, lengths of the major and minor axes for the duct and the lumen, solidity of the duct and the lumen, and eccentricity of the duct and the lumen.

Statistical analysis and model building: APF parameters were calculated for all sites (n = 259) and ductal parameters were calculated for all sites that contained ducts (n=50), and the diagnostic performance of each image parameter was individually assessed by determining the classification accuracy. Two-class linear discriminant analysis was performed to classify malignant from benign breast architectural features based on each individual APF or ductal parameter; receiver operator characteristic (ROC) curves were constructed and area under the curve (AUC) was calculated for each ROC curve. Sensitivity and specificity values were determined at the optimal cutpoint. Parameters were sorted by accuracy for classification of neoplasia based on AUC values. Boxplots were created for the parameters with the highest AUCs. A Student t-test for samples with unequal variances was used to identify statistically significant differences between mean parameter values measured in benign and malignant tissues. This analysis was performed to evaluate individual APF and ductal parameters to incorporate into a classification model.

Next we sought to develop a multivariate model to yield optimal separation between benign and malignant tissues. Towards that end, all 33 APF and ductal variables were used as input for a classification and regression tree (CART) function in Matlab. Decision trees were constructed using the automated Matlab function classregtree, which selects parameters and cutpoints that lead to the optimal classification of benign and malignant breast architectural features. Decision trees were pruned to prevent a single APF or ductal from being used at more than one node within the tree. Pruning was also performed to prevent the number of categories for classification of malignant breast features from exceeding 3: the number of malignant tissue types (IDC, ILC, and DCIS). After construction, decision tree nodes were pruned by finding the next higher node whose decision point led to two categories, one with a majority of neoplastic

sites, and one with a majority of benign sites. A custom leave one out cross-validation algorithm was also developed in order to calculate the cross-validated sensitivity and specificity. Specifically, 258 of the 259 data points were used to build a CART model, which contained the same two variables at the first and second decision points. Specifically the standard deviation of IND (StdIND) was the first decision point and the number of lumens was the second decision point. However, with each iteration of leave one out cross-validation, the cutoff value of StdIND could vary. The cutoff value associated with the number of lumens (number of lumens >1) was held constant because biologically normal ducts are expected to only contain a single lumen; therefore, this was considered to be the optimal and only logical cutoff value and therefore was held constant. Then the model was applied to the remaining data point, which was classified as either benign or malignant. This process was repeated for all 259 data points, and the calculated diagnosis for each image was compared to the known diagnosis in order to calculate sensitivity and specificity for the cross-validated model. The performance of the decision tree was characterized by computing sensitivity and specificity for classification of malignant breast architectural features. Additionally, sensitivity and specificity were calculated for each individual histologic type of malignant tissue in order to determine the relative classification accuracy for IDC, ILC, and DCIS sites. For example, in order to calculate sensitivity for IDC, true positives were defined as IDC sites that had been classifed as malignant by the decision tree, and false negatives were defined as IDC sites that had been classified as benign. Specificity was calculated by defining true negatives as benign sites that were correctly classified in the decision tree and false positives were defined as benign sites that were incorrectly classified. An ROC curve was constructed for the decision tree model. All sites were sorted in order of ascending StdIND value and then sensitivity and specificity for classification of neoplasia were calculated at every StdIND value. The cutoff value for number of lumens was held constant at 1 lumen because biologically normal ducts are expected to only contain a single lumen. AUC was calculated based on the resulting ROC curve.

Results:

A total of 259 sites from 36 patients were identified in composite confocal fluorescence images. A summary of patients, sites, and diagnoses are included in Table 2.4. In total there were 179 benign sites, which included adipose tissue, fibrous tissue, lobules, and benign ducts, and 80 malignant sites, which included DCIS, IDC, and ILC.

Table 2.4 Summary of patients from which tissue specimens were acquired, sites analyzed, and histologic diagnoses

Diagnosis	Patients	Sites
Benign		
Adipose tissue	18	42
Fibrous tissue	16	31
Lobules	12	82
Non-hyperplastic ducts	9	20
Hyperplastic ducts	4	4
Malignant		
Ductal carcinoma in situ (DCIS)	6	26

Invasive ductal carcinoma (IDC)	15	37
Invasive lobular carcinoma (ILC)	3	17
Total	36	259

Figure 2.9 shows representative confocal images of sites without ducts acquired by confocal fluorescence microscopy in row 1 and APFs isolated with MSER at those sites in row 2. Row 3 shows sites in the corresponding histologic slide with H&E staining that have similar histology to the confocal sites. APFs were false-colored green and overlaid onto the original images for visualization. As seen, APFs are isolated at the periphery of adipose cells and are dispersed throughout the fibrous tissue image. Denser clusters of APFs are isolated in and around lobules. APFs are the densest at sites with malignant tissue, including IDC and ILC.
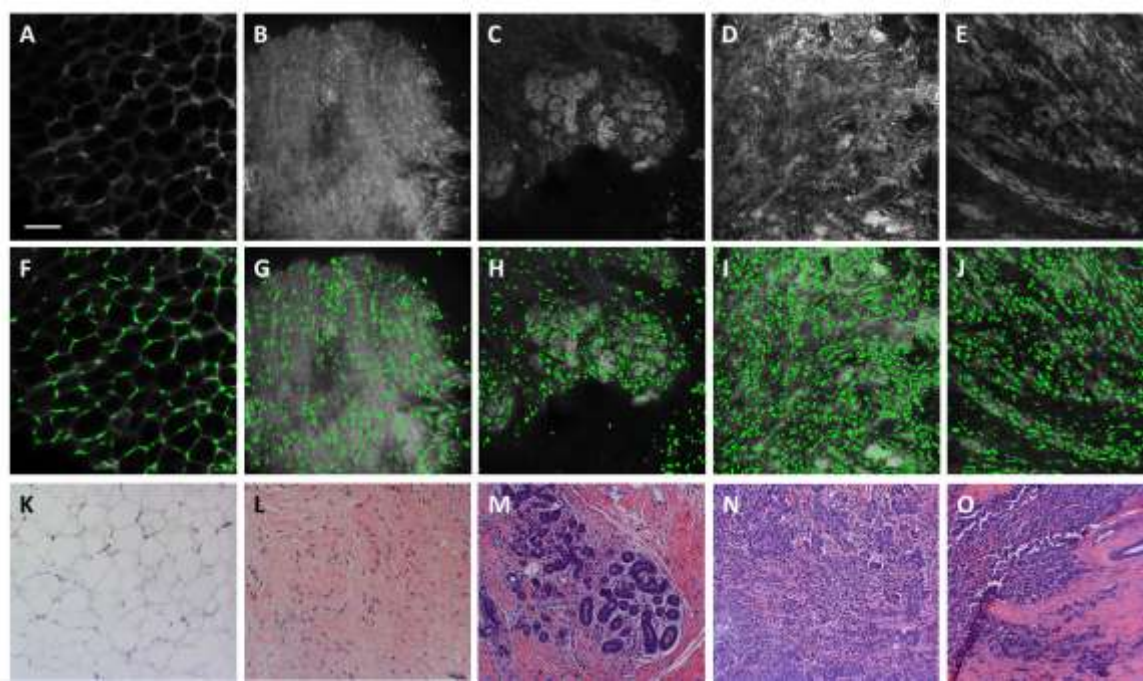

Figure 2.9. Representative raw confocal fluorescence images of adipose tissue, fibrous tissue, lobules, invasive ductal carcinoma, and invasive lobular carcinoma are shown in A through E, respectively. F-J: APFs segmented by identifying maximally stable extremal regions (MSER) are false colored green and overlaid onto the raw confocal fluorescence image. K-O: Histologic slides with H&E staining show similar histology to confocal images in A-E. Slides were prepared with the same specimens from which confocal images were acquired. Scale bar is 100 μm.

Figure 2.10 shows representative images of breast ducts acquired with confocal fluorescence microscopy in row 1, APFs that were isolated at sites with breast ducts using MSER in row 2, and ducts that were segmented with the ductal segmentation algorithm in row 3. Row 4 of Figure 2.10 shows sites in the corresponding histologic slide with H&E staining that have similar histology to the confocal sites. APF density in and around the ducts increases from the non-hyperplastic duct, to the hyperplastic duct, to DCIS. However, relatively few APFs are successfully isolated using MSER within the non-hyperplastic and hyperplastic ducts, which is

most likely due to the fact that the borders of individual APFs are difficult to visually discern in confocal fluorescence images. The images of sites isolated with the ductal segmentation algorithm show well-defined lumens in both the non-hyperplastic duct and hyperplastic duct. Conversely, the image of DCIS shows bridges of cells crossing the lumen to create a cribriform pattern with several lumens.
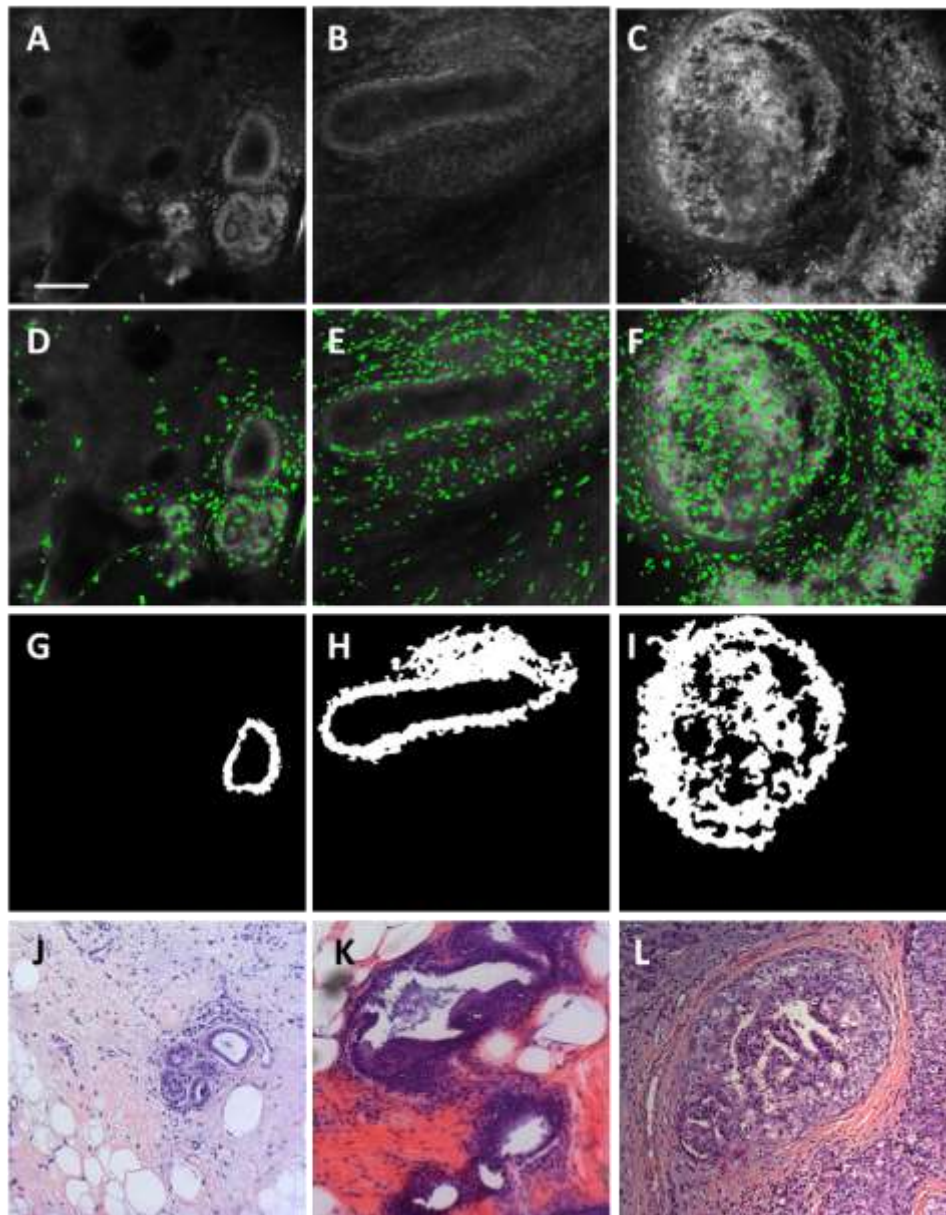

Figure 2.10. Representative confocal images of normal, non-hyperplastic ducts (A), hyperplastic ducts (B), and ductal carcinoma *in situ* (C) analyzed with the APF segmentation algorithm (middle row) and with the ductal segmentation algorithm (bottom row). D-F: APFs segmented by identifying maximally stable extremal regions (MSER) are false colored green and overlaid onto the raw confocal fluorescence image. G-I: Breast ducts segmented using the ductal segmentation algorithm. J-L: Histologic slides with H&E staining show similar histology to

confocal images in A-E. Slides were prepared with the same specimens from which confocal images were acquired. Scale bar is 100 μm.

The parameters that yielded the highest performance for distinguishing between benign and malignant sites are shown in Table 2.5. We evaluated the performance of APF parameters for classification of benign and malignant features in all sites and in sub-groups of sites that did or did not contain ducts to determine the groups for which APF parameters had the highest classification accuracy. We only evaluated the classification accuracy of ductal parameters at sites that contained ducts. APF parameters measured at non-duct sites achieve higher performance (AUC = 0.93) than APF parameters measured at duct sites (AUC = 0.69). Conversely, ductal parameters achieve higher performance (AUC = 0.92) than APF parameters for classification of duct sites (AUC = 0.69). These findings suggest that a combination of APF parameters measured at non-duct sites and ductal parameters measured at duct sites may yield improved separation between all benign and malignant sites.

Table 2.5 Summary of top performing parameters for distinguishing between benign and malignant sites measured using algorithms

Group	Performance metric	Standard deviation of IND	Area fraction	Range of IND
A. Classification by APF Parameter – All Sites	AUC	0.87	0.86	0.87
	Sensitivity	78	76	76
	Specificity	82	79	85
B. Classification by APF Parameter – Non-duct Sites	AUC	0.93	0.92	0.91
	Sensitivity	85	80	81
	Specificity	88	87	88
C. Classification by APF Parameter – Duct Sites	AUC	0.68	0.72	0.74
	Sensitivity	46	65	62
	Specificity	100	70	96
Group	Performance metric	Number of lumens	Minor dimension of outer ellipse	Area of outer ellipse
D. Classification by Duct Parameter – Duct Sites	AUC	0.92	0.83	0.82
	Sensitivity	88	73	81
	Specificity	88	79	75

Boxplots showing the mean and interquartile range of the top three performing APF parameters are shown in Figure 2.11. Both Std IND and Range IND decrease from adipose to fibrous to lobules to ILC to IDC, while AF increases from adipose to fibrous to lobules to ILC to IDC. This trend suggests that the number of clusters of APFs increases from adipose tissue, which has the fewest, to IDC, which has the greatest number of clusters of APFs. All comparisons between benign (adipose, fibrous, lobules) and malignant (IDC, ILC) sites were significant. Similarly, AF increases from adipose to fibrous to lobules to IDC, which suggests increasing APF density.

Boxplots showing the mean and interquartile range of the top three performing ductal parameters for duct sites are also shown in Figure 2.11. DCIS lesions have a significantly higher number of lumens than hyperplastic and non-hyperplastic ducts (p < 0.001), which is consistent with the cribriform pattern that occurs when abnormally high cellular proliferation causes the luminal space to be filled with epithelial cells. The minor dimension of the outer ellipse approximating the duct is significantly smaller in normal, non-hyperplastic ducts than in DCIS lesions (p < 0.001). There is no significant difference in the minor dimension between ellipses approximating hyperplastic ducts and DCIS lesions. The area of the outer ellipse approximating duct area was significantly smaller in normal, non-hyperplastic ducts than in DCIS lesions (p < 0.001). There is no significant difference between the average area of outer ellipses approximating hyperplastic ducts and DCIS lesions.
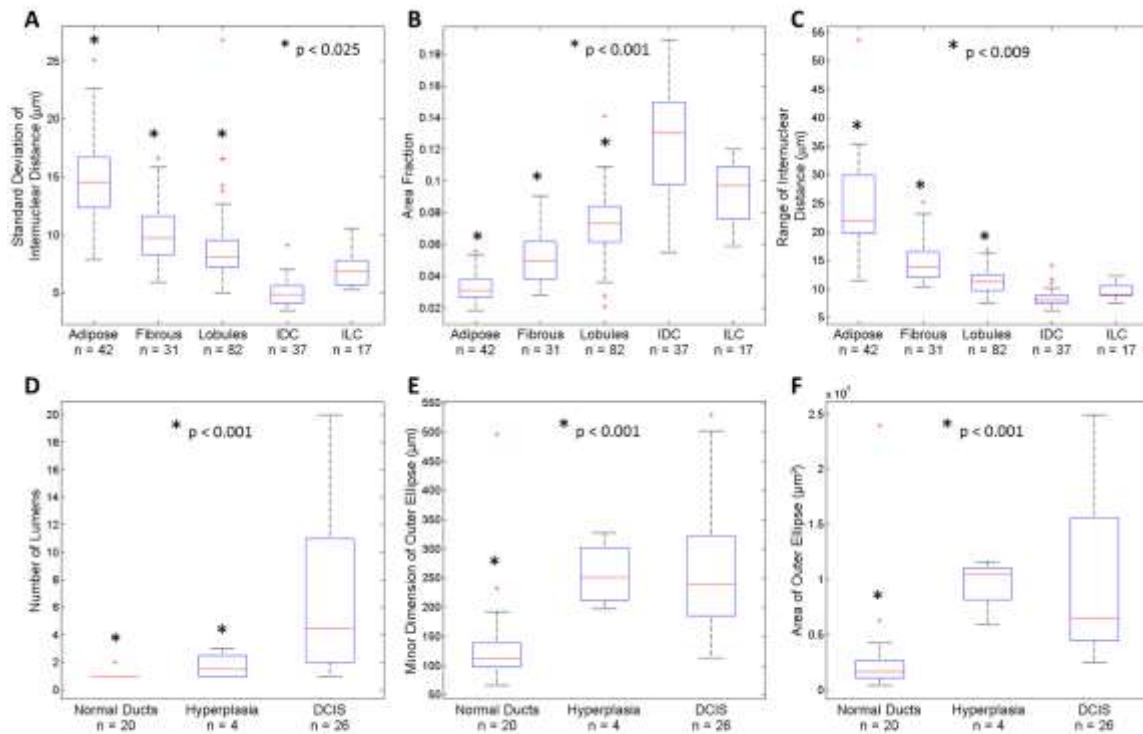

Figure 2.11. Mean value of parameters used to separate malignant from benign sites. APF parameters calculated with the APF segmentation algorithm are shown for all adipose, fibrous, lobules, invasive ductal carcinoma (IDC), and invasive lobular carcinoma (ILC) sites; A: standard deviation of IND; B: area fraction; C: range of IND. Ductal parameters calculated with the duct-based segmentation algorithm are shown for all normal, non-hyperplastic ducts, hyperplastic ducts (Hyperplasia), and ductal carcinoma in situ (DCIS); D: number of lumens; E: minor dimension of outer ellipse; F: area of outer ellipse. The number of sites represented in each box is represented by n. Significant differences between mean values of parameters measured at benign and malignant sites are indicated by asterisks (*).

All 33 APF and ductal parameters were used as input for a classification and regression tree (CART) algorithm to automate selection of parameters to discriminate benign and malignant

sites. The CART algorithm was pruned to remove redundancies and over-fitting to the data set. The classification tree generated through this process is shown in Figure 2.11. Std IND with a cutoff value of 6.83 µm is the first decision point selected for classification by the decision tree, followed by number of lumens with a cutoff value of 1. Std IND < 6.83 µm separates out 52 true positives composed of IDC, DCIS, and ILC sties and 9 false positives composed of fibrous and lobule sites. The remaining sites enter the second node – Number of lumens > 1– which separates out 13 true positive DCIS sites and 3 false positive hyperplasia and normal duct sites. The remaining sites are classified as benign and are composed of 167 true negative adipose, fibrous, lobule, normal duct, and hyperplasia sites and 15 false positive IDC, DCIS, and ILC sites. Overall, the model achieved a sensitivity and specificity of 81% and 93% respectively, corresponding to an area under the curve of 0.93 and 90% overall classification accuracy, as shown in Table 2.6. If the model is evaluated based on classification of individual histologic types of neoplasia, 92% of IDC sites and 96% of DCIS sites were classified correctly. However, the model correctly classified only 35% of ILC sites. Additionally, leave one out cross-validation was performed, which yielded a cross-validated sensitivity of 75% and specificity of 93%. Specifically, cross-validation resulted in a 6% drop in sensitivity (from 81% to 75%) due to the fact that 5 additional IDC images were incorrectly classified during cross-validation. When each of these 5 cases were left out of the original cohort of data used to form the model (in other words during the leave one out cross-validation exercise), the cutoff value associated with StdIND dropped. This resulted in each of the 5 cases being classified as a false negative. For the remainder of the images, the cutoff value associated with StdIND remained the same, resulting in the same specificity of 93%.
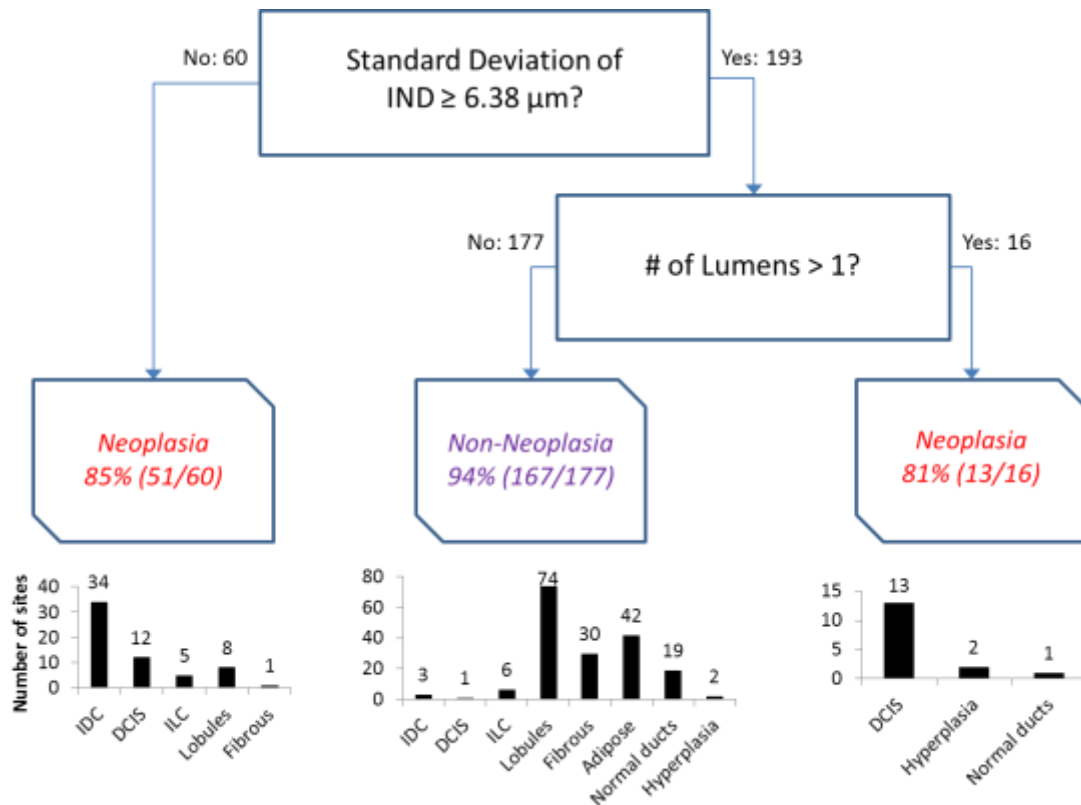
Figure 2.11. Classification tree automatically generated when all APF and duct data was used. Duct- and APF-based parameters selected by classification regression tree analysis to optimize separation between benign and malignant sites. Bar graphs show the diagnoses of sites sorted into each classification category.

Table 2.6. Performance of model for classification of neoplasia, non-neoplasia, and individual histologic types of breast neoplasia

	Sensitivity	Specificity
Classification Tree Model	81% (65/80)	93% (167/179)
Cross-validated Model	75% (60/80)	93% (167/179)
	Correctly Classified	
All Sites	90% (232/259)	
DCIS	96% (25/26)	
IDC	92% (34/37)	
ILC	35% (6/17)	

As seen in the histograms in Figure 2.11 ILC sites account for the largest number of false negative (n = 11 out of 17 sites) while lobule sites account for the largest number of false positives (n = 8 out of 82 sites). Figure 2.12 shows representative confocal images of a true positive ILC, false negative ILC, true negative lobules, and false positive lobules sites in row 1 and APFs isolated with MSER at those sites in row 2. Row 3 shows sites in the corresponding histologic slide with H&E staining that have similar histology to the confocal sites. As seen, there are large differences in the density and clustering of APFs between the true positive ILC site

and true negative lobules site. In comparison, the false negative ILC site in has relatively few APFs, which appear to be predominately clustered in the upper left region of the image. Conversely, the false positive lobules site contains more APFs than Figure 2.12G, particularly in stromal tissue located in between lobules.
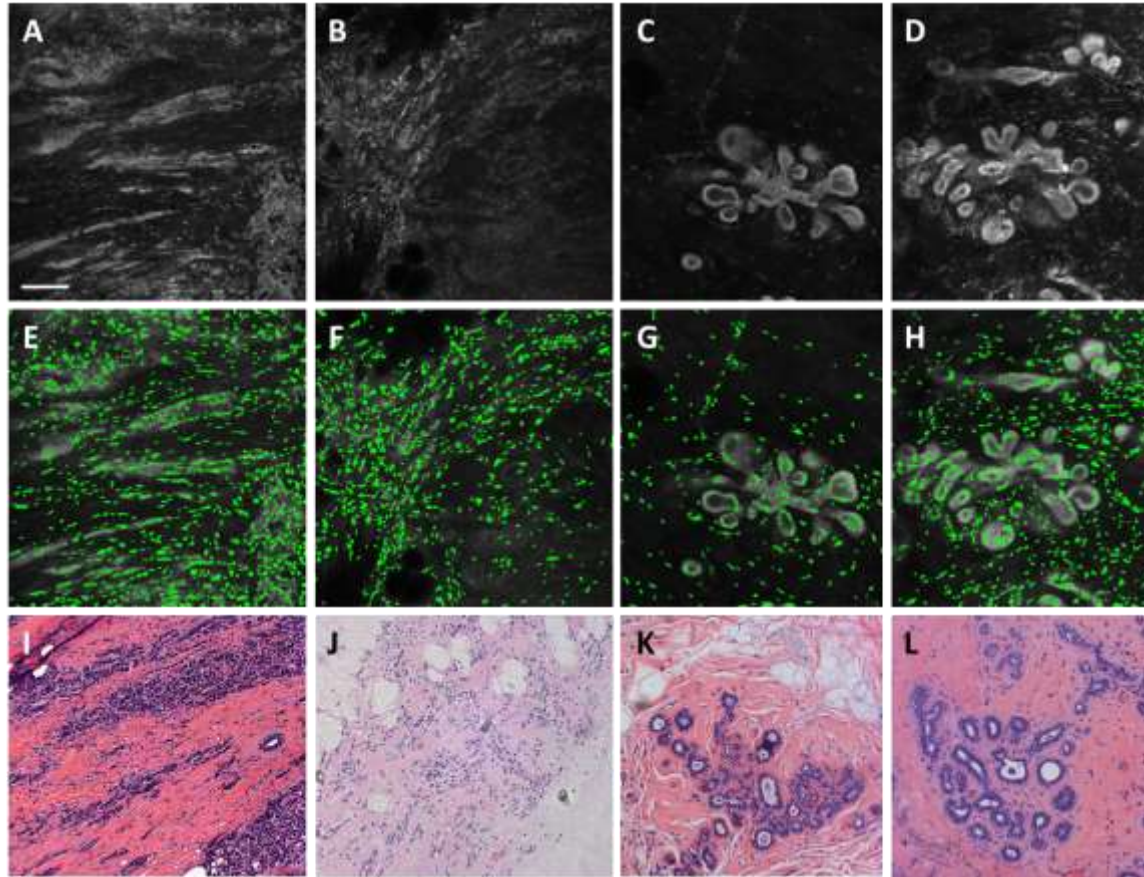

Figure 2.12. Representative images of sites with lowest classification accuracy in the decision tree model. A-D: invasive lobular carcinoma and lobules in confocal fluorescence images. E-H: APFs segmented by identifying maximally stable extremal regions (MSER) are false colored green and overlaid onto the raw confocal fluorescence image. I-L: Histologic slides with H&E staining show similar histology to confocal images in A-E. Slides were prepared with the same specimens from which confocal images were acquired. A, E: a true positive invasive lobular carcinoma (ILC) site; B, F: false negative ILC site; C, G: true negative lobules; and D, H: false positive lobules. Scale bar is 100 µm.

Discussion

In this study, we performed quantitative analysis of breast histology in confocal fluorescence images by designing algorithms to segment and measure APF and ductal parameters. We combined APF and ductal parameters to develop a classification tree model to classify malignant from benign changes in the breast parenchyma with 81% sensitivity and 93% specificity, which corresponded to an AUC of 0.93 and an overall accuracy of 90%. The cross-

validated model classified the same sites with 75% sensitivity, 93% specificity, and 88% overall accuracy.

Several groups have used automated morphometric evaluation of nuclei in H&E stained sections of breast tissue [53-56], cytological smears of breast tissue [57], and fluorescence microscopy images of mouse tissue [42, 43] to classify benign and malignant breast features. While these groups demonstrate that quantitative nuclear parameters can be used to classify benign and malignant breast features, some lesions are more difficult to distinguish. For example, Rajesh et al used automated nuclear morphometry to classify ILC, IDC, and borderline lesions [55]. While significant differences were found between parameters measured for ILC and IDC, no significant difference was found between parameters measured for ILC and benign borderline lesions [55]. We found similar results to the other studies – namely that ILC is difficult to distinguish from non-neoplasia based on APF features alone. Additionally, several studies have demonstrated the feasibility of computerized image analysis to distinguish between non-hyperplastic ducts, hyperplastic ducts, and DCIS. Mayr et al used computerized image analysis to quantify ductal parameters in H&E-stained slides of breast biopsies and found that the most significant parameters for differentiation between normal ducts and DCIS were duct mean diameter and the presence of necrosis [58]. Anderson et al used a computerized segmentation algorithm to measure parameters of ductal hyperplasia and DCIS in tissue sections stained with the antibody cocktail AE 1/3, and showed that the highest classification accuracy for DCIS was achieved by combining parameters of ducts and lumina [59]. The findings from our work agree with previous studies, which showed that quantitative ductal parameters can be used to classify benign and malignant ducts [58, 59].

The strengths of our study are that we demonstrate that APF and ductal parameters can be measured in confocal fluorescence images of clinical samples acquired at the point of care. We perform quantitative analysis of breast tissue architecture without requiring tissue fixation, cutting, and staining and achieve comparable classification accuracy to studies that performed computerized analysis on fixed breast tissue stained with H&E. The model classified IDC and DCIS with greater than 90% accuracy using parameters that were based on the morphological characteristics of each malignant tissue type. Specifically, IDC was classified with 92% accuracy using standard deviation of IND as a parameter, which identifies dense clusters of APFs. DCIS was classified with 96% accuracy based on the presence of more than one lumen, which is consistent with the cribriform pattern. Overall we achieve high performance (AUC = 0.93) on a large number of sites (n = 259).

There are several limitations associated with this study. While our initial data set contains a large number of sites (n = 259), the data was acquired at a single center (The University of Texas M.D. Anderson Cancer Center), and some individual categories, such as ILC contain relatively few sites (n = 17); therefore, additional work is needed with a large, independent data set composed of data from more than one center to validate the feasibility and reproducibility of these parameters. However, our initial results indicate that leave one out cross-validation of the CART model yields similar performance to the original model suggesting that our model may generalize to an independent data set. Another limitation to the study are the large variances

observed for the APF parameters that reflect the high degree of heterogeneity in APF size and spacing in benign and malignant breast epithelia. Changes in APF area and spacing in breast epithelia occur frequently in both ductal and lobular nuclei and can be due to a number of clinical features, including sexual maturity, pregnancy, menopausal status, use of hormonal contraceptives, and presence of mammary carcinoma [80]. The presence of heterogeneity in APF area and distribution within benign breast tissue is a potential source of variance for the nuclear parameters measured in this study. Similarly, IDC and ILC typically contain irregular nuclear sizes and an irregular distribution of nuclei [81, 82], which is another potential source of variance within APF parameters. In addition, the algorithm designed for ductal segmentation uses an interactive threshold to convert images from grayscale to binary and a user-defined selection tool to isolate ducts from surrounding nuclei. The ductal segmentation process is a potential source of variability between users, particularly for parameters that could be impacted by a user's visual assessment of the duct wall boundaries, such as duct wall width. However, the ductal parameter that was ultimately selected for the decision tree model was the number of lumens, which is unlikely to vary at the decision point (number of lumens greater than 1) based on slight variations to the threshold value or by excluding surrounding nuclei. This is because it is readily apparent if a duct has one or more lumens based on visual assessment, however the segmentation algorithm could assist in identifying ducts with more than 1 lumen. Lastly, examination of the breakdown of false negatives and false positives reveals that our algorithm does most poorly at distinguishing ILC and lobule sites. Specifically 65% (n = 11 out of 17 sites) of ILC sites and 10% of lobule sites (n = 8 out of 82 sites) are incorrectly classified. Figure 2.12 reveals that there are differences in quantity and clustering of APFs between the true positive and false negative ILC sites. In particular, APFs in the false negative ILC site appear to be predominately located in the upper left region of the image, suggesting that only the upper left region of the image contains ILC while the remainder of the image may contain other benign tissue. Therefore, the fraction of the image that consists of a malignant tissue type may correlate with the likelihood that it is correctly classified as a true positive site. Conversely, the false positive lobules site contains more APFs than the true negative lobule site, particularly in stromal tissue located in between lobules. This indicates that the stromal tissue that lobules or other features are embedded within may lead to incorrect classification as a false positive site. In future work, additional parameters are needed in order to classify lobules as benign and ILC as malignant with greater accuracy.

It is to be noted that while confocal microscopy provides high resolution high quality images, currently its cost, footprint, and maintenance requirements limit the ability to translate this imaging platform to routine usage in patient care. Specifically, the need for beam scanning in confocal microscopy limits the volume of tissue that can be surveyed in a given amount of time. However, structured illumination microscopy (SIM) has the added advantage of full-field illumination and non-descanned detection, which lowers the complexity and cost and increases the speed with which microscopy of large tissue areas can be performed. Thus, in future work the algorithms described here could be combined with SIM imaging of breast tissue to enable automated diagnosis of large tissue areas.

Conclusion

In conclusion, quantitative APF and ductal parameters were measured in confocal fluorescence images of fresh breast tissue and used to develop a classification algorithm that distinguishes between 259 benign and malignant sites with an accuracy of 88%. The APF and ductal parameters described in this study could be used to develop criteria to automate breast lesion diagnosis for immediate evaluation of fresh tissue at the point of care obviating the need for extensive tissue preparation.

Plans for year 6

Quantitative diagnostic criteria developed on fluorescence confocal images could be applied to SIM images of breast tissue in the future in order to enable automated assessment of breast tumor margins.

Aim 3: *Optical quantitative biology to assess therapy response in different sub-types of breast cancer:*

Introduction

Until this year, our progress toward Aim 3 focused on the development of an optical imaging strategy for simultaneously monitoring glucose uptake and oxygenation *in vivo.* The primary goal of developing such a technique is to identify aerobic glycolysis in tumors- a common metabolic phenotype that manifests itself in aggressive, therapy-resistant tumors. In the past year, we have published the results presented in our last report detailing the final optimization of our hyperspectral imaging technique for measurement of delivery-corrected glucose uptake and vascular oxygenation (Frees, *PLOS ONE* 2014). Additionally, we have published on a similar technique to monitor glucose and oxygenation endpoints with optical spectroscopy (Rajaram, *PLOS ONE* 2015). We are confident that both our imaging and spectroscopy methods can be used to quantify glucose and vascular oxygen saturation for the identification of tumors undergoing aerobic glycolysis. The techniques are complementary, since hyperspectral imaging provides spatial information that can inform on tumor heterogeneity and spectroscopy is ideal for monitoring the metabolism of solid tumors during long-term tumor growth and therapy studies.

While aerobic glycolysis is often considered the primary metabolic program of aggressive tumors, recent studies show that many tumors use a combination of glycolysis and mitochondrial metabolism to better supply the tumor's energy needs [83]. Mitochondria play crucial roles in maintaining sufficient ATP levels and in regulating apoptosis to promote proliferation [84]. Mitochondrial membrane potential, maintained by electron transport, is the primary driver for mitochondria functionality [84], and hyperpolarized mitochondria have been observed in a wide range of cancers [85]. It follows that increased mitochondrial membrane potential provides natural contrast for identification of cancers. Therapies are now being developed that target mitochondrial metabolism and cause changes in mitochondrial membrane potential. A decrease in membrane potential may indicate successful treatment of a tumor, as a loss of membrane potential is closely related to the beginning of the apoptotic cascade toward cell death [86].

Additionally, recent literature has shown that the aggressiveness of a cancer depends on its ability to maintain "metabolic plasticity" [83], that is, to quickly adapt to microenvironmental stress. Metastatic cells were shown to adapt to stress differently than non-metastatic cells; in

particular, they were able to rapidly change their metabolic programming based on substrate availability [83]. Taken together, the literature indicates that measuring a combination of endpoints that reports on glucose uptake, oxygenation, and mitochondrial metabolism may be more effective for distinguishing particularly aggressive tumors. Further, subjecting tumors to stress and observing their metabolic plasticity may give additional insight into their eventual fate, e.g. helping to predict therapy response or resistance.

Despite its recognized importance, few methods exist to measure mitochondrial membrane potential *in vivo*. A family of cyanine dye-based compounds has been shown to successful monitor expected changes in mitochondrial membrane potential [85], but the compounds are still being developed and are not commercially available. Their fluorescence excitation and emission fall in the NIR-wavelength range, which offers good depth penetration but cannot be imaged on many microscopes. Another class of lipophilic, cationic dyes based on the fluorescent compound rhodamine are well-validated to report on mitochondrial membrane potential [87]. One such dye is TMRE. TMRE's primary use is in cell culture, but a handful of research groups have used them *in vivo* for visualization of mitochondria [88]. However, these few studies did not thoroughly characterize the uptake kinetics of the dye, and also required topical application of TMRE, making the technique very limiting.

Based on its low cost, commercial availability, and extensive characterization in cell studies, we identified TMRE as a good candidate for monitoring mitochondrial membrane potential *in vivo*. Here we present our optimization of TMRE to measure relative mitochondrial metabolism *in vivo* in a non-tumor window chamber model. We also demonstrate for the first time that TMRE can be used *in vivo* to identify aberrant cancer metabolism.

Following the optimization of TMRE as a marker of mitochondrial membrane potential, we incorporate our new mitochondrial probe with previously optimized glucose uptake and oxygenation endpoints [89, 90] to create an "optical energy budget". We show here our preliminary results exploring the relationship between optical energy budget and metastatic potential. Further, we stress the non-metastatic and metastatic tumor lines with hypoxia to observe the changes in optical energy budget; our hypothesis is that metastatic tumors maintain "metabolic plasticity" and respond to stress differently than non-metastatic tumors.

In summary, a majority of our focus during the previous year can be divided into two major components: 1. Optimization of TMRE for *in vivo* measurement of mitochondrial membrane potential, and 2. Development of a hypoxia "stress test" to relate metabolic stress response to metastatic potential. This works propels us toward our long-term goal of determining whether the oxygenation-metabolic demand relationship changes in a tumor in response to stress and whether this response or change can be indicative of long-term tumor behavior.

Methods
vitro cell culture
4T1, 4T07, and 67NR murine mammary adenocarcinoma lines were cultured in Dulbecco's Modified Eagle Medium (DMEM) supplemented with 10% fetal bovine serum (FBS) and 1% antibiotics. For the TMRE confocal imaging experiment, the cells were trypsinized and seeded on 60mm tissue culture plates 24 hours before imaging according to established protocols. Cells were incubated with 50nM TMRE for 30 minutes prior to the start of imaging.

Dorsal skin flap window chamber model
All *in vivo* experiments were conducted according to a protocol approved by Duke University

Institutional Animal Care and Use Committee. We surgically implanted titanium window chambers on the back of female athymic nude mice (nu/nu, NCI, Frederic, Maryland) under anesthesia (i.p. administration of ketamine (100 mg/kg) and xylazine (10 mg/kg)). We injected a 20 μL suspension (20,000 cells) of 4T1, 4T07, or 67NR cells into the dorsal skin fold and placed a glass coverslip (dia = 12 mm, No. 2, Erie Scientific, Portsmouth, New Hampshire) over the exposed tissue. In a separate group of control mice, we injected 20 μL of saline. All animals were housed in an on-site housing facility with *ad libitum* access to food and water and standard 12-hour light/dark cycles. A flowchart depicting the experiment protocol is presented in Figure 3.1. For a 6-hour period prior to imaging, the animals were only provided with water. During normoxia measurements, the animals were allowed to breathe 21% oxygen. For the hypoxia group, the animals were subjected to breathing 10% oxygen for 15 minutes prior to imaging and through the end of imaging. For the CCCP group animals, the window chamber glass was removed and 0.1 mL of 50μM CCCP (carbonyl cyanide *m*-chlorophenylhydrazone) was topically applied to the tissue. The glass was immediately replaced, and imaging began 5 minutes later.

Hyperspectral imaging of oxygen saturation, glucose uptake, and mitochondrial membrane potential
A schematic of our study design is shown in Figure 3.1. We used a Zeiss Axioskop 2 microscope for recording all images. At the end of 6 hours of fasting, we initially recorded trans-illumination images and corresponding background fluorescence images. In addition, a free space trans-illumination image using appropriate neutral density filters was recorded before every imaging session to account for daily variations in light intensity. The animals were administered a 100 μL tail-vein injection of TMRE (25mM; MW: 515) or NBDG (6mM; MW: 342.16) dissolved in sterile saline. We recorded the TMRE or NBDG fluorescence for 75 minutes as follows: every 5 seconds for the first 8 minutes, every 30 seconds for the next 30 minutes and every 3 minutes for the final 35 minutes of imaging.
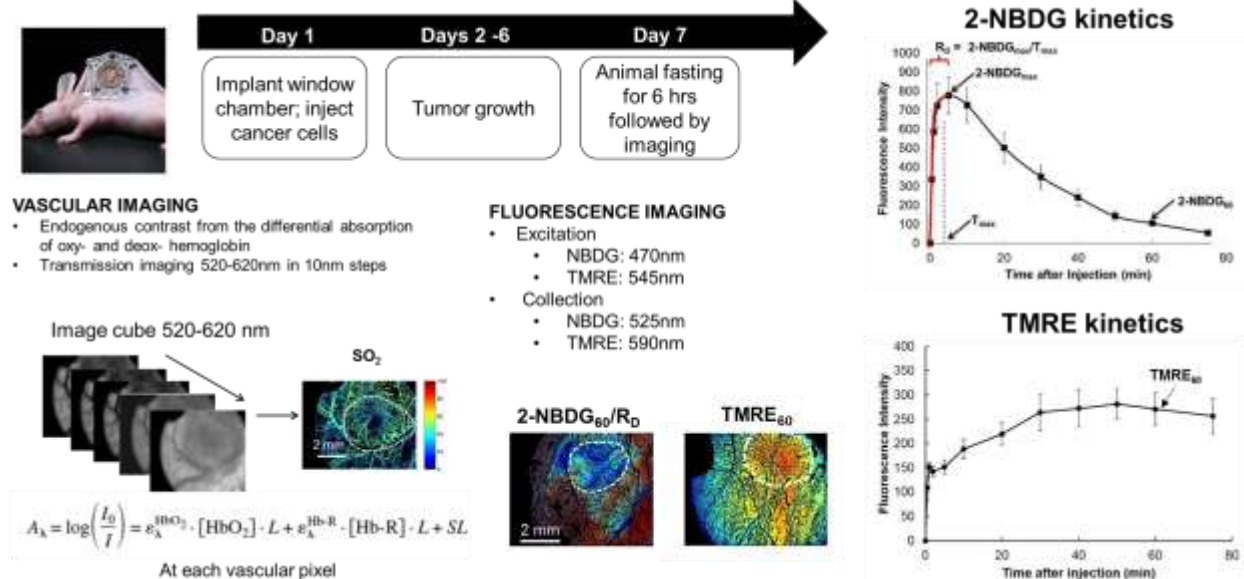

Figure 3.1 Imaging of 2-NBDG and TMRE in a dorsal window chamber model. The timeline of imaging events and description of hyperspectral imaging settings are shown. Trans-illumination images were collected in 10 nm increments from 500–600 nm and used to calculate hemoglobin saturation, as shown in the SO_2 image. Typical mages for the endpoints 2-NBDG$_{60}$/R$_D$ (delivery corrected 2-NBDG uptake) and TMRE$_{60}$ (TMRE uptake) are also shown. A 6 mM injection of 2-NBDG or 25uM injection of TMRE was given and imaged for 75 minutes, and the mean of the tissue region for each image was used to construct the kinetic curves at right. Adapted from

Frees, et al [71].

Calculation of Vascular and Metabolic Parameters
Trans-illumination images were collected in 10 nm increments from 500–600 nm and used to create an image cube (x,y,λ). A modified form of the Beer-Lambert law that describes absorption of chromophores in thin slices is fit to the trans-illumination image cube (x,y,λ) to obtain the concentration of the primary absorbers – oxy $[HbO_2]$ and deoxy-hemoglobin $[dHb]$ at each pixel [91]. We then calculate total hemoglobin content, $[THb]$ ($[HbO_2]+[dHb]$), and SO_2 ($[HbO_2]/[THb]$) at each pixel. The presence or absence of $[THb]$ was used to segment the images into vascular and tissue space, respectively.

After 2-NBDG or TMRE injection, fluorescence images were collected) for a period of 75 minutes. A kinetic uptake curve was created from the (x,y,t) data for each (x,y) pixel location. As shown in Figure 3.1, for 2-NBDG the initial rate of delivery (R_D) and glucose uptake $(2\text{-}NBDG_{60})$ were calculated from the time course for each pixel. R_D was calculated from the rise to the initial peak of the curve as $(I_{max}\text{-}I_0)/T_{max}$, where subscript 0 corresponds to a baseline image captured prior to 2-NBDG injection. $2\text{-}NBDG_{60}$ is defined as glucose uptake. For TMRE, we found that signal was stable from 40-75 minutes after injection. We chose to compare TMRE uptake at 60 minutes $(TMRE_{60})$ across groups. This timepoint was chosen for future simultaneous measurement of TMRE and 2-NBDG.

TMRE endpoints were additionally parsed by SO_2. For each $TMRE_{60}$ image, every tissue pixel in the tumor area was assigned to an SO_2 group according to the SO_2 of the nearest vascular pixel. In a given image, there were as many as five SO_2 groups: 0–10% SO_2, 10–20% SO_2, 20–40% SO_2, 40–60% SO_2, and 60–80% SO_2. The distribution of pixels for each endpoint was then represented as a survival curve (1-cumulative distribution) stratified by SO_2. Curves were then averaged within a tissue type (Non-tumor, 67NR, 4T07 or 4T1). Each curve then represents the mean of distributions of $TMRE_{60}$ pixels at a given SO_2 level from up to 6 mice. Curves were plotted in two ways: to compare $TMRE_{60}$ across SO_2 levels within a given tissue type, and to compare $TMRE_{60}$ across tissue types at a given SO_2 level.

Statistical Analysis
For all *in vitro* and *in vivo* studies containing multiple groups, a one-way analysis of variance (ANOVA) was performed to test for global differences and a Tukey-Kramer post-hoc test was used to compare between groups. For all analyses, differences between groups were deemed significant at a 95% confidence level ($p \leq 0.05$). Error bars correspond to standard error on all graphs. The Statistics Toolbox in MATLAB (MathWorks, USA) was used for all statistical tests.

Results

Part 1: Optimization of TMRE for in vivo measurement of mitochondrial membrane potential

In Figure 3.2, we investigated whether localization of TMRE delivered *in vivo* via tail vein injection was comparable to TMRE localization in cell culture exposed directly to TMRE in solution. Indeed, we saw that in all tumor cell lines and in a non-tumor window chamber, TMRE localized to mitochondrial-sized features surrounding cell nuclei stained with Hoescht nuclear contrast agent. This confirmed to us that TMRE localization *in vivo* 30 minutes after tail vein injection was comparable to TMRE localization *in vitro* after 30 minutes of incubation with TMRE solution.
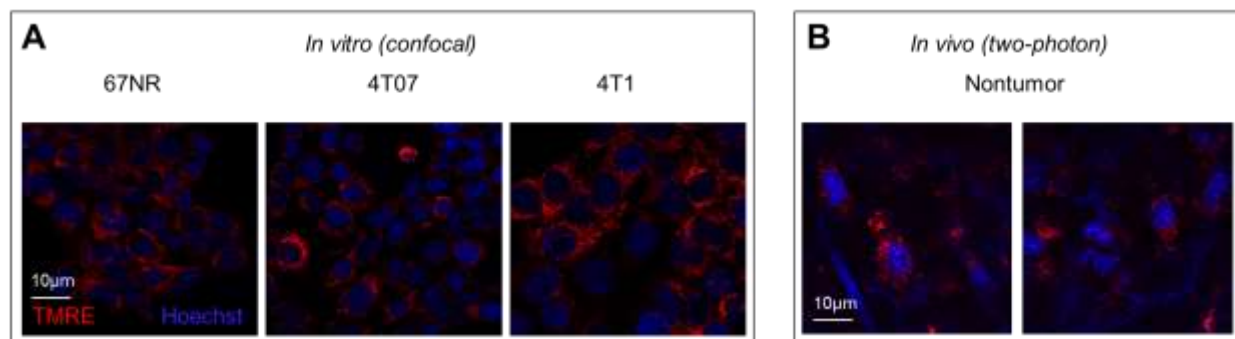
Figure 3.2 High resolution imaging shows consistent localization of TMRE *in vitro* and *in vivo*. Panel 3.1A shows *in vitro* uptake of 50nM TMRE in a panel of murine breast cancer cell lines. The cells were incubated with TMRE for 30 minutes prior to imaging. Hoescht nuclear stain was added to cells 10 minutes prior to imaging. Panel 3.2B shows *in vivo* uptake of TMRE in a non-tumor window chamber, 30 minutes after tail vein injection of 0.1mL of 25µM TMRE. Hoescht was injected subcutaneously in the window chamber 15 minutes prior to TMRE injection. In both *in vitro* and *in vivo* imaging, TMRE localizes to mitochondrial-sized features surrounding cell nuclei.

Figure 3.3 shows an investigation of TMRE uptake kinetics in non-tumor tissue during control conditions (Normoxia, 21% O_2) and during environmental perturbations (Hypoxia and CCCP). Hypoxia has been shown to cause a decrease in mitochondrial membrane potential in cells *in vitro*, likely due to a decrease in oxidative phosphorylation and electron transport during low-oxygen conditions. CCCP, a protonophore, has been shown to decrease mitochondrial membrane potential in both cell and animal models. As expected, both hypoxia and CCCP caused a drastic decrease in TMRE uptake, signaling that our measurements indeed correlate with expected changes in mitochondrial membrane potential. Interestingly, when each curve was normalized to its respective peak, the uptake kinetics for each group were indistinguishable. This indicates that only the magnitude of TMRE uptake, and not the observed kinetics, report on mitochondrial membrane potential. The small variance in kinetics across mice, as well as the stability of the TMRE signal from 40-75 minutes, allows for robust measurements for a wide range of experiments. For our studies, we used the timepoint t=60. This timepoint was chosen for eventual integration of TMRE with our previously optimized measurements of glucose (2-NBDG) uptake.
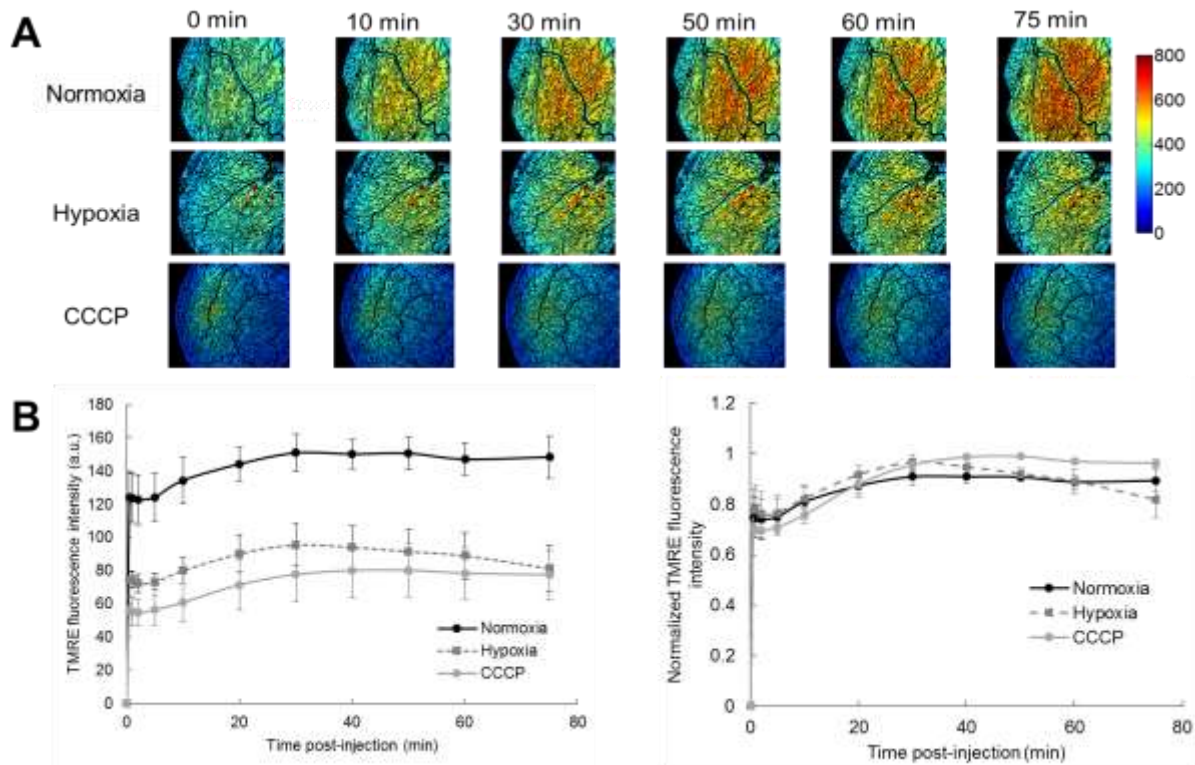
Figure 3.3. TMRE uptake kinetics are repeatable and robust to measure response to perturbations. Representative images of TMRE uptake in non-tumor window chambers following injection with 0.1mL of 100uM TMRE are shown in Panel 3.3A. The normoxia window chamber was imaged under baseline imaging conditions (21% O_2). The hypoxia window chamber was imaged while breathing 10% O_2. The mouse breathed hypoxic gas 15 minutes prior to TMRE injection. In the CCCP window chamber, 0.1mL of 50µM CCCP was administered topically 5 minutes prior to TMRE injection. Figure 3.3B shows the effect of environmental perturbations on TMRE uptake kinetics. Both hypoxia and CCCP decreased TMRE uptake at all timepoints. However, as shown in Figure 3.3C, normalized kinetics are indistinguishable between groups. Additionally, TMRE signal is incredibly stable following initial uptake; the average loss of signal is less than 5% from t = 40 minutes to t= 75 minutes (Mean ΔTMRE = -0.045, ± 0.03 (SE)). The timepoint 60 minutes was chosen for our studies.

In Figure 3.4, the relationship between TMRE uptake ($TMRE_{60}$) and vascular oxygenation (SO_2) is explored for non-tumor window chambers under control conditions (normoxia), hypoxic conditions, or CCCP pre-treatment. $TMRE_{60}$ and SO_2 were quantified for each mouse. As expected, perturbation of the tissue microenvironment with hypoxia or CCCP was sufficient to decrease $TMRE_{60}$. The decrease in $TMRE_{60}$ was likely caused by diverting substrates away from oxidative phosphorylation and thus causing a decrease in mmp (hypoxia group) or by directly collapsing mmp by transport of protons through the membrane (CCCP group). Surprisingly, the overall mean SO_2 was not decreased during hypoxia compared to the normoxia group; however, SO_2 in each of the mice decreased from its own baseline after hypoxia (p<0.05 by paired t-test). CCCP caused a slight but not significant increase in SO_2, likely due to decreased oxygen consumption.

During control conditions, TMRE uptake is consistent regardless of SO_2, reflecting the tightly controlled metabolic state of normal tissue. However, when energy supply and demand is

perturbed with hypoxia, TMRE uptake increases with SO_2, revealing a relationship between increased oxygen consumption and TMRE uptake. In the CCCP group, TMRE uptake was comparable, but low, at all SO_2. Figure 3.4D shows that, regardless of regional SO_2, TMRE uptake was decreased in both the hypoxia and CCCP groups relative to control. It follows that TMRE uptake, and by extension, mitochondrial membrane potential, are sensitive primarily to the disruption of baseline conditions of the microenvironment, and not to natural variations in oxygen consumption.
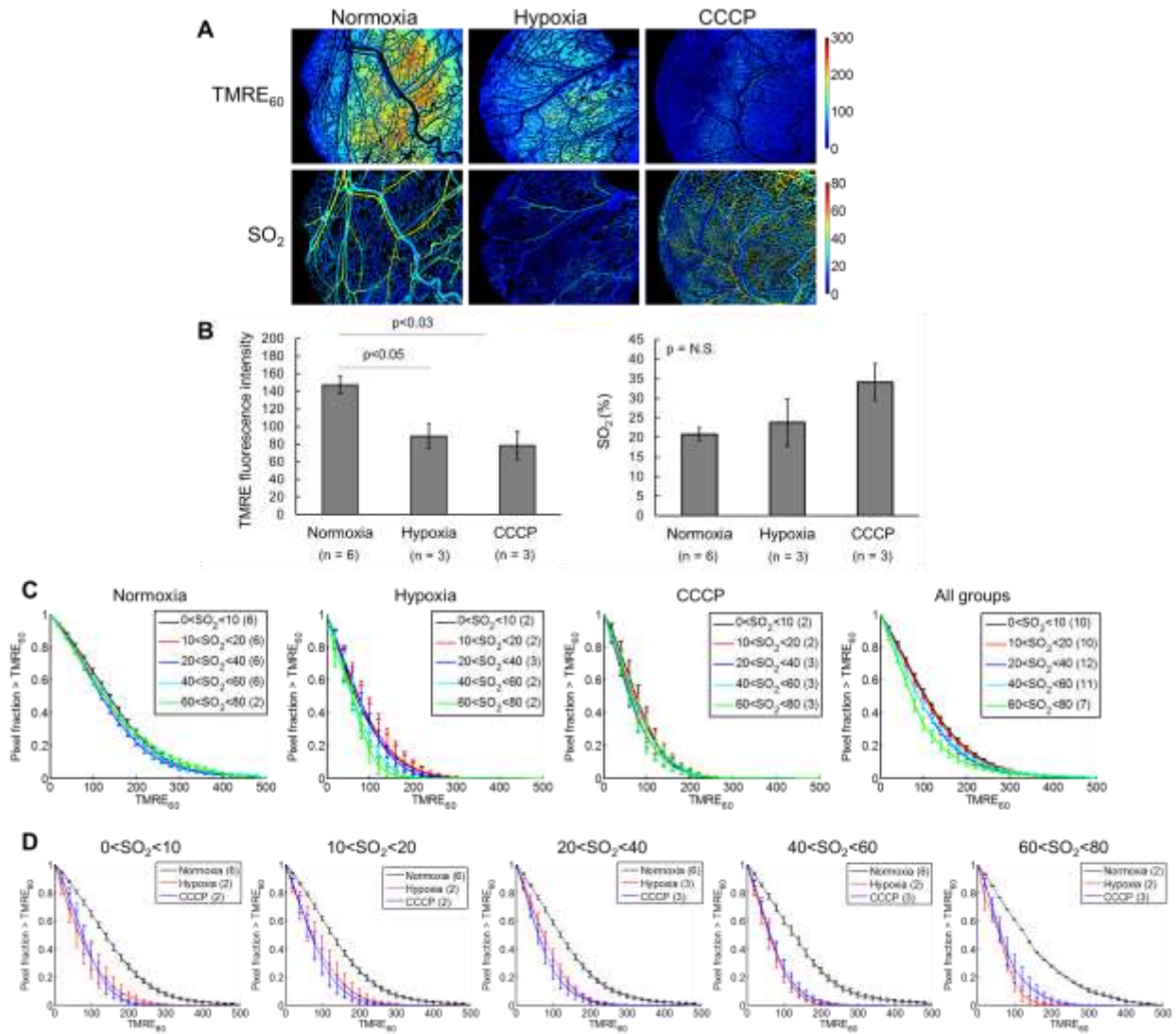

Figure 3.4 TMRE uptake is sensitive to changes in the tissue microenvironment. Panel 3.4A shows TMRE uptake and SO_2 in non-tumor window chambers subjected to 1. normoxia (15 minutes of breathing room air before TMRE injection), 2. hypoxia (15 minutes of breathing 10% O_2 before TMRE injection), or 3. Pre-treatment with the mitochondrial uncoupler CCCP (0.1mL of 50µM CCCP) topically applied to tissue 5 minutes before TMRE injection). Each mouse was administered 0.1mL of 25uM TMRE via tail vein. Panel 3.4B shows group averages of $TMRE_{60}$ and SO_2 in each treatment group. Though there was no significant difference in mean SO_2, TMRE uptake decreased in hypoxia ($p<0.05$) and CCCP ($p<0.03$) groups**.** Panel 3.4C shows the relationship between regional TMRE uptake and regional SO_2 in each group.

Each curve corresponds to a distribution of tissue pixels parsed by the SO_2 in the nearest vessel. In normoxia and CCCP groups, TMRE uptake is comparable across all SO_2. During hypoxia, TMRE uptake increases in low-SO_2 regions. Panel 3.4D shows the comparison of TMRE uptake across groups for each SO_2 level. TMRE uptake in the normoxia-breathing group is greater than uptake in hypoxia or CCCP groups, regardless of SO_2. This indicates metabolic changes in the tissue that cannot be sensed by SO_2 alone. n = 6 mice (normoxia) and n = 3 mice (hypoxia and CCCP), unless otherwise noted in legend.

Figure 3.5 summarizes the TMRE uptake characteristics of non-tumor tissue, non-metastatic tumors (67NR and 4T07), and metastatic tumors (4T1), and the relationship between SO_2 and $TMRE_{60}$ in each group. The boxplots in Figure 3.5B show that TMRE uptake is increased in all tumor types relative to non-tumor, but SO_2 is comparable in all groups. $TMRE_{60}$ is not distinguishable between tumors lines. Interestingly, Figure 3.5C shows that a relationship may exist between SO_2 and TMRE in non-metastatic 67NR and 4T07, but not in normal tissue or metastatic 4T1. TMRE uptake increases slightly as SO_2 decreases in 67NR and 4T07, indicating the ability of these tumors to maintain higher mmp in regions of greater oxygen consumption. When all groups are compared at a given SO_2 in Figure 3.5D, $TMRE_{60}$ is consistently increased in tumor relative to normal, with a slight trend $TMRE_{60,67NR} > TMRE_{60,4T07} > TMRE_{60,4T1}$ at all SO_2. *In vitro* imaging, shown in Figure 3.5E, reveals that TMRE uptake is comparable among the tumor lines, corroborating *in vivo* results.
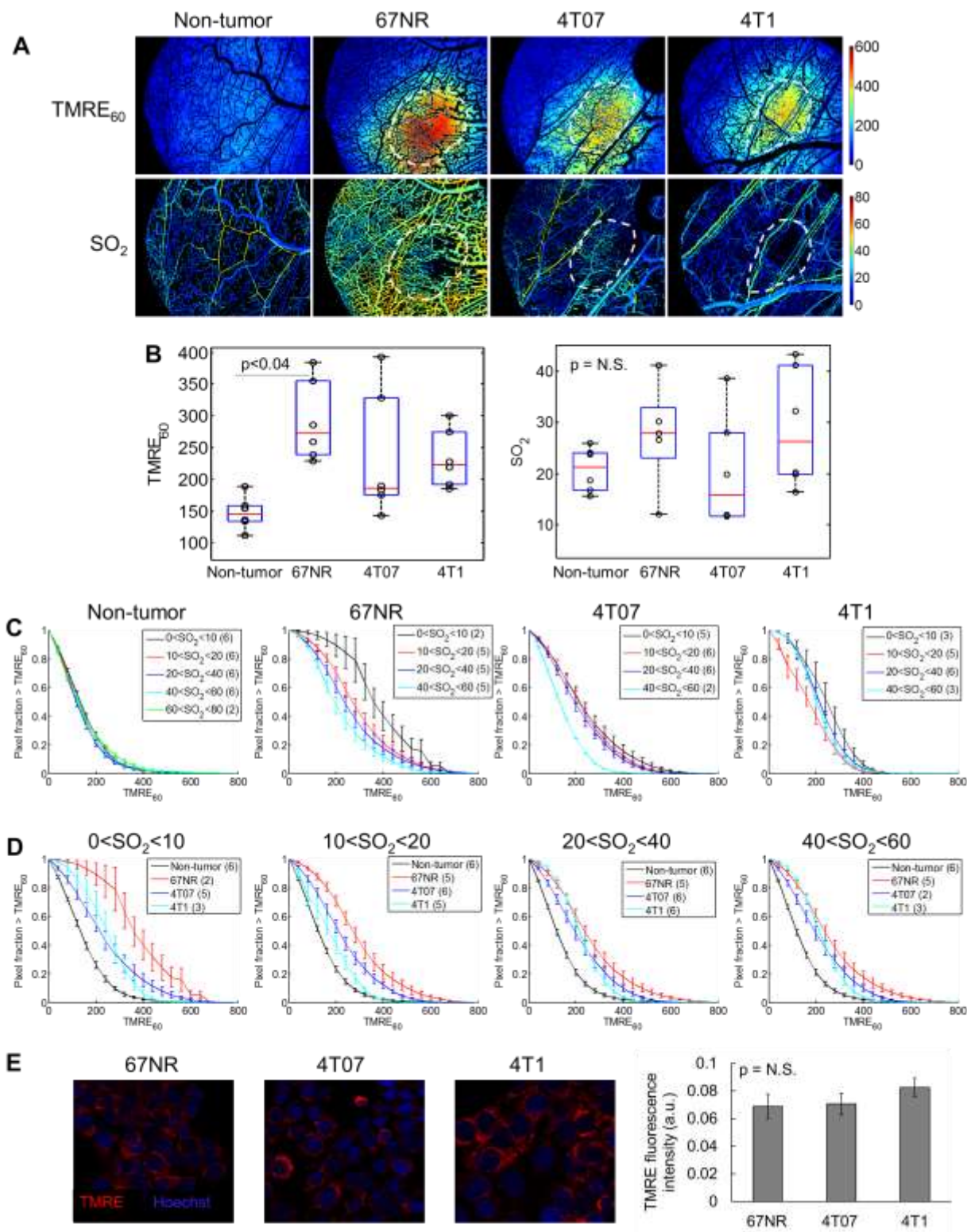
Figure 3.5 Increased TMRE uptake in tumors suggests aberrant mitochondrial metabolism. Panel 3.5A shows TMRE uptake and vascular oxygenation (SO_2) in a nontumor window chamber and nonmetastatic (67NR and 4T07) and metastatic (4T1) tumor window chambers after injection of 0.1mL of 25uM TMRE. Tumor regions are outlined in white. Figure

3.5B shows mean $TMRE_{60}$ and SO_2 in all tissue types. TMRE uptake is increased in tumors (67NR > Non-tumor, $p<0.04$), and mean SO_2 is comparable across all groups. Figure 3.5C shows the relationship between regional $TMRE_{60}$ and regional SO_2 in each tissue type. Each curve corresponds to a distribution of tissue pixels parsed by the SO_2 in the nearest vessel. In non-tumor tissue, TMRE uptake is stable regardless of SO_2. In non-metastatic 67NR and 4T07, trends indicate that TMRE uptake increases with decreasing SO_2. In metastatic 4T1, TMRE uptake is comparable across SO_2. Figure 3.5D shows that TMRE uptake in tumors is greater than in non-tumor tissue regardless of regional SO_2. The tumor line 67NR consistently has the greatest TMRE uptake at all SO_2. In vitro imaging of all tumor lines is shown in Figure 3.5E. Cells were incubated with TMRE for 30 minutes prior to imaging. Hoescht nuclear stain was added to cells 10 minutes prior to imaging. TMRE uptake was indistinguishable across groups. Error bars show standard error. Group numbers indicated in legend. n = 6 mice per group unless otherwise noted (Fig 3.5B,C,D). n = 6 plates per cell line (Fig 3.5E).

A preliminary study relating TMRE fluorescence intensity to predicted TMRE concentration is shown in Figure 3.6. A concentration curve was constructed from fluorescence measurements of known TMRE concentrations in solution (PBS), imaged with the same imaging system as our *in vivo* results. Fluorescence signal was background-subtracted using a plate of PBS containing no TMRE. Fluorescence was additionally corrected for day-to-day variations in lamp signal with an identical protocol used to correct all *in vivo* data (scaling factor = 1000/mean fluorescence of rhodamine standard). Increasing TMRE concentration linearly correlated with increasing corrected fluorescence signal (R^2 = 0.98, $p<0.001$). The equation governing the linear fit in Figure 3.6A was used to calculate the predicted tissue-level TMRE concentration from the average measured fluorescence of each group. Predicted tissue-level concentration ranges from 9.8nM (non-tumor) to 23.8nM (67NR).
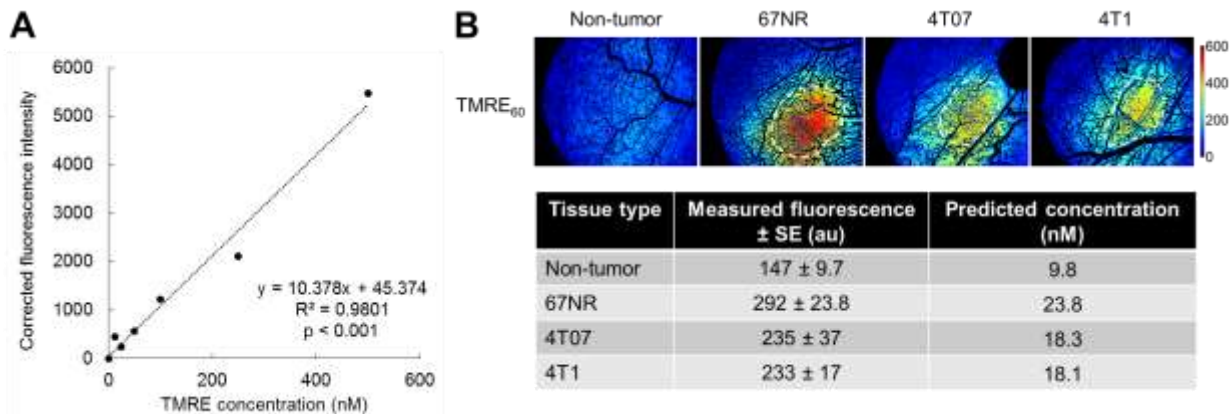

Tissue type	Measured fluorescence ± SE (au)	Predicted concentration (nM)
Non-tumor	147 ± 9.7	9.8
67NR	292 ± 23.8	23.8
4T07	235 ± 37	18.3
4T1	233 ± 17	18.1

Figure 3.6 TMRE uptake and predicted tissue-level concentration in all tissues. In **Fig 3.6A**, solutions containing increasing concentrations of TMRE (0-500nM) dissolved in PBS were imaged with the hyperspectral microscope system using the same imaging settings as the *in vivo* studies. Mean fluorescence intensity was averaged over the entire illuminated region of the phantoms. Background signal was calculated by imaging a plate containing only PBS, and the background fluorescence was subtracted from each TMRE phantom to give "corrected fluorescence intensity" (y-axis). Figure 3.6B shows the estimated mean concentration of TMRE at the tissue level in each tissue type. The curve in Fig 3.6A was used to calculate the predicted concentration (nM) from the measured TMRE fluorescence.

2: Development of a hypoxia "stress test" to relate metabolic stress response to metastatic potential

In Figure 3.7, 67NR, 4T07 and 4T1 window chamber tumors were stressed with hypoxia (10% inspired O_2). Based on our previous studies in non-tumor (shown in Fig 3.3, 3.4 and 3.7B), we expected a decrease in $TMRE_{60}$ during hypoxia relative to normoxia conditions ($p<0.02$). Interestingly, the non-metastatic tumor lines 67NR and 4T07 showed a significant decrease in TMRE uptake during hypoxia ($p<0.04$ for 67NR, $p<0.05$ for 4T07). On the contrary, TMRE uptake *increased* in metastatic 4T1 tumors ($p<0.04$). The ability to maintain mitochondrial membrane potential during stress such as hypoxia may indicate metabolic plasticity of 4T1 cells, and may be related to increased aggressiveness.
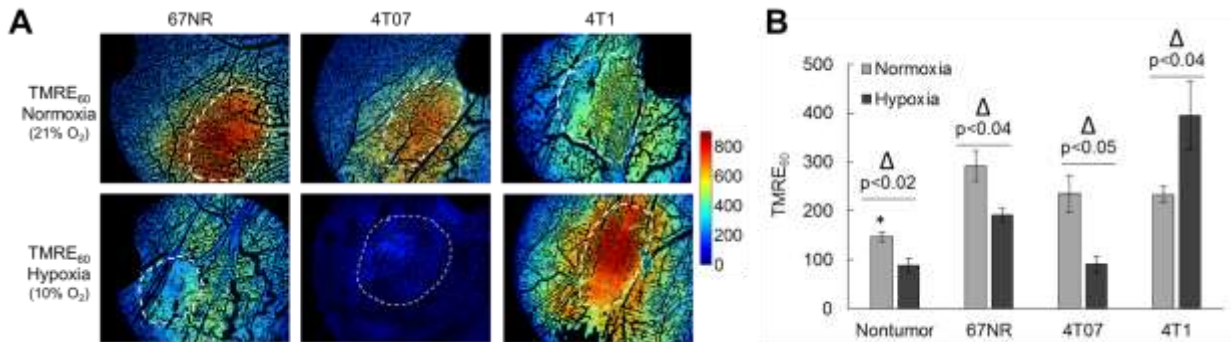

Figure 3.7 TMRE uptake changes in response to hypoxia. Panel 3.7A shows TMRE uptake in 67NR, 4T07, and 4T1 tumors subjected to normoxia (21% O_2) or hypoxia (10% O_2). In Figure 3.7B, mean $TMRE_{60}$ is shown for all tissue types under normoxia and hypoxia. At baseline, $TMRE_{60}$ in 67NR is significantly increased relative to non-tumor ($p<0.04$). After hypoxia, $TMRE_{60}$ decreases in non-tumor, 67NR, and 4T07 ($p<0.02$, $p<0.04$, and $p<0.05$, respectively). $TMRE_{60}$ increases in 4T1 after hypoxia ($p<0.04$).

We also investigated the change in glucose uptake in response to hypoxia. At baseline, metastatic 4T1 showed increased glucose uptake compared to all other tissue types ($p<0.05$). Non-tumor tissue showed an expected increase in glucose uptake during hypoxia ($p<0.04$), consistent with a shift away from oxidative metabolism and toward glycolysis when oxygen is limiting. The trends in 67NR and 4T07 tumors again mirrored the trend seen in non-tumor, with glucose uptake increasing slightly (though not significantly). In 4T1 however, glucose uptake decreased slightly, though not significantly.
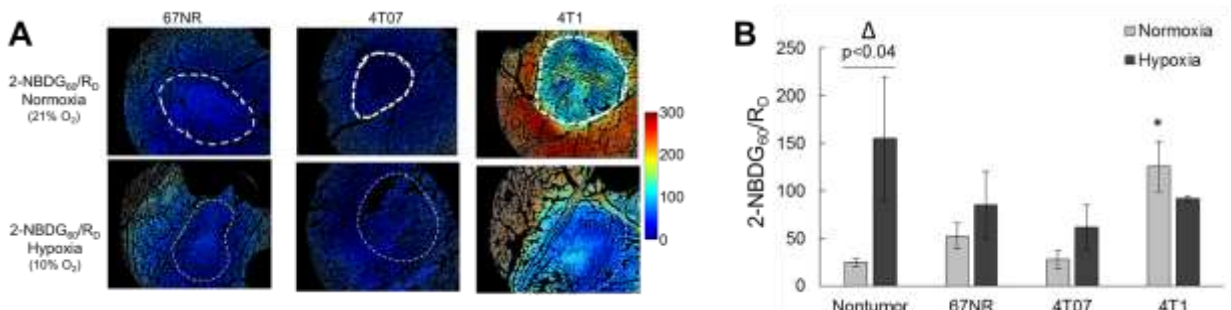
Figure 3.8 2-NBDG uptake changes in response to hypoxia. Panel 3.8A shows 2-NBDG uptake in 67NR, 4T07, and 4T1 tumors subjected to normoxia (21% O_2) or hypoxia (10% O_2). In Figure 3.8B, mean $2\text{-}NBDG_{60}/R_D$ is shown for all tissue types under normoxia and hypoxia. At baseline, $2\text{-}NBDG_{60}/R_D$ in 4T1 is significantly increased relative to all other groups ($p<0.05$). After hypoxia, $2\text{-}NBDG_{60}/R_D$ increases in non-tumor ($p<0.04$), 67NR, and 4T07 (not significant).

2-NBDG$_{60}$/R$_D$ decreases in 4T1 after hypoxia, though the change is not significant.

Lastly, we combined our glucose uptake and mitochondrial membrane potential endpoints into a single measure of metabolism called the "optical energy budget" (OEB, see Figure 3.9) that could be used to compare the tumor types. The OEB summary statistic is shown over each bar in Figure 3.9. OEB is calculated as OEB = 2-NBDG/(TMRE+2-NBDG), and an increased OEB corresponds to a tissue type that displays increased glucose uptake relative to mitochondrial membrane potential. Under normal conditions, 4T1 shows a highly glycolytic phenotype relative to 67NR and 4t07, consistent with our knowledge of the Warburg effect in this cell line. During hypoxia, the OEB reveals that 67NR and 4T07 shift metabolism toward glycolysis, whereas 4T1 seems to increase mitochondrial efficiency and decrease glucose uptake. The ability of some particularly aggressive cell types to maintain mmp during hypoxia has been reported, but to our knowledge has not been observed with metabolic imaging, or in the 4T1 tumor type. The link between tumor hypoxic response and metastasis is not yet well defined.
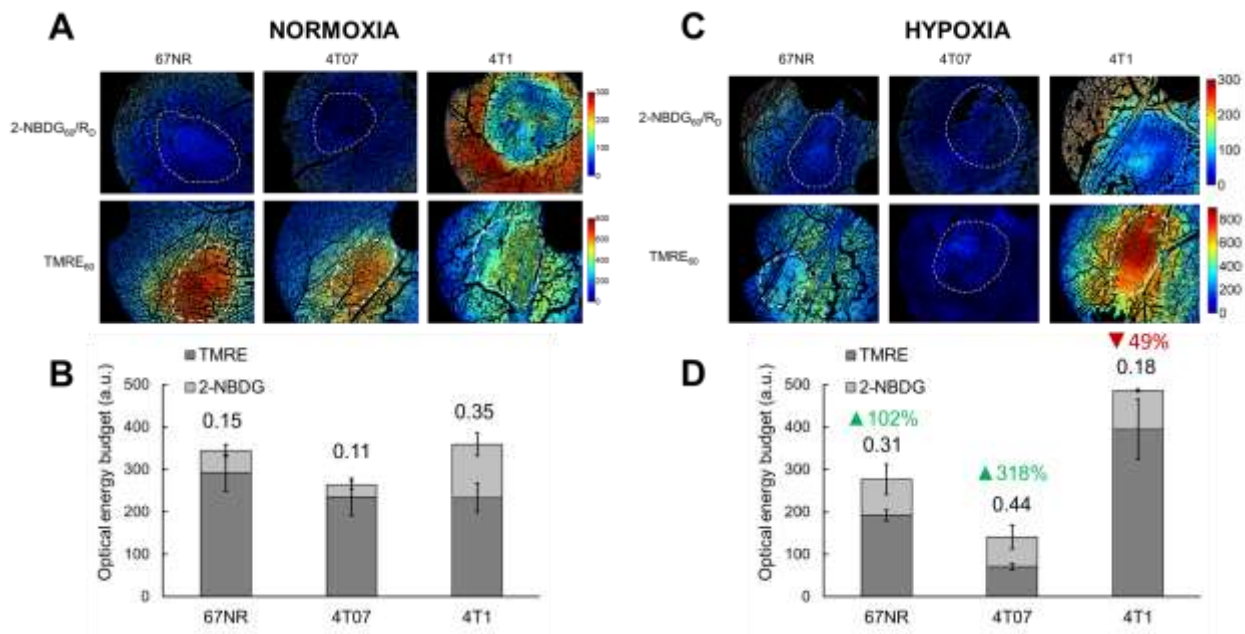

Figure 3.9 An optical energy budget reveals a unique hypoxic signature in metastatic tumors. 2-NBDG and TMRE uptake in tumors under baseline conditions are shown in Panel 3.9A. Optical energy budget (OEB = 2-NBDG/(TMRE+2-NBDG)) is shown for each tumor type in Figure 3.9B. OEB was increased in 4T1 relative to 67NR or 4T07 tumors. Uptake of TMRE and 2-NBDG under hypoxia (10%) is shown in Panel 3.9C. The OEB under hypoxia is shown for each tissue type. Relative to baseline conditions, 67NR and 4T07 increased OEB dramatically (102% and 318%, respectively). 4T1 tumors decreased OEB during hypoxia, showing a 49% decrease in OEB.

Our plans for year 5 originally focused on monitoring therapy response with glucose and oxygenation endpoints. However, emerging literature and new insights gained from our project shifted our focus toward incorporating a measurement of mitochondrial membrane potential into our toolbox. We are now well-poised to pursue a therapy monitoring project utilizing our integrated glucose, mmp, and SO$_2$ imaging technique. Targeted therapies such as PI3K-inhibition can lead to significant 'normalization' of the vasculature and direct cell signaling effects, both of which can have a profound impact on metabolic state. Our goal is to evaluate our optical energy budget in the context of therapy to determine which tumors are responsive at

an early timepoint based on the change or absence of change in OEB, allowing for personalization of therapy based on early response signatures. We also hope to use our hypoxic stress test as a pre-treatment screening tool, i.e. determine if we can correlate hypoxic changes in OEB to eventual therapy outcome.

3. KEY RESEARCH ACCOMPLISHMENTS:

AIM 1

- A robust spectral data acquisition software package was developed to facilitate data collection and integrity.
- Hi-resolution raster-scanned images were acquired for approximately 60 lumpectomy patients; the analysis based on breast density corroborates previous findings.

AIM 2

- Optimized the sparse component analysis (SCA) algorithm to distinguish positive from negative biopsies imaged with the high resolution microendoscope (HRME).
- Explored how higher resolution microscopes, such as a fluorescent confocal microscope, could be used to visualize ductal morphology in addition to nuclear morphology.
- Partnered with Rice University to acquire confocal images of resected breast tissue and developed computerized algorithms to segment and quantify nuclear and ductal parameters to further enhance our ability to characterize breast architectural features.

AIM 3

- Optimized an optical imaging agent for *in vivo* measurement of mitochondrial membrane potential in tumors
- Used optical imaging to reveal significant differences in the baseline metabolic phenotype of non-tumor tissue, non-metastatic tumors, and metastatic tumors
- Demonstrated a hypoxic stress test to identify aggressive tumor types *in vivo*

4. REPORTABLE OUTCOMES:

AIM 1:

1. Nichols, B.S., et al., A Quantitative Diffuse Reflectance Imaging (QDRI) System for Comprehensive Surveillance of the Morphological Landscape in Breast Tumor Margins. PloS one, 2015. **10**(6): p. e0127525.

AIM 2:

Journal publications – (published, in review and in progress)

1. Mueller J, Gallagher J, Chitalia R, Krieger M, Erkanli A, Willett R, Geradts J, Ramanujam N. Rapid staining and imaging of sub-nuclear features to differentiate between malignant and benign breast tissues at a point-of-care setting. BMC Cancer, 2015. Under review.

2. Dobbs J*, Mueller J*, Krishnamurthy S, Shin D, Kuerer H, Yang W, Ramanujam N, Richards-Kortum R. Micro-anatomical quantitative optical imaging: towards automated assessment of breast tissues. Breast Cancer Research, 2015, 17: 105.

3. Mueller J, Fu H, Mito J, Whitley M, Chitalia R, Erkanli A, Dodd L, Cardona D, Geradts J, Willett R, Kirsch D, Ramanujam N. A quantitative microscopic approach to predict local recurrence based on *in vivo* intraoperative imaging of sarcoma tumor margins. International Journal of Cancer, 2015, 137(10): 2403-12.

Conference abstracts and proceedings

1. Mueller J, Fu H, Javid M, Kirsch D, Willett R, Brown Q, Ramanujam N. Structured Illumination Fluorescence Imaging and Analysis for Identification of Residual Disease during Cancer Surgery. Biomedical Optics (BIOMED) Topical Meeting, 2014.

2. Mueller J, Fu H, Mito J, Javid M, Harmany Z, Dodd L, Willett R, Kirsch D, Brown Q, Ramanujam N. Quantitative high-resolution fluorescence imaging for in vivo detection of residual disease during cancer surgery. NCI-NIBIB Point of Care Technologies for Cancer Conference, 2014.

AIM 3:

Journal publications – (published, in review and in progress)
1. Martinez, A.F., S.S. McCachren III, M. Lee, H. Murphy, M.W. Dewhirst, N. Ramanujam. "In vivo optical imaging of the cationic rhodamine dye TMRE shows changes in mitochondrial membrane potential due to environmental perturbations and aberrant cancer metabolism". In progress.
2. Martinez, A.F., S. McCachren III, M. Lee, H. Murphy, M.W. Dewhirst, N. Ramanujam. "Optical energy budget reveals differences in the metabolic phenotype and hypoxic response of metastatic and non-metastatic cancers". In progress.
3. Rajaram, N., A. Reesor, C. Mulvey, A.E. Frees, and N. Ramanujam. "Non-invasive, simultaneous quantification of vascular oxygenation and glucose uptake in tissue." PLoS ONE 10(1): e0117132, doi:10.1371/journal.pone.0117132, 2015.
4. Frees, A.E., N. Rajaram, S.S. McCachren III, A.N. Fontanella, M.W. Dewhirst, and N. Ramanujam. "Delivery-corrected imaging of fluorescently-labeled glucose reveals distinct breast cancer phenotypes." PLoS ONE 9(12): e115529, doi:10.1371/journal.pone.0115529, 2014.

Conference abstracts and proceedings
1. Martinez, A.F., S.S. McCachren, M. Lee, N. Rajaram, M.W. Dewhirst, and N. Ramanujam. "Optical toolbox for in vivo analysis of glucose uptake, vascular oxygenation, and mitochondrial membrane potential in breast cancer." Technical poster session. Emerging Analytical Approaches, AACR: Metabolism and Cancer, Bellevue, Washington, June 2015.

4. **CONCLUSIONS:**

Aim 1

We have demonstrated that a multi-channel scanning technique is capable of providing rapid, sub-millimeter resolution surveillance of the tumor margin landscape, which accurately reports on the underlying histopathology. Although a 0.75mm sampling resolution still does not qualify as microscopy, it does provide a highly pragmatic technological intersection addressing the limitations of the native wide-field spectroscopy system and microscopy, and provides a 3-fold improvement in terms of the amount of tissue reviewed during histopathology. Sampling of a full margin currently requires 13.8 minutes, significantly longer than the 30 seconds required for a single, 6mm resolution spectral snapshot, however, this still is within the timing constraints warranted for an intra-operative tool: the amount of time elapsed between specimen removal and surgery completion is typically between 25-35 minutes. The margin-level, tissue morphology is accurately quantified using [β-carotene]/<μ_s'> as a surrogate for mammographic breast density, which can subsequently be used to stratify and accurately classify site level data. At the site-level, we observed that inadequate sampling resolution can lead to misclassification of tissue subtypes, specifically fibroadipose tissue, a mix of fibrous and adipose tissue, could not be statistically distinguished from pure adipose at the native 6mm probe resolution. A future analysis will quantify the influence of benign tissue near very small regions of disease, as site-level tissue types were not clearly clustered in several cases with purported malignant regions. In conclusion, these studies suggest that quantitative optical spectral imaging may be a pragmatic solution to the margin assessment problem and could ultimately be integrated into the clinical standard of care.

Aim 2

In conclusion, acriflavine staining and high resolution microendoscope (HRME) imaging combined with SCA+CT can be used to quantitatively diagnose breast disease. Additionally, quantitative APF and ductal parameters were measured in confocal fluorescence images of fresh breast tissue and used to develop a classification algorithm that distinguishes between 259 benign and malignant sites with an accuracy of 88%. The APF and ductal parameters described in this study could be used to develop criteria to automate breast lesion diagnosis for immediate evaluation of fresh tissue at the point of care obviating the need for extensive tissue preparation. Together, this work yields an optimized set of tools that are capable of imaging tissue at high resolution with no tissue processing and that can automatically segment and quantify those specimens. Ultimately, this platform provides a potentially useful adjunct to histopathological techniques by providing quality control at the point of care setting.

Aim 3

Recent literature challenges conventional wisdom that aerobic glycolysis is the sole metabolic program for aggressive and therapy-resistant cancers. Glucose and oxygenation endpoints are indeed critical indicators of tumor fate, but incorporating additional metabolic endpoints may give a more holistic view of cancer phenotype. In particular, mitochondrial metabolism has been indicated as a crucial metabolic program for quiescent cells that evade therapy.

We have incorporated the fluorescent molecule TMRE into our metabolic imaging toolbox to measure mitochondrial membrane potential, a surrogate for mitochondrial metabolism. By using this integrated toolbox to measure glucose uptake, vascular oxygenation, and mitochondrial membrane potential, we were able to separate non-tumor tissue, non-metastatic tumors, and

metastatic tumors based on metabolic phenotype. We developed a statistic called the "optical energy budget" (OEB) to quickly summarize metabolic phenotype, and saw that this statistic could monitor changes in metabolism during hypoxic stress. Further, the pattern of changes in OEB during hypoxia was distinct in metastatic tumors.

Looking ahead, we believe the optical toolbox and corresponding OEB endpoint will be valuable tools for measuring response to cancer therapies targeted at metabolism and vascular normalization. The method is ready for near-immediate adoption in preclinical studies for testing new cancer therapies and developing deeper understanding of tumor biology. To modify this method to be suitable for clinical studies, we propose to transition our optical toolbox to an optical spectroscopy platform. Optical spectroscopy is portable, fast, and non-destructive, making it an ideal technology for clinical studies, as well as for pre-clinical studies requiring repeated measurements over weeks or months.

Lastly, since our results indicate that using hypoxia to stress tumors can cause them to reveal their true metabolic phenotype, we propose that such a test could be used to aid in diagnosis and prognosis. In particular, this could be an exciting strategy when coupled with emerging patient-derived xenograft models. Further, incorporating a simple hypoxic stress test with currently used metabolic imaging modalities such as Positron Emission Tomography (PET) could be implemented without much change in standard pre-clinical or clinical workflow.

5. REFERENCES:

1. Jacobs, L., *Positive margins: the challenge continues for breast surgeons.* Ann Surgical Oncology, 2008. **15**(5): p. 1271-2.
2. Lee, M.C., et al., *Determinants of breast conservation rates: reasons for mastectomy at a comprehensive cancer center.* Breast J, 2009. **15**(1): p. 34-40.
3. Society, A.C. *Cancer Facts and Figures 2009*. 2009.
4. Sanchez, C., et al., *Factors associated with re-excision in patients with early-stage breast cancer treated with breast conservation therapy.* Am Surg, 2010. **76**(3): p. 331-4.
5. Mann, R.M., et al., *The impact of preoperative breast MRI on the re-excision rate in invasive lobular carcinoma of the breast.* Breast Cancer Res Treat, 2010. **119**(2): p. 415-22.
6. Balch, G.C., et al., *Accuracy of intraoperative gross examination of surgical margin status in women undergoing partial mastectomy for breast malignancy.* Am Surg, 2005. **71**(1): p. 22-7; discussion 27-8.
7. Mendez, J.E., et al., *Influence of breast cancer margin assessment method on the rates of positive margins and residual carcinoma.* Am J Surg, 2006. **192**(4): p. 538-40.
8. Huston, T.L., et al., *The influence of additional surgical margins on the total specimen volume excised and the reoperative rate after breast-conserving surgery.* Am J Surg, 2006. **192**(4): p. 509-12.
9. Kobbermann, A., et al., *Impact of Routine Cavity Shave Margins on Breast Cancer Re-excision Rates.* Ann Surg Oncol, 2010.
10. McCahill, L.E., et al., *Variability in reexcision following breast conservation surgery.* JAMA, 2012. **307**(5): p. 467-75.
11. Palmer, G.M. and N. Ramanujam, *A Monte Carlo-based inverse model for calculating tissue optical properties. Part I: Theory and validation on synthetic phantoms.* Appl. Opt., 2006. **45**(5): p. 1062-71.

12.   Palmer, G.M. and N. Ramanujam, *Monte-Carlo-based model for the extraction of intrinsic fluorescence from turbid media.* Journal of biomedical optics, 2008. **13**(2): p. 024017-024017-9.

13.   Zhu, C., et al., *Diagnosis of breast cancer using diffuse reflectance spectroscopy: Comparison of a Monte Carlo versus partial least squares analysis based feature extraction technique.* Lasers Surg Med, 2006. **38**(7): p. 714-24.

14.   Ramanujam, N. and G.M. Palmer, *Method for extraction of optical properties from diffuse reflectance spectra*. 2009, Google Patents.

15.   Brown, J.Q., et al., *Optical Spectral Surveillance of Breast Tissue Landscapes for Detection of Residual Disease in Breast Tumor Margins.* PloS one, 2013. **8**(7): p. e69906.

16.   Nichols, B.S., et al., *A Quantitative Diffuse Reflectance Imaging (QDRI) System for Comprehensive Surveillance of the Morphological Landscape in Breast Tumor Margins.* PloS one, 2015. **10**(6): p. e0127525.

17.   Brown, J.Q., *Optical Assesssment of Tumor Resection Margins in the Breast.* IEEE Journal of selected topics in Quantum Electronics, 2010. **16**(3): p. 530-544.

18.   Elkhuizen, P.H., et al., *Local recurrence after breast-conserving therapy for invasive breast cancer: high incidence in young patients and association with poor survival.* Int J Radiat Oncol Biol Phys, 1998. **40**(4): p. 859-67.

19.   Kumar, V., A. Abbas, and N. Fausto, *Robbins and Cotran Pathologic Basis of Disease*. 7th ed. 2005, Philadelphia: Elsevier Saunders.

20.   Cohen, C., *Image cytometric analysis in pathology.* Hum Pathol, 1996. **27**: p. 482-93.

21.   Millot, C. and J. Dufer, *Clinical applications of image cytometry to human tumour analysis.* Histol Histopathol, 2000. **15**: p. 1185-200.

22.   Jacobs, L., *Positive margins: the challenge continues for breast surgeons.* Ann Surg Oncol, 2008. **15**(5): p. 1271-2.

23.   Clarke, M., et al., *Effects of radiotherapy and of differences in the extent of surgery for early breast cancer on local recurrence and 15-year survival: an overview of the randomised trials.* Lancet, 2005. **366**(9503): p. 2087-106.

24.   Adeyi, O.A., *Pathology Services in Developing Countries-The West African Experience.* Archives of Pathology & Laboratory Medicine, 2011. **135**(2): p. 183-186.

25.   Rambau, P.F., *Pathology practice in a resource-poor setting: Mwanza, Tanzania.* Arch Pathol Lab Med, 2011. **135**(2): p. 191-3.

26.   Gareau, D.S., et al., *Rapid screening of cancer margins in tissue with multimodal confocal microscopy.* J Surg Res, 2012. **178**(2): p. 533-538.

27.   Drezek, R.A., et al., *Optical imaging of the cervix.* Cancer, 2003. **98**: p. 2015-27.

28.   Muldoon, T.J., et al., *Evaluation of quantitative image analysis criteria for the high-resolution microendoscopic detection of neoplasia in Barrett's esophagus.* J Biomed Opt, 2010. **15**: p. 026027.

29.   Balu, M., et al., *Distinguishing between benign and malignant melanocytic nevi by in vivo multiphoton microscopy.* Cancer Res, 2014. **74**(10): p. 2688-97.

30.   Schlichenmeyer, T.C., et al., *Video-rate structured illumination microscopy for high-throughput imaging of large tissue areas.* Biomed Opt Express, 2014. **5**(2): p. 366-77.

31.   Tanbakuchi, A.A., et al., *Clinical confocal microlaparoscope for real-time in vivo optical biopsies.* J Biomed Opt, 2009. **14**: p. 044030.

32.   Tanbakuchi, A.A., et al., *In vivo imaging of ovarian tissue using a novel confocal microlaparoscope.* Am J Obstet Gynecol, 2010. **202**(1): p. 90.e1-9.

33.   Dobbs, J.L., et al., *Feasibility of confocal fluorescence microscopy for real-time evaluation of neoplasia in fresh human breast tissue.* J Biomed Opt, 2013. **18**(10): p. 106016.

34. Clark, A.L., et al., *Confocal microscopy for real-time detection of oral cavity neoplasia.* Clin Cancer Res, 2003. **9**: p. 4714-21.

35. Karen, J.K., et al., *Detection of basal cell carcinomas in Mohs excisions with fluorescence confocal mosaicing microscopy.* Br J Dermatol, 2009. **160**: p. 1242-50.

36. Boppart, S.A., et al., *Optical coherence tomography: feasibility for basic research and image-guided surgery of breast cancer.* Breast Cancer Res Treat, 2004. **84**(2): p. 85-97.

37. Sun, J.G., et al., *Segmentation and correlation of optical coherence tomography and x-ray images for breast cancer diagnostics.* J Innov Opt Health Sci, 2013. **6**(2): p. 1350015.

38. Nguyen, F.T., et al., *Intraoperative evaluation of breast tumor margins with optical coherence tomography.* Cancer Res, 2009. **69**: p. 8790-6.

39. Hsiung, P.L., et al., *Benign and malignant lesions in the human breast depicted with ultrahigh resolution and three-dimensional optical coherence tomography.* Radiology, 2007. **244**(3): p. 865-74.

40. Zysk, A.M., et al., *Optical coherence tomography: a review of clinical development from bench to bedside.* J Biomed Opt, 2007. **12**(5): p. 051403.

41. Clark, A.L., et al., *Detection and diagnosis of oral neoplasia with an optical coherence microscope.* J Biomed Opt, 2004. **9**: p. 1271-80.

42. Nyirenda, N., D.L. Farkas, and V.K. Ramanujan, *Preclinical evaluation of nuclear morphometry and tissue topology for breast carcinoma detection and margin assessment.* Breast Cancer Res Treat, 2011. **126**(2): p. 345-54.

43. Mueller, J.L., et al., *Quantitative Segmentation of Fluorescence Microscopy Images of Heterogeneous Tissue: Application to the Detection of Residual Disease in Tumor Margins.* PLoS One, 2013. **8**(6): p. e66198.

44. Muldoon, T.J., et al., *Subcellular-resolution molecular imaging within living tissue by fiber microendoscopy.* Opt Express, 2007. **15**: p. 16413-23.

45. Ferguson, L.R. and W.A. Denny, *The genetic toxicology of acridines.* Mutat Res, 1991. **258**: p. 123-60.

46. Krolenko, S.A., et al., *Acridine orange accumulation in acid organelles of normal and vacuolated frog skeletal muscle fibres.* Cell Biol Int, 2006. **30**(11): p. 933-9.

47. Ballard, D., *Generalizing the Hough Transform to Detect Arbitrary Shapes*. 1981, Pattern Recognition. p. 111-122.

48. YOUDEN, W.J., *Index for rating diagnostic tests.* Cancer, 1950. **3**(1): p. 32-5.

49. Nandakumar, V., et al., *Isotropic 3D nuclear morphometry of normal, fibrocystic and malignant breast epithelial cells reveals new structural alterations.* PLoS One, 2012. **7**(1): p. e29230.

50. Chasles, F., B. Dubertret, and A.C. Boccara, *Optimization and characterization of a structured illumination microscope.* Opt Express, 2007. **15**(24): p. 16130-16140.

51. Hagen, N., L. Gao, and T.S. Tkaczyk, *Quantitative sectioning and noise analysis for structured illumination microscopy.* Opt Express, 2012. **20**(1): p. 403-13.

52. Gustafsson, M.G.L., *Surpassing the lateral resolution limit by a factor of two using structured illumination microscopy.* Journal of Microscopy-Oxford, 2000. **198**: p. 82-87.

53. Ladekarl, M. and F.B. Sørensen, *Quantitative histopathological variables in in situ and invasive ductal and lobular carcinomas of the breast.* APMIS, 1993. **101**(12): p. 895-903.

54. Ozaki, D. and Y. Kondo, *Comparative morphometric studies of benign and malignant intraductal proliferative lesions of the breast by computerized image analysis.* Hum Pathol, 1995. **26**(10): p. 1109-13.

55. Rajesh, L., P. Dey, and K. Joshi, *Automated image morphometry of lobular breast carcinoma.* Anal Quant Cytol Histol, 2002. **24**(2): p. 81-4.

56.   Latson, L., B. Sebek, and K.A. Powell, *Automated cell nuclear segmentation in color images of hematoxylin and eosin-stained breast biopsy.* Analytical and Quantitative Cytology and Histology, 2003. **25**(6): p. 321-331.

57.   Gupta, S., et al., *Role of morphometry in evaluation of cytologically borderline breast lesions: a study of 70 cases.* Diagn Cytopathol, 2012. **40**(3): p. 191-6.

58.   Mayr, N.A., et al., *Intraductal breast carcinoma: initial results of a morphometric study using computerized digital image analysis.* Clin Oncol (R Coll Radiol), 1990. **2**(2): p. 66-70.

59.   Anderson, N.H., et al., *Computerized scene segmentation for the discrimination of architectural features in ductal proliferative lesions of the breast.* J Pathol, 1997. **181**(4): p. 374-80.

60.   Gao, J., et al., *Quantitative morphometry by image analysis of normal, hyperplastic and cancerous ductal breasts.* Anal Quant Cytol Histol, 2009. **31**(5): p. 255-61.

61.   Dobbs, J.L., et al., *Feasibility of confocal fluorescence microscopy for real-time evaluation of neoplasia in fresh human breast tissue.* Journal of Biomedical Optics, 2013. **18**(10).

62.   Dobbs, J., et al., *Confocal fluorescence microscopy for rapid evaluation of invasive tumor cellularity of inflammatory breast carcinoma core needle biopsies.* Breast Cancer Res Treat, 2014.

63.   Schiffhauer, L.M., et al., *Confocal Microscopy of Unfixed Breast Needle Core Biopsies: A Comparison to Fixed and Stained Sections.* BMC Cancer, 2009. **9**.

64.   Parrish, A., et al., *Reflectance confocal microscopy for characterization of mammary ductal structures and development of neoplasia in genetically engineered mouse models of breast cancer.* Journal of Biomedical Optics, 2005. **10**(5).

65.   Tilli, M.T., et al., *Real-time imaging and characterization of human breast tissue by reflectance confocal microscopy.* Journal of Biomedical optics, 2007. **12**(5): p. 051901.

66.   Abeytunge, S., et al., *Confocal microscopy with strip mosaicing for rapid imaging over large areas of excised tissue.* Journal of Biomedical Optics, 2013. **18**(6).

67.   Pierce, M.C., D.J. Javier, and R. Richards-Kortum, *Optical contrast agents and imaging systems for detection and diagnosis of cancer.* International Journal of Cancer, 2008. **123**(9): p. 1979-1990.

68.   van de Ven, A.L., K. Adler-Storthz, and R. Richards-Kortum, *Delivery of optical contrast agents using Triton-X100, part 2: enhanced mucosal permeation for the detection of cancer biomarkers.* Journal of Biomedical Optics, 2009. **14**(2).

69.   Pierce, M., D. Yu, and R. Richards-Kortum, *High-resolution fiber-optic microendoscopy for in situ cellular imaging.* J Vis Exp, 2011(47).

70.   Rosbach, K.J., et al., *High-resolution fiber optic microscopy with fluorescent contrast enhancement for the identification of axillary lymph node metastases in breast cancer: a pilot study.* Biomedical Optics Express, 2010. **1**(3): p. 911-922.

71.   Thekkek, N. and R. Richards-Kortum, *Optical imaging for cervical cancer detection: solutions for a continuing global problem.* Nat Rev Cancer, 2008. **8**(9): p. 725-31.

72.   Muldoon, T.J., et al., *Evaluation of quantitative image analysis criteria for the high-resolution microendoscopic detection of neoplasia in Barrett's esophagus.* J Biomed Opt, 2010. **15**(2): p. 026027.

73.   Thekkek, N., S. Anandasabapathy, and R. Richards-Kortum, *Optical molecular imaging for detection of Barrett's-associated neoplasia.* World J Gastroenterol, 2011. **17**(1): p. 53-62.

74.   Kyrish, M., et al., *Needle-based fluorescence endomicroscopy via structured illumination with a plastic, achromatic objective.* J Biomed Opt, 2013. **18**(9): p. 096003.

75.   Rosen, P.P., *Rosen's Breast Pathology.* 3 ed. 2008, Philadelphia, PA, USA: Lippincott Williams & Wilkins. 1116.

76.   Matas, J., et al., *Robust wide-baseline stereo from maximally stable extremal regions*. 2004, Image and Vision Computing. p. 761-767.

77.   Kaakinen, M., et al., *Automatic detection and analysis of cell motility in phase-contrast time-lapse images using a combination of maximally stable extremal regions and Kalman filter approaches.* J Microsc, 2014. **253**(1): p. 65-78.

78.   Arteta, C., et al., *Learning to detect cells using non-overlapping extremal regions.* Med Image Comput Comput Assist Interv, 2012. **15**(Pt 1): p. 348-56.

79.   Schondorf, H. and H. Naujoks, *DETERMINING THE NUCLEAR-AREA IN NORMAL BREAST EPITHELIA AND IN THE NUCLEI OF MAMMARY CARCINOMAS.* Journal of Cancer Research and Clinical Oncology, 1985. **109**(3): p. 241-244.

80.   Schöndorf, H. and H. Naujoks, *Determining the nuclear area in normal breast epithelia and in the nuclei of mammary carcinomas.* J Cancer Res Clin Oncol, 1985. **109**(3): p. 241-4.

81.   BLOOM, H.J. and W.W. RICHARDSON, *Histological grading and prognosis in breast cancer; a study of 1409 cases of which 359 have been followed for 15 years.* Br J Cancer, 1957. **11**(3): p. 359-77.

82.   Foote, F.W. and F.W. Stewart, *Lobular carcinoma in situ: A rare form of mammary cancer.* Am J Pathol, 1941. **17**(4): p. 491-496.3.

83.   Simoes, R.V., et al., *Metabolic Plasticity of Metastatic Breast Cancer Cells: Adaptation to Changes in the Microenvironment.* Neoplasia, 2015. **17**(8): p. 671-84.

84.   Vowinckel, J., et al., *MitoLoc: A method for the simultaneous quantification of mitochondrial network morphology and membrane potential in single cells.* Mitochondrion, 2015. **24**: p. 77-86.

85.   Onoe, S., et al., *Investigation of cyanine dyes for in vivo optical imaging of altered mitochondrial membrane potential in tumors.* Cancer Med, 2014. **3**(4): p. 775-86.

86.   Gottlieb, E., et al., *Mitochondrial membrane potential regulates matrix configuration and cytochrome c release during apoptosis.* Cell Death Differ, 2003. **10**(6): p. 709-17.

87.   Perry, S.W., et al., *Mitochondrial membrane potential probes and the proton gradient: a practical usage guide.* Biotechniques, 2011. **50**(2): p. 98-115.

88.   Xie, H., et al., *Mitochondrial alterations near amyloid plaques in an Alzheimer's disease mouse model.* J Neurosci, 2013. **33**(43): p. 17042-51.

89.   Frees, A.E., et al., *Delivery-corrected imaging of fluorescently-labeled glucose reveals distinct metabolic phenotypes in murine breast cancer.* PLoS One, 2014. **9**(12): p. e115529.

90.   Rajaram, N., et al., *Delivery rate affects uptake of a fluorescent glucose analog in murine metastatic breast cancer.* PLoS One, 2013. **8**(10): p. e76524.

91.   Sorg, B.S., et al., *Hyperspectral imaging of hemoglobin saturation in tumor microvasculature and tumor hypoxia development.* J Biomed Opt, 2005. **10**(4): p. 44004.